Single-cell RNA sequencing unveils the hidden powers of zebrafish kidney for generating both hematopoiesis and adaptive antiviral immunity

Chongbin Hu[1], Nan Zhang[1], Yun Hong[1], Ruxiu Tie[4], Dongdong Fan[1], Aifu Lin[1], Ye Chen[1,3*], Lixin Xiang[1*], Jianzhong Shao[1,2*]

[1]College of Life Sciences, Key Laboratory for Cell and Gene Engineering of Zhejiang Province, Zhejiang University, Hangzhou, People's Republic of China. [2]Laboratory for Marine Biology and Biotechnology, Qingdao National Laboratory for Marine Science and Technology, Qingdao, People's Republic of China. [3]Division of Medical Genetics and Genomics, the Children's Hospital, Zhejiang University School of Medicine, Hangzhou, China. [4]Bone Marrow Transplantation Center, the First Affiliated Hospital, Zhejiang University School of Medicine, Hangzhou, China.

[*]For correspondence: shaojz@zju.edu.cn (J.-z.S.), xianglx@zju.edu.cn (L.-x.X.) and yechency@zju.edu.cn (Y. C)

Abstract

The vertebrate kidneys play two evolutionary conserved roles in waste excretion and osmoregulation. Besides, the kidney of fish is considered as a functional ortholog of mammalian bone marrow that serves as a hematopoietic hub for generating blood cell lineages and immunological responses. However, knowledge about the properties of kidney hematopoietic cells, and the functionality of kidney in fish immune systems remain to be elucidated. To this end, our present study generated a comprehensive atlas with 59 hematopoietic stem/progenitor cell (HSPC) and immune-cell types from zebrafish kidney via single-cell transcriptome profiling analysis. These populations included almost all known cells associated with innate and adaptive immunity, and displayed differential responses to viral infection, indicating their diverse functional roles in antiviral immunity. Remarkably, HSPCs were found to have extensive reactivities to viral infection, and the trained immunity can be effectively induced in certain HSPCs. In addition, the antigen-stimulated adaptive immunity can be fully generated in kidney, suggesting kidney acting as a secondary lymphoid organ. These results indicated that fish kidney is a dual-functional entity with functionalities of both primary and secondary lymphoid organs. Our findings illustrated the unique features of fish immune system, and highlighted the multifaced biology of kidney in ancient vertebrates.

Keywords

single-cell transcriptome profiling, zebrafish kidney, HSPCs, immune cell types,

hematopoiesis and antiviral immunity

Abbreviations: SVCV, spring viremia of carp virus; scRNA-seq, single-cell RNA sequencing; HSPCs, hematopoietic stem and progenitor cells; AID, activation-induced cytidine deaminase; Igs, immunoglobulins; APCs, antigen-presenting cells; IFNs, interferons; MAST, Model-based Analysis of Single-cell Transcriptomics; DEs, dual expressers; SHM, somatic hypermutation; DCs, dendritic cells; EPC, Epithelioma papulosum cyprinid; CPE, cytopathic effect; $TCID_{50}$, 50% tissue culture infective dose; PCA, principal component analysis; t-SNE, t-Distributed Stochastic Neighbor Embedding; GO, Gene Ontology; KEGG, Kyoto Encyclopedia of Genes and Genomes; cDC, classical DC; pDC, plasmacytoid DCs; DEGs, differentially expressed genes; BCG, Bacillus Calmette-Guerin; HSCs, hematopoietic stem cells; MPPs, multipotent progenitors; CMLPs, common myeloid-lymphoid progenitors; CMMEPs, common myeloid-megakaryocyte-erythroid progenitors; MACS, magnetic-activated cell sorting; RT-qPCR, quantitative real-time PCR.

Introduction

Teleost fish are a group of indispensable model organisms for comprehending the evolutionary history and general principles underlying the design of the vertebrate immune system, since they stand as the earliest living jawed vertebrates known as an important link in vertebrate evolution[1]. Over the recent decades, the field of fish immunology has made significant strides, notably hastening the identification and characterization of functional genes and signaling pathways intricately associated with both piscine innate and adaptive immunities. These advances stem from the progress in genome projects encompassing diverse fish species, and have markedly enriched our comprehension of the molecular underpinnings of fish immunity[2-4]. Some breakthroughs have not only challenged established paradigms about the immune system but have also unveiled novel dimensions of mammalian immunity[1,2]. Thus far, it was generally accepted that teleost fish possess the fundamental components of both innate and adaptive immune systems, akin to those seen in humans and other mammalian counterparts[5,6]. However, our grasp of the precise architectural layout, cellular coordination, and functional attributes of the fish immune system, particularly the adaptive facet, remains incomplete[6,7]. Evolutionarily speaking, bony fish represent the earliest living organisms endowed with a rudimentary adaptive immune system encompassing basic molecular and cellular constituents. These encompass immunoglobulins (Igs), antigen-specific receptors (TCR/BCR) driven by the recombination-activating genes, major histocompatibility complex class I and II (MHC-I/II) molecules, as well as T and B lymphocytes. These cellular elements

77 populate the primary and secondary lymphoid organs of fish, such as the thymus and
78 spleen[8-10]. Notwithstanding, the fish adaptive immune system is characterized by its
79 own set of specializations and distinctive attributes. Notably absent in fishes are the
80 bone marrow, histologically discernible lymph nodes, Peyer's patches, and germinal
81 centers—entities that define primary and secondary lymphoid organs in mammals[11,12].
82 Additionally, fishes lack antibody class-switch recombination activity, albeit retaining
83 the ability to express activation-induced cytidine deaminase (AID)[13,14]. These
84 revelations underscore the substantial diversity inherent in immune systems across
85 distinct vertebrate taxonomic groups. Consequently, teleost fish emerge as invaluable
86 primitive animal models, illuminating previously uncharted events during the
87 emergence and phylogenetic progression of adaptive immune systems. Such
88 endeavors stand to elucidate the distinct principles governing the immunology of
89 ancient vertebrates, thereby furnishing scientific substantiation for a broader
90 comprehension of the evolutionary trajectory of vertebrate immune systems.
91 In light of these considerations, we have recently generated a comprehensive
92 atlas of immune cell types within the spleen of zebrafish, employing a single-cell
93 transcriptome profiling approach[15]. Our work has entailed the classification of splenic
94 leukocytes into 11 principal categories and the identification of over 50 subset
95 populations within these categories. Moreover, we have delineated the differential
96 responses of various subset cells—both innate and adaptive—to infection by the
97 spring viremia of carp virus (SVCV). Particularly noteworthy was our discovery of
98 hematopoietic stem and progenitor cells (HSPCs) existed within the spleen. This
99 observation intimates that the fish spleen may well function as a hematopoietic site,
100 transcending its established role as a secondary lymphoid organ. These insights offer
101 fresh perspectives into the intricacies and distinctive attributes of the fish immune
102 system, setting it apart from its mammalian counterparts. Seeking to attain a deeper
103 understanding of the fish immune system, our present study has undertaken a further
104 exploration of immune cell types and their functional characteristics within the kidney
105 of zebrafish. This investigation places special emphasis on the hematopoietic activity
106 of kidney HSPCs and the adaptive immune responses of kidney immune cells towards
107 viral infections. As a result, our classification efforts have yielded 13 categories of
108 cells from kidney leukocyte preparations, unearthing 59 potential subset cells
109 spanning HSPCs and immune cell-associated categories. The observed subset
110 populations manifest disparate reactions to SVCV infection. Most notably, some
111 HSPC subsets exhibit a robust proliferative response to viral infection, capable of
112 inducing trained immunity. Furthermore, we have successfully identified a
113 comprehensive array of cells—encompassing diverse antigen-presenting cells (APCs)
114 as well as effector T and B cells—integral for the full activation of adaptive immunity
115 within the kidney. These adaptive immune-associated cells display marked

116 responsiveness to SVCV infection and antigenic stimulation. Evidently, the complete
117 process of adaptive immunity unfolds within the kidney, as evidenced by the
118 substantial expansion, activation, and somatic hypermutation (SHM) of
119 antigen-specific T and B cells upon exposure to cognate antigens. These results
120 strongly affirmed the kidney's dual role as a lymphoid organ, boasting both
121 hematopoietic functionality and adaptive immune reactivity in adult fish.
122 Consequently, our findings cast the fish kidney in the role of a secondary lymphoid
123 organ, supplementing its recognized status as a primary lymphoid organ. This
124 advancement significantly improved our current comprehension of fish hematopoietic
125 and immune systems, thus advancing our insights into the multifaceted biology of the
126 kidney in ancient vertebrates.
127
128 **Results**
129 **Categories of immune-associated cells in kidney**
130 In order to profile distinct immune-cell categories within the kidneys, leukocytes
131 were extracted from zebrafish kidney tissues. The experimental groups consisted of
132 fish treated with PBS (control), fish infected with SVCV (infected), and fish that
133 underwent both vaccination with inactivated SVCV and subsequent SVCV infection
134 (vaccinated+infected). Each sample comprised leukocytes from 60 fish and was
135 subjected to scRNA-seq using the 10× Chromium platform. Following sequencing,
136 the control group exhibited mean reads/median genes per cell of 34,501/1,090, the
137 infected group showed 29,706/1,383, while the vaccinated+infected group displayed
138 37,611/1,379. The total number of detected genes in leukocyte samples from the
139 control, infected, and vaccinated+infected groups were 26,345, 26,865, and 25,342,
140 respectively. Employing an unsupervised cluster detection algorithm (SEURAT), we
141 identified 13 distinct clusters of cells exhibiting similar gene expression profiles
142 (**Figure 1A**). Moreover, specific genes were pinpointed within each cluster. Notably,
143 clear demarcation boundaries were evident for each cluster in the heatmap, while dot
144 plot and violin plot analyses indicated that a PCA-based cell separation approach was
145 indeed favorable for our investigation (**Figure 1B and C, Figure 1—figure**
146 **supplement 2**).
147 The 13 clusters were classified as neutrophils, macrophage/myeloid cells, B cells,
148 T/NK cells, and three categories of HSPCs (HSPCs 1–3), along with renal cells
149 (kidney multiciliated cells, kidney mucin cells, kidney distal tubule and proximal
150 tubule cells) (**Figure 1A–C**). Clusters 0, 2, and 9 were identified as neutrophils based
151 on their expression of lineage marker genes including *mpx*, *lyz*, *cpa5*, *cd11b*, *adgrg3*
152 and *nccrp1*. Notably, cluster 0 exhibited high expression of *scpp8*, *mmp13a.1*, *mmp9*,
153 *tlr5b*, and *gpr84*, while cluster 2 was actively expressing interferon-inducible genes
154 like *zgc:152791* (*ifi27.2*, interferon alpha inducible protein 27.2) and *si:dkey-188i13.6*

155 (*ifi27.3*, interferon alpha inducible protein 27.3). Cluster 9, on the other hand,
156 displayed elevated expression of *hmgn2*, *hmgb2a*, and *top2a*. The functional
157 implications of these genes in neutrophils necessitate further exploration (**Figure 1C**
158 **and D** and **Supplementary file 1**). Cluster 1 was identified as a macrophage/myeloid
159 population due to the expression of lineage-specific genes including *mpeg1.1*, *ctss2.2*,
160 *mpeg1.2*, *grn1*, *marco* and *grna*. Additionally, cluster 1 exhibited expression of
161 *s100a10b*, *lgals3bpb*, and *c1qb*, implicated in classical complement pathway
162 activation (**Figure 1C and E** and **Supplementary file 1**). Cluster 3 represented B
163 cells, expressing lineage marker genes like *ighm*, *ighd*, *ighz*, *igl3v5*, *cd79a*, *cd79b* and
164 *cd37* (**Figure 1C and F**). Consistent with the existence of Mpeg1.1^{+} B cells in
165 zebrafish kidney, gut, skin and spleen tissues[16], this cluster displayed expression of
166 *mpeg1.1*. Notably, cluster 3 also highly expressed *igic1s1*, *zgc:194275*, *igl1c3* and
167 *cxcr4a*, the latter harbors major chemotactic activity to lymphocytes (**Supplementary**
168 **file 1**). Clusters 4 and 6 corresponded to HSPCs 1 and HSPCs 2 populations, marked
169 by the expression of pertinent signature genes like *nanos1*, *spi2*, *meis1b*, *foxp4*, *csf1rb*,
170 *gtpbp4*, *rpl5b*, *rplp2l*, *rpl18*, *rps7*, *rsl1d1* in cluster 4, and *mki67*, *mcm5*, *dut*, *npm1a*,
171 *snu13b*, *cnbpa* in cluster *6* (**Figure 1C, I and J** and **Supplementary file 1**)[17]. Cluster
172 5 represented T and NK cells, expressing T-cell signature genes including *trac*, *trbc*,
173 *cd3ζ*, *lck*, *zap70*, *cd4-1*, *cd8a*, *runx3*, *il2rb*, *bcl11ba* and *il7r*, as well as NK lineage
174 genes like *nkl.2*, *cd56*, *cd94*, *cd27*, *zbtb32* and *il2rb*. Additionally, cluster 5 also
175 highly expressed *ccl34b.4*, *ccl33.3*, *ccl36.1*, *nk-lysin*, *sla2*, *tnfrsf18*, and *tnfrsf9*, the
176 latter contributes to the clonal expansion, survival, and development of T cells
177 (**Figure 1C and G** and **Supplementary file 1**)[18,19]. Cluster 8 denoted the HSPCs 3
178 population, expressing *zfpm1*, *meis1b*, *gata1a*, *zeb2a*, *tal1*, *mef2aa*, *mpl*, *pbx1a* and
179 *hdr* marker genes (**Figure 1C, K**). This HSPC population also actively expressed
180 *hsp70* (*hsp70.1*, *hsp70l*, *hsp70.3*), *itga2b*, *thbs1b*, *hbaa1*, *hbaa2*, *hbba1*, *hbba1.1*, and
181 *rgcc*, among which *hsp70* members, *hbaa1*/2 and *hbba1*/*1.1* are essential for the
182 differentiation of hematopoietic progenitors into erythroids (**Supplementary file 1**)[20].
183 Clusters 7, 10, 11, and 12, characterized by lineage-specific genes like *tuba7l*, *dnai1.1*,
184 *kif17*; *clcnk*, *hoxb8a*, *cldnh*; *muc2.2*, *agr2*, *itln1*; and *slc26a1*, *slc5a12*, *slc13a3*
185 respectively, represented kidney multiciliated cells, kidney distal tubule cells, kidney
186 mucin cells, and kidney proximal tubule cells (**Figure 1C and L–O**)[21]. These renal
187 cells are remnants in the preparation of leukocytes. It's noteworthy that cluster 11
188 exhibited high expression of genes like *zmp:0000001323*, *CABZ01058647.1*,
189 *si:dkey-203a12.2* (*spink2.7*), *spink2.5*, *spink2.10*, and *spink2.4*, resembling a unique
190 serpin-secreting cell population recently identified in zebrafish spleen tissues[15].
191
192 **Characterization of kidney HSPCs**
193 To achieve a more comprehensive understanding of kidney hematopoietic cell

194 populations, subclustering was conducted exclusively on the three HSPC clusters
195 depicted in Figure 1. This analysis unveiled 11 enrichments (designated as H0–H10)
196 (**Figure 2A**). To validate our outcomes, we aligned the subset-specific genes of each
197 cluster and the ensuing heatmap indicated a distinct categorization for each cluster
198 (**Figure 2B**). Within this context, H0 manifested as a Nanos1^{+}Spi2^{+} phenotypic
199 cluster expressing signature genes *nanos1* and *spi2*, alongside specific expressions of
200 *sla2*, *csf1rb*, *rn7sk*, *sik1* and *irf1b*, forming a collection of potential new marker genes
201 (**Figure 2A-C**). Meanwhile, H1 was identified as a group of cycling HSPCs,
202 characterized by the expression of the marker gene *mki67*. This cluster also exhibited
203 pronounced expression of *hist1h4l.12*, *tubb2b*, *hmgb2a*, *hmgb2b*, *zgc:110425*, *grn1*,
204 *BX640512.2* and *si:ch73-281n10.2* genes (**Figure 2A-C** and **Supplementary file 2**).
205 It's noteworthy that the presence of H0 and H1 populations has been corroborated in
206 previous research[17]. H2, H3, and H4 clusters demonstrated high expression of
207 potential signature genes: *blf*, *hdr*, *rhag*, *mef2aa*, *rgcc*, *pmp22b*, *fth1a*, *prdx2*, *mych*,
208 *igfbp1a* in H2; *CR318588.2*, *zgc:152791*, *si:busm1-266f07.2*, *CR318588.3*,
209 *CR936442.1*, *tnfrsf9a*, *tat* in H3; and *BX640512.2*, *grn1*, *BX323596.2*, *cxcl11.1*,
210 *marcksl1b*, *lgals2a*, *txn*, *psma3*, *atp5mc1* in H4 (**Figure 2A-C** and **Supplementary**
211 **file 2**), respectively. The functional characteristics and developmental potential of
212 these three clusters require further elucidation. H5 was categorized as a group of NK
213 progenitors, exhibiting high expression of *gata3*, *nkl.3*, *nkl.4*, *ccl34b.4*, *CR388164.2*,
214 *ccl33.3*, *dusp2*, *BX005105.1, icn*, *bhlhe40*, and *coro1a* (**Figure 2A-C** and
215 **Supplementary file 2**). Cells within H6 represented myeloid progenitors, showing
216 extensive expression of *mmp13a.1*, *si:ch1073-429i10.1*, *il1b*, *cpa5*, *mpx*, *timp2b*,
217 *BX908782.2*, *npsn*, *lect2l* and *lyz* marker genes (**Figure 2A-C**). H7 and H8 were
218 identified as erythrocyte and lymphoid progenitor populations, denoted by their
219 expression of *hbba1.1*, *hbaa1*, *hbba1*, *si:ch211-5k11.8*, *hbba2*, *hbaa2*,
220 *si:ch211-103n10.5*, *cahz*, *hemgn* in H7, and *pbx1a*, *pdpk1a*, *rag1*, *rag2*, *cxcr4b*, *h2afx*,
221 *ccr9a*, *sid1*, *zgc:77784*, *nme3*, *kdm6bb* in H8, respectively (**Figure 2A-C**). H9 and
222 H10 clusters were discerned as endothelial and thrombocyte progenitors due to their
223 expression of marker genes such as *cdh5*, *kdrl*, *pecam1*, *igfbp5b*, *rbp4*, *cxcl18b*,
224 *cxcl12a*, *selenop*, *jun*, *fosl1a*, *jdp2b*, *fosab*, *si:ch73-335l21.4* in H9, and *itga2b*, *fn1b*,
225 *thbs1*, *sele*, *aldob*, *apln*, *tpm4a*, *hbegfb*, *cald1a*, *fgl2a*, *pim2*, *atp2b1a* in H10 (**Figure**
226 **2A-C**). The endothelial progenitors were also found in the bone marrow of mouse,
227 and they are developmentally associated with a subset of CD34^{+} hematopoietic stem
228 cells, and can differentiate ex vivo to an endothelial phenotype[22,23]. Subsequently,
229 pseudotime trajectory analysis revealed that a significant portion of HSPCs were
230 positioned within a primary trajectory characterized by five bifurcations and five
231 stages (**Figure 3A-C**). The endothelial (H9) and thrombocyte (H10) progenitors were
232 situated towards the trajectory's origin. This arrangement partially validated the

233 constructed trajectory (**Figure 3C**). H4 cells were positioned towards the trajectory's
234 terminus (**Figure 3C**). H2 cells, along with erythrocyte (H7) and lymphoid (H8)
235 progenitors, were positioned towards the trajectory's midpoint. H0 and H3
236 populations, along with NK (H5) and myeloid (H6) progenitors, were located towards
237 both the origin and midpoint of the trajectory. Furthermore, an analysis of the
238 pseudotime dynamics of significantly changed genes in the 11 HSPC clusters revealed
239 three modules delineated by their pseudotemporal expression patterns (**Figure 3D**
240 **and E**). In addition, RNA velocity analysis showed the differentiation potential of H0,
241 H1, H2, H3 and H4 subclusters into myeloid, thrombocyte/erythrocyte and lymphoid
242 progenitors (**Figure 3F**). These findings collectively suggested that H0-H4 clusters
243 potentially represent a group of stem and early progenitors that lead to late
244 progenitors responsible for differentiation into erythroid, myeloid, and lymphocyte
245 lineages. Notably, we recently detected the presence of HSPCs in zebrafish spleen
246 tissues, indicating the spleen's role as a hematopoietic organ in fish[15]. To compare
247 HSPC characteristics between the kidney and spleen, we integrated scRNA-seq data
248 from both organs and subjected the merged dataset to cell classification. This
249 assessment demonstrated that the newly generated atlas shared overall consistency
250 with the kidney and spleen, merging proportional HSPCs and immune cells from the
251 two organs to varying extents (**Figure 4A**). These observations underscored the
252 presence of substantial overlapping HSPCs and immune cell types in both the kidney
253 and spleen. Furthermore, pseudotime trajectory analysis highlighted similar cell
254 differentiation trajectories shared between the kidney and spleen (**Figure 4B-E**).
255 Pseudotime dynamics of significantly altered genes across all categories were
256 analyzed and organized into three modules based on their pseudotemporal expression
257 patterns (**Figure 4F and G**). In aggregate, our findings reveal overall similarities in
258 HSCPs' composition and differentiation potentials between the kidney and spleen,
259 suggesting analogous functionalities in hematopoiesis and immunity across both
260 organs. Nevertheless, the precise correlation between the fish kidney and spleen
261 requires further clarification.
262
263 **T and NK subsets in kidney**
264 Subdividing the T/NK category in Figure 1 led us to observe 23 subset clusters
265 (designated as T0–T22) enriched within the T/NK population through iterative
266 subclustering (**Figure 5A**). To validate the classification results, we assessed the most
267 variably expressed genes among cell clusters, and the heatmap demonstrated effective
268 classification for each cluster (**Figure 5B**). Subsequently, we analyzed the DEGs
269 within the 23 clusters. Notably, clusters T5, T17, and T18 were identified as NKT
270 subsets due to their widespread expression of NKT lineage genes, including *cd3ζ*, *trbc*,
271 *cd8a/cd4-1*, *zbtb32*, *nkl.2*, *il2rb* and *cd94* (**Figure 5C** and **Supplementary file 3**).

These NKT subset clusters exhibited substantial heterogeneity, as evident from their distinct transcriptional profiles, including the high expression of *vmp1*, *BX649554.1*, *nkl.2*, *stim1a*, *ccl36.1*, *CABZ01044746* in T5; *gata3*, *cpa5*, *tppp*, *si:dkey-78l4.7*, *si:dkey-78l4.4*, *cfbl*, *si:dkey-21e2.3.1*, *BX322787.1*, *si:dkey-9i23.4*, *si:dkey-78l4.6* in T17; and *ccl39.7*, *ccl39.6*, *nfil3−4*, *ccl35.2* in T18 (**Supplementary file 3**). Cluster T0 represented the $CD3^{low}CD4^{low}CD8^{low}$ T subset due to its low expression of *cd3ζ*, *cd4-1*, and *cd8a*. This subset likely represents an early developmental population of double positive (DP) T cells. Clusters T1 and T2 were identified as $CD8^{+}$-nkl.2 subsets exhibiting cytotoxic activity, as evidenced by the expression of *cd8a* and *nkl.2* (**Figure 5C** and **Supplementary file 3**). T3 was classified as a Th1 subset based on its expression of Th1-specific genes, including *cd4-1*, *ifng1*, *il2*, *cxcr3.1.1*, *tnfa*, and *tnfb*. Additionally, T3 expressed the cytotoxic T cell-related *gzmk* gene, suggesting its potential for both helper and cytotoxic activities (**Figure 5C** and **Supplementary file 3**). T4 was designated as a $CD4^{-}CD8^{-}$-nkl.4 subset due to its high expression of *nkl.4* and *trbc*, coupled with the absence of *cd4*/*cd8* expression and low *cd3ζ* expression. Continuing the narrative, clusters T6, T7, T10, T13, T19, T20, and T21 were categorized as NK subsets due to their expression of NK signature genes, including *zbtb32*, *nkl.2*, *il2rb*, and *cd94* (**Figure 5C** and **Supplementary file 3**). Among these, T19 exhibited no expression of *cd11b* or *cd27*, T7 expressed both *cd11b* and *cd27*, and T10, T13, T20, and T21 expressed *cd11b* but not *cd27* (**Figure 5C** and **Supplementary file 3**). These observations suggested that T19, T7, and T6/10/13/20/21 represented $CD11b^{-}CD27^{-}$, $CD11b^{+}CD27^{+}$, and $CD11b^{+}CD27^{-}$ subset NK cells, demonstrating high differentiation potential, cytokine secretion, and cytolytic functions as observed in humans[24]. Notably, each NK subset displayed distinct gene expression profiles, including the expression patterns of *her6*, *txn*, *id2a*, *mef2cb*, *zgc:162939* in T6; *hsp70.3*, *nkl.3*, *dicp1.1*, *nkl.4, ccl33.3* in T7; *cxcr4a*, *id1*, *phlda2*, *gnb5b*, *rasgef1ba*, *lgals2a*, *ctsbb*, *BX649442.1*, *enpp1* in T10; *nkl.2*, *nkl.3*, *nkl.4*, *fa2h*, *flt3* in T13; and *ctss1*, *eomesa*, *mafbb*, *mafa*, *si:ch73−180n10.1*, *CR388164.3*, *CR388164.2* in T19. Additionally, T20 and T21 cells specifically expressed *grn2* and *diabloa*, respectively (**Supplementary file 3**). These findings underscored the heterogeneity and functional diversity of zebrafish NK subsets. Clusters T8, T9, and T15 were identified as a group of $CD8^{+}$ CTL subsets, expressing $CD8^{+}$ CTL-specific genes, including *cd8a*, *cd8b*, *gzma*, *gzmk*, *ifng1*, and *tnfb* (**Figure 5C** and **Supplementary file 3**). T11 was labeled as a γδ T subset due to its high expression of *trgc*, *trdc*, *sox13*, and *cd3ζ*, combined with low expression of *cd4-1* and *cd8a*. This γδ T subset also exhibited high expression of *il2*, a pivotal cytokine gene involved in diverse immune activities (**Figure 5C**). T12 was classified as a Th17 subset due to its expression of lineage-specific genes, including *roraa*, *stat3*, *il17a/f3*, *il21*, *cd4-1*, *ccr6a*, *rorc*, *cd3ζ*, *il22*, *tgfb1a* and *il17a/f1*. T14 represented a distinctive

311 $CD4^+IgM^+$ subset characterized by the concurrent expression of *ighm* and *cd4-2.2*.
312 Cluster T16 was designated as a regulatory T (Treg) subset based on the expression of
313 *foxp3a*, *foxp3b*, *ctla4*, *cd4-1*, and *il17ra1a* marker genes (**Figure 5C** and
314 **Supplementary file 3**). T21 was indicative of a Th2-like subset, demonstrated by its
315 expression of Th2-associated genes, including *cd3ζ*, *il4*, *gata3*, *il13*, *stat6*, *batf* and
316 *cxcr4b*. Notably, this subset exhibited elevated expression of *faslg*, a pivotal apoptotic
317 inducer contributing to T cell cytotoxicity (**Figure 5C, Figure 9D**).
318
319 **B cell subsets in kidney**
320 Nine subclusters of B cells (designated as B0–B8) were classified through
321 unsupervised clustering of all B cells, based on their expression of distinct B-subset
322 signature genes (**Figure 6A and B**). B0 and B3 were designated as immature/mature
323 B cells (im/mat. B) due to their expression of *zfpm1* and *gata1a* genes (**Figure 6A**
324 **and B**). B1 was categorized as a canonical IgM^+IgD^+ B subset, characterized by its
325 high expression of *ighm* and *ighd* genes. B2 and B7 were identified as pro/pre B
326 subsets, exhibiting significant expression of *pclaf*, *pdia4*, *pdia6*, *rag1*, and *rag2* genes.
327 B4 likely represented a population of plasma cells that highly expressed *ighm* or *ighz*
328 (**Figure 6A and B**). B5 displayed expression of genes related to germinal-center B
329 cells, including *aicda* (AID), *mki67*, *top2a*, *stmn1a*, *bach2b*, *bcl6aa*, *bcl6ab*, *cd81a*,
330 *cd9a*, *irf8*, *lmo2*, *pclaf* and *nfkb2*, which exhibited a notable increase following virus
331 infection (**Figure 6A-C** and **Supplementary file 4**). Cluster B6 comprised activated
332 B cells and plasmablasts (act. B/PBs), actively expressing *dscamb*, *cpa5*, *fcer1g*,
333 *mmp13a.1*, *mpx*, *timp2b*, *npsn*, *il1b* and *lect2l*. It's worth noting that B6 also expressed
334 *il10* and *tgfb1a*/*b*, suggesting the potential presence of a regulatory B cell type within
335 this subcluster (**Figure 6A and B**). B8 was recognized as a B1-like subset with
336 heightened immune activities, including chemokine production, based on its
337 expression of *cd5*, *ccl33.3*, *ccl34b.4*, *nkl.4*, *tnfrsf18*, *nkl.2*, *sla2* and *hmgn3* genes
338 (**Figure 6A and B**). Interestingly, a distinct subset of $IgM^+\beta^+$ cells was identified
339 within B8 (**Figure 6A and B**). This lineage, known as dual expresser (DE),
340 simultaneously expressing TCR and BCR, has been reported in humans and is also
341 present in the spleen of zebrafish[15,25]. The top 10 subset-specific genes with the
342 greatest significance for each B-cell subset are visualized in a heatmap (**Figure**
343 **6—figure supplement 1B**). An analysis of the top 10 significantly enriched GO terms
344 within the biological process (BP) for each B-cell subset was conducted. The results
345 revealed varying metabolic processes enriched in each subset. For example, protein
346 export emerged as a major BP category and the most notable KEGG pathway in
347 plasma cells (**Figure 6—figure supplement 2E**). This outcome aligns with the
348 understanding that plasma cells are actively engaged in antibody synthesis and
349 secretion, underscoring the importance of protein synthetic metabolism in humoral

350 immune responses[26,27]. Moreover, (im)mat. B subset cells exhibited significant
351 enrichment in antigen processing and presentation BP pathways (**Figure 6—figure**
352 **supplement 2F**). This finding is congruent with prior evidence highlighting the robust
353 antigen presentation capability of teleost fish B cells, contributing to the initiation of
354 naïve $CD4^+$ T cell activation in adaptive humoral immunity[28,29]. Additionally, the
355 translation process displayed enrichment across all B-cell subsets, indicative of
356 ongoing protein synthesis during B cell development and maturation (**Figure**
357 **6—figure supplement 2A-D**). These observations provide substantive support for
358 subset classification from the perspective of cellular metabolism. Subsequently,
359 Monocle2 pseudotime analysis was performed on B-cell subsets using Monocle to
360 unveil potential relationships among different subsets during B-cell development.
361 Distinct pseudotime trajectory states of the B-cell subsets were delineated and are
362 presented in **Figure 6D-F**. Among these subsets, pro/pre B (B2), B1-like (B8), and
363 germinal center B-like cells (B5) occupied state 1, representing the initial
364 differentiation phase, followed by the im/mat. B (B0 and B3), IgM^+IgD^+ B (B1), act.
365 B/PBs (B6), and plasma (B4) cells. Notably, the identified B2, B5, and B8 clustered
366 together in a single branch, while B0, B3, and B7 progressively differentiated into B6
367 and eventually into B4 (**Figure 6F**). To explore the regulation of B-cell differentiation,
368 a pseudotime analysis was conducted on the genes significantly altered within these
369 clusters. These genes were categorized into three modules based on their
370 pseudotemporal expression patterns, thereby yielding potential key regulators of
371 teleost B-cell development (**Figure 6G, Figure 6—figure supplement 1E**).
372
373 **Heterogeneity of kidney macrophage/myeloid cells**
374 We categorized kidney macrophage/myeloid cells into 10 distinct subclusters
375 (designated as M0-M9) using a resolution of 0.3, as depicted in **Figure 7A-C**. A
376 heatmap showcasing the top ten most significant subset-specific genes for each
377 subcluster is provided in **Figure 7B**. M0, M1 and M7 cells were identified as
378 M1-typical macrophages expressing marker genes such as *tnfa*, *il6*, *il1b*, *il12a*, *stat1a*,
379 *mpeg1.2*, *mhc1zba*, *mhc2dab*, *cd83*, *cd74a*, *cd68*, *ccr7*, *selp* and *il15ra*, suggesting
380 their engagement in inflammatory responses (**Figure 7A-C** and **Supplementary file**
381 **5**). Both M2 and M5 subclusters exhibited active expression of genes associated with
382 common APC macrophages, including *mhc1zba*, *mhc2dab*, *cd83*, *cd74a* for M2, and
383 *mpeg1.1*, *mpeg1.2*, *mhc1zba*, *mhc2dab*, *cd83*, *cd74a*, *CR318588.1*, *CR318588.2*,
384 *CR318588.3* for M5, implying their role in antigen presentation (**Figure 7A-C** and
385 **Supplementary file 5**). M3 and M8 were characterized as M2-typical macrophages,
386 demonstrated by their high expression of M2 macrophage-related genes like *cd209*,
387 *il10*, *tgfb1a*, *tgfb1b*, *ly86* (*cd80/86*), *cd4-1*, *mpeg1.1*, *mpeg1.2*, *mhc2b*, *mhc2dab*, *cd83*
388 and *cd74a* (**Figure 7A-C** and **Supplementary file 5**). M4 was classified as a

389 macrophage-*isg15* population, expressing *mpeg1.1*, *mpeg1.2*, *mhc1zba*, *mhc2dab*,
390 *cd83*, *cd74a*, along with interferon-inducible genes *ifi45*, *isg15* and *ifi27.2*
391 (*zgc:152791*), underscoring its significant role in IFN-mediated immune responses
392 (**Figure 7A-C** and **Supplementary file 5**). M6 cells exhibited the expression of genes
393 related to eosinophils, including *fabp3*, *gtpbp4*, *ddx21*, *cldni*, *cd11b*, *cd44b*, *ackr3b*,
394 indicating their resemblance to eosinophil population (**Figure 7A-C** and
395 **Supplementary file 5**). M9 cells represented a group of dendritic cells (DCs)
396 extensively expressing lineage marker genes such as *zbtb46*, *scpp8*, *mmp13a.1*, *mmp9*,
397 *mpx* and *cpa5*. This DC group encompassed various DC populations, including
398 classical DC (cDC), plasmacytoid DCs (pDC), and a distinct $C1q^{+}DC$ (highly
399 expressing *c1qa*, *c1qb*, and *c1qc*), each expressing their respective subset marker
400 genes independently (**Figure 7A-C** and **Supplementary file 5**)[30].
401
402 **Heterogeneity of kidney neutrophils**
403 Neutrophils comprise the most prevalent subset of kidney leukocytes,
404 constituting 45.00% within the immune-cell categories (clusters 0, 2, and 9 in Figure
405 1), and accounting for 38.15% of the total sequenced cells in both the control and
406 SVCV-infected groups (**Figure 9A and B**). Subsequently, we undertook an analysis of
407 neutrophil heterogeneity. Through iterative subclustering within the neutrophil
408 category alone, we derived six distinct subgroups (designated as N0–N5) (**Figure 8A**
409 and **Supplementary file 6**). A heatmap was constructed to display the top 10 most
410 significant DEGs within each subcluster (**Figure 8C**). Subsequent annotation of each
411 subcluster was performed based on their unique biological functions and signaling
412 pathways utilizing GO and KEGG analyses (**Figure 8D and E, Figure 8—figure**
413 **supplement 1**). N0 exhibited functional enrichment in the C-type lectin receptor
414 pathway. This subset displayed heightened expression of *tcnbb*, *marcksl1b*, *pglyrp5*,
415 *irf1b*, *f3b*, *afap1l1b* and *stat1a*, implying its engagement in innate antiviral immune
416 responses (**Figure 8D** and **Supplementary file 6**). The biological focus of N1
417 centered on the endocytosis pathway (**Figure 8E**). Furthermore, this population
418 prominently expressed *scpp8*, *rab44*, *s1pr4*, *hbba1*, *crip1*, *hbaa1* and *hbba1.1*,
419 underscoring its pivotal role in the respiratory processes of neutrophils
420 (**Supplementary file 6**). N2 neutrophils were notably linked with the ribosome
421 pathway (**Figure 8—figure supplement 1**), actively manifesting expression of *cfd*,
422 *fabp3*, *ssr3*, *rpl22l1*, *ssr2*, *eef1g*, *rpl7*, *rplp2l*, *rpl15* and *rpl7a* genes that are
423 indispensable for the alternative pathway of complement activation, cytoplasmic
424 translation, intracellular metabolism, and other facets of innate immune response
425 (**Supplementary file 6**). N3 subpopulation exhibited evident involvement in oxidative
426 phosphorylation and interferon-mediated antiviral responses, as discerned from robust
427 expression of genes such as *txn* (thioredoxin), *ifi45* and *ifi46* (interferon

428 alpha-inducible protein 27.1 and 27.4), *si:dkey−188i13.6* (interferon alpha-inducible
429 protein 27.3), *zgc:152791* (interferon alpha-inducible protein 27.2), *CR318588.1*,
430 *CR318588.2*, *CR318588.3*, alongside other IFN-induced genes (**Figure 8—figure**
431 **supplement 1** and **Supplementary file 6**). N4 subcluster was typified by elevated
432 expression of diverse immune-relevant genes, including *jdp2b*, *fosab*, and *nr4a1*, with
433 primary functional enrichment in the MAPK signaling pathway (**Figure 8—figure**
434 **supplement 1** and **Supplementary file 6**). Finally, N5's functional enrichment
435 revolved around the cell cycle process, evidenced by the prominent expression of
436 *h2afx* (H2A.X variant histone), *tuba8l* (tubulin alpha 5), *top2a* (DNA topoisomerase II
437 alpha), *mki67* (marker of proliferation Ki-67), *hist1h4l.12*, and *hmgb2b* (high mobility
438 group box 2b), aligning closely with the architectural organization of genomic DNA
439 (**Figure 8—figure supplement 1** and **Supplementary file 6**).
440
441 **Response of kidney HSPCs and immune-cells to SVCV infection**
442 We subsequently investigated alterations in HSPCs and immune cell categories
443 following SVCV infection to assess the potential involvement of these cells in
444 antiviral immunity. The results revealed considerable changes in the abundance of
445 most categories after seven days of SVCV challenge. Specifically,
446 macrophage/myeloid cells (cluster 1), neutrophils 2 (cluster 2), and HSPCs 2 (cluster
447 6) exhibited an overall increase from 12.61% to 17.30%, 3.40% to 11.70%, and
448 1.64% to 9.72%, respectively (**Figure 9A and B**). Conversely, neutrophils 1 (cluster
449 0), T/NK (cluster 5), and HSPCs 3 (cluster 8) demonstrated an overall decrease from
450 39.72% to 23.51%, 11.29% to 5.16%, and 6.27% to 2.08% (**Figure 9A and B**).
451 Notably, several subset cells within the neutrophil category displayed marked changes
452 following SVCV infection. For instance, N0, N2, and N3 cells exhibited increases
453 from 3.45% to 41.26%, 6.75% to 17.31%, and 0.10% to 26.05%, respectively,
454 significantly contributing to the overall rise in neutrophils 2 (cluster 2 in Figure 1). By
455 contrast, N1 and N4 cells decreased from 71.87% to 1.30% and 13.64% to 6.69%
456 (**Figure 8A and B**). In the T/NK cell category, the abundance of NK (T6, T7, T13,
457 T21), NKT (T5, T17), Th2-like (T22), and Th17 (T12) cells increased from 3.64% to
458 6.58%, 3.82% to 5.97%, 2.78% to 3.52%, 0.52% to 1.23%, 5.38% to 7.50%, 1.82% to
459 2.30%, 0.69% to 2.60%, and 1.65% to 3.52%, respectively (**Figure 9C and E**).
460 Conversely, Th1 (T3) and Treg (T16) cells decreased from 11.01% to 5.36% and
461 2.43% to 1.68%, accompanied by a decrease in $CD8^+$ CTLs (T8, T9, and T15)
462 (**Figure 9C and E**), whose activation is regulated by Th1 cells[31,32]. Simultaneously,
463 the expression of these cell related genes was significantly downregulated (**Figure**
464 **9F**). In the macrophage/myeloid category, populations such as M1, M2, M4, and M5
465 experienced significant increases from 3.24% to 14.72%, 0.44% to 10.60%, 0.09% to
466 22.97%, and 0.09% to 23.26%, respectively, contributing to the overall category cell

467 increase (**Figure 7D and E**). By contrast, M1-type (M0, M7) and M2-type (M3, M8)
468 macrophages, decreased from 30.56% to 11.43%, 27.50% to 2.59%, 23.12% to 8.01%
469 and 9.02% to 0.65% (**Figure 7D and E**). Among B-cell subsets, the abundance of
470 (im)mat. B (B0) cells exhibited a significant decline from 51.08% to 22.10%, leading
471 to a partial decrement in total B cells (**Figure 6A and C**). Correspondingly, KEGG
472 analysis indicated that DEGs in (im)mat. B cells were primarily associated with
473 apoptosis, ferroptosis, necroptosis, phagosome, and mitophagy, as reflected by the
474 significant transcriptional up-regulation of related genes including *gsdmea*, *bcl2l1*,
475 *acsl4b*, *alox5a*, *prf1.7.1*, *il1b*, *gpx4a*, *gpx4b*, *atf3*, *aco1*, *atg13*, *casp3a*, *casp3b*, *apaf1*,
476 *casp9* and *casp8l2* (**Figure 6—figure supplement 1C and D**), suggesting that the B0
477 subset experienced severe cell death upon infection. However, the proportion of
478 common $IgM^{+}IgD^{+}$ B (B1), pro/pre B (B2), and germinal center B-like (B5) subsets
479 increased from 12.74% to 27.46%, 5.29% to 20.57%, and 2.05% to 10.83%,
480 respectively (**Figure 6A and C**). Within HSPC categories, cycling HSPCs (H1),
481 HSPCs 3 (H3), and HSPCs 4 (H4) exhibited increases from 6.06% to 24.59%, 0.32%
482 to 15.25%, and 0.32% to 16.22%, respectively. Conversely, HSPCs 1 (H0), HSPCs 2
483 (H2), myeloid progenitors (H6), erythrocyte progenitors (H7), lymphoid progenitors
484 (H8), and endothelial progenitors (H9) experienced significant declines from 27.81%
485 to 19.87%, 12.43% to 6.93%, 9.24% to 4.26%, 17.69% to 1.18%, 6.14% to 1.54%,
486 and 11.00% to 2.10%, respectively (**Figure 2D and E**). These observations
487 underscore the extensive response of kidney HSPCs and immune cells to SVCV
488 infection.
489
490 **Interferon-producing cells and key virus-responsive genes**
491 Interferons (IFNs) play pivotal roles in the defense against viral infections. In
492 this study, we delved into the transcriptional profiles of zebrafish IFNs, specifically
493 IFNϕ1-3 (*ifnphi1-3*), IFN-γ (*ifng1-2*), and IFNγ1R (*ifng1-1*), across various kidney
494 HSPCs and immune cells[33,34]. The findings revealed varying degrees of detection for
495 *ifnphi1*, *ifnphi2*, *ifnphi3*, *ifng1-1*, and *ifng1-2* in most HSPCs and immune cells before
496 and after SVCV infection (**Figure 10A and B**). Pre-SVCV infection, *ifng1-1*, *ifng1-2*,
497 and *ifnphi2* were primarily expressed in T/NK cells (cluster 5) and HSPCs 2 (cluster 6)
498 at different basal levels, with the highest expression seen in T/NK cells (**Figure 10C**).
499 Conversely, *ifnphi1* exhibited widespread expression in such as HSPCs 2 (cluster 6),
500 B cells (cluster 3), HSPCs 3 (cluster 8), and macrophages/myeloid cells (cluster 1),
501 with its peak in HSPCs 2 (cluster 6), followed by B cells (**Figure 10C**). Additionally,
502 *ifnphi3* showed extensive expression in HSPCs 2 (cluster 6), HSPCs 3 (cluster 8),
503 neutrophils 2 (cluster 2), B cells (cluster 3), and kidney mucin cells (cluster 11)
504 (**Figure 10C**). Post-SVCV infection, *ifng1-1*, *ifng1-2*, *ifnphi1*, and *ifnphi3* were
505 notably up-regulated to varying extents in most corresponding cells. Specifically,

506 *ifnphi1* and *ifnphi3* exhibited increased expression in kidney multiciliated cells
507 (cluster 7) and neutrophils 3 (cluster 9) upon infection (**Figure 10C**). However, the
508 expression of *ifng1-2* in HSPCs 1 (cluster 4), HSPCs 2 (cluster 6), and HSPCs 3
509 (cluster 8), *ifnphi3* in kidney mucin cells (cluster 11), neutrophils 2 (cluster 2), and
510 HSPCs 2 (cluster 6), and *ifng1-1* in HSPCs 2 (cluster 6) experienced a decline
511 (**Figure 10C**). Overall, *ifnphi1* displayed the most significant up-regulation, while
512 *ifng1-2* exhibited the highest expression upon challenge of SVCV, despite its
513 downregulation trend under infection. This latter response indicated that IFN-γ
514 actively participates in antiviral immunity alongside the previously recognized
515 predominant role of type I IFN in antiviral defense[35,36]. Notably, *ifnphi4* and *ifnu* were
516 barely detectable post-SVCV infection, suggesting that IFNϕ4 and IFN-υ may play
517 distinct functional roles in zebrafish defense against different pathogens.
518 We next investigated the key virus-responsive genes beyond interferons. By
519 employing Model-based Analysis of Single-cell Transcriptomics (MAST), we
520 identified the most significantly up-regulated genes in the DEGs of all kidney
521 immune-cell categories. The results demonstrated a robust response of most immune
522 cells to SVCV infection, evident from the considerable up-/down-regulation of
523 numerous genes in these cells (**Figure 10D and E**). From the list of top up-regulated
524 genes, six stood out as displaying the strongest responsiveness to SVCV infection.
525 These genes included *isg15* (ISG15 ubiquitin-like modifier), *CR318588.1*,
526 *zgc:152791* (interferon alpha-inducible protein 27.2, *ifi27.2*), *ifi45* (interferon
527 alpha-inducible protein 27.1, *ifi27.1*), *CR318588.2*, and *CR318588.3* (**Figure 10F-J,**
528 **Figure 10—figure supplement 1**). Remarkably, *isg15*, *CR318588.1*, *ifi45*, and
529 *zgc:152791* were prominent across almost every cluster (**Figure 10F**). These findings
530 underscore the pivotal roles of these six genes in zebrafish antiviral immunity. To
531 validate the scRNA-seq analysis, we examined the expression levels of *isg15*,
532 *CR318588.3*, *zgc:152791*, *ifi45*, and *CU984600.2* in kidney T-/B-cell populations
533 using RT-qPCR. Consistently, these genes exhibited significant upregulation upon
534 SVCV insult, confirming their responsiveness to viral infection (**Figure 10K and L**).
535 Notably, the *isg15*, *ifi45*, and *ifi27* homologs are recognized to play crucial roles in
536 host antiviral immunity through interaction with IFN-α/β in mammals[37,38]. This
537 identification of *isg15*, *ifi45*, and *ifi27* in zebrafish suggests their conserved roles in
538 IFN-associated immunity across vertebrate evolution from fish to mammals. However,
539 the functional roles of *CR318588.1*, *CR318588.2*, *CR318588.3*, and *zgc:152791*
540 (*ifi27.2*, another variant of *ifi27*) in host antiviral immunity remain understudied.
541 Consequently, further investigation is warranted to fully grasp their contributions to
542 host immune defense against viral infections.
543
544 **Trained immune response of HSPCs to SVCV**

545 Numerous studies have documented the phenomenon of enhanced resistance in
546 innate immune cells such as macrophages and neutrophils upon reinfection with the
547 same or unrelated pathogens, a phenomenon termed trained immunity[39-41].
548 Furthermore, Bacillus Calmette-Guerin (BCG) has been found to induce trained
549 immunity in hematopoietic stem cells (HSCs) and multipotent progenitors (MPPs),
550 promoting augmented myelopoiesis at the expense of lymphopoiesis[42,43]. In this study,
551 we investigated the potential induction of trained immunity in innate immune cells
552 and HSPCs within the kidney upon stimulation by SVCV. To this end, zebrafish were
553 immunized with the SVCV vaccine for 14 days and subsequently exposed to virulent
554 SVCV for another 7 days. The outcomes demonstrated a substantial reduction in the
555 proportion of neutrophils within cluster 0 following SVCV infection. However, this
556 population exhibited minimal reduction in vaccinated zebrafish (referred to as
557 "trained zebrafish") upon the second SVCV challenge (**Figure 11—figure**
558 **supplement 1**). Furthermore, the abundance of HSPCs 1 within cluster 4 remained
559 unchanged after SVCV infection, yet experienced significant expansion during the
560 second SVCV challenge in trained zebrafish (**Figure 11—figure supplement 1**).
561 Notably, the H0 subset exhibited the most pronounced response to trained immunity
562 to SVCV within the HSPC categories (**Figure 11A**). Specifically, the proportion of
563 H0 decreased from 27.81% in the PBS group to 19.87% in the SVCV group, then
564 rapidly surged to 41.43% in the vaccinated + SVCV group. This trend was supported
565 by the significant upregulation of numerous immune-related genes within H0 subset
566 cells of trained zebrafish (**Figure 11B**). Thus, the shift in the H0 subset played a
567 pivotal role in the overall heightened activity of the HSPCs 1 category within trained
568 zebrafish. Collectively, these findings underscore an intensified immune response in
569 kidney HSPCs of zebrafish subsequent to SVCV vaccination, suggesting the
570 inducement of trained immunity in zebrafish kidney HSPCs for the generation of a
571 memory response to SVCV infection. Furthermore, the neutrophils within the kidney
572 of trained zebrafish exhibited enhanced antiviral immunity, showcasing potential
573 innate immune memory characteristics.
574
575 **Infection of SVCV in kidney immune cells**
576 To delineate the potential immune cells susceptible to SVCV infection, we
577 investigated the transcription of five subgenomic RNAs/genes (sgRNAs) encoding N,
578 P, M, G, and L proteins during the SVCV replication cycle across diverse kidney
579 immune-cell categories, following our recently described approach[15]. Applying an
580 unsupervised cluster detection algorithm, we identified 10 clusters characterized by
581 similar gene expression profiles. Importantly, the integration of viral sgRNA
582 sequences into the kidney scRNA-seq datasets revealed an overall preservation of the
583 composition of immune-cell categories (**Figure 12A**). Subsequently, we scrutinized

584 the transcripts of the five sgRNAs in scRNA-seq datasets from both control and
585 SVCV-infected zebrafish. As anticipated, the five sgRNAs were present in cells from
586 infected fish but absent in those from control fish, validating the effectiveness of our
587 integration method (**Figure 12B**). The representation of cells transcribing N-, M-, P-,
588 G-, and L-protein encoding sgRNAs exhibited proportional variation, with
589 approximately 0.15% of cells carrying sgRNA for N protein, followed by M (0.12%),
590 P (0.12%), G (0.06%), and L (0.03%) proteins, respectively (**Figure 12C**). This
591 distribution aligns with prior observations, confirming the heightened prevalence of N
592 protein transcripts in SVCV-infected cells, followed by those for M, P, G, and L
593 proteins[44-46]. Refining our analysis to specific cell types, we discerned that viral
594 sgRNAs were predominantly detected in macrophage/myeloid cells within cluster 3
595 and 9. This observation strongly implies that macrophage/myeloid cells are the
596 prevailing cell types supporting productive viral replication in zebrafish kidney
597 (**Figure 12D**).
598
599 **Experimental assay for adaptive immunity occurring in kidney**
600 The aforementioned observations underscore the immunologically responsive
601 nature of the fish kidney, revealing innate and adaptive immune activities that extend
602 beyond its previously recognized role in hematopoiesis. Among these activities,
603 adaptive immunity has traditionally been attributed to secondary lymphoid organs
604 such as the spleen and lymph nodes[9,47]. This study offers experimental confirmation
605 for the occurrence of adaptive immunity in the zebrafish kidney following viral
606 stimulation. To this end, zebrafish were exposed to inactivated SVCV (10^6
607 TCID50/fish) for 7 days, and the activation of kidney T and B cells was assessed by
608 quantifying their heightened proliferation and increased expression of CD154 and
609 CD40 costimulatory molecules through flow cytometry and RT-qPCR. As anticipated,
610 $CD4^+$ T, $CD8^+$ T, and IgM^+ B cells exhibited significant proliferation in the kidneys of
611 zebrafish stimulated with SVCV compared to control fish that received mock PBS
612 (**Figure 13A-D**). In tandem, the transcriptional levels of CD154 and CD40 genes
613 displayed marked upregulation, concurrent with the proliferation of $CD4^+$ T, $CD8^+$ T,
614 and IgM^+ B cells (**Figure 13E and F**). Importantly, parallel activation of $CD4^+$ T,
615 $CD8^+$ T, and IgM^+ cells was also discerned in the spleens of SVCV-stimulated
616 zebrafish (**Figure 13G**). These results suggested that the zebrafish kidney assumes a
617 central role in orchestrating adaptive immune responses to viral infection, a role that
618 may be comparable to that of the spleen, a well-known secondary lymphoid organ
619 crucial for initiating and advancing adaptive immunity. To substantiate this
620 perspective, we proceeded to investigate the occurrence of SHM, a hallmark event
621 driving antibody affinity maturation in adaptive humoral immunity, within kidney B
622 cells upon antigenic stimulation. We employed RT-qPCR to examine the expression of

623 the zebrafish AID gene (*aicda*), a pivotal initiator of SHM. As anticipated, AID
624 transcript presence was evident in the zebrafish kidney, and its expression
625 significantly increased in response to SVCV stimulation (**Figure 13H**).
626 Correspondingly, SHM was identified in kidney B cells through PCR-based
627 high-throughput sequencing. Notably, the frequency of mutagenesis within V regions
628 (V4-9) of IgM genes demonstrated a substantial antigen-dependent increase (**Figure**
629 **13I**). These findings offer novel insights into the dual-functionality of the zebrafish
630 kidney, encompassing both hematopoietic and adaptive immunological
631 responsiveness. This suggests that the fish kidney operates as a unique organ
632 amalgamating the roles typically associated with primary and secondary lymphoid
633 tissues.
634

635 **Discussion**

636 The immune system constitutes a complex evolutionary entity marked by
637 significant heterogeneity and structural-functional diversity across various taxa. The
638 origin and phylogenetic evolution of the vertebrate immune system captivates the
639 attention of comparative immunologists, particularly concerning teleost fish due to
640 their pivotal phylogenetic standing. In human and other mammalian organisms, the
641 immune system encompasses primary and secondary lymphoid organs[11,47], the former
642 including bone marrow and thymus, facilitating hematopoiesis, lymphocyte
643 maturation, and functional development[47,48]. Secondary lymphoid organs, including
644 lymph nodes, spleen, and sections of mucosal immune systems, trigger the activation
645 of naïve lymphocytes by antigens, thereby initiating and advancing adaptive immune
646 responses[11,49,50]. In contrast to mammals, teleost fish lack bone marrow and lymph
647 nodes. Instead, the anterior section of the fish kidney (referred to as the head kidney)
648 emerges as an operational analog of mammalian bone marrow in adult fish.
649 Accordingly, the fish kidney functions as the primary hematopoietic site, overseeing
650 the generation of circulating blood cell lineages and B cell maturation[51-53].
651 Furthermore, the fish kidney is also thought to be an immunologically responsive
652 organ capable of eliciting immune responses against a spectrum of pathogens,
653 including bacteria, viruses, and parasites[26,27]. These findings establish the kidney's
654 pivotal role in fish immunity, although a comprehensive understanding of the cellular
655 components and their attributes within the hematopoietic process and immune
656 responses in the fish kidney remains elusive.
657 To address these gaps, we conducted a single-cell RNA sequencing (scRNA-seq)
658 analysis of kidney leukocytes in zebrafish, unraveling the spectrum of hematopoietic
659 and immune-associated cell types in adult fish. We identified 13 distinct cell
660 categories, spanning three groups of HSPCs, six cohorts of innate and adaptive

661 immune-related cells, and four renal cell types, which emerged as byproducts of
662 cellular preparation. Further subdivisions of the three HSPC groups led to the
663 identification of 11 potential subpopulations, each marked by unique gene expression
664 profiles. Notable subsets, such as Nanos1^{+}Spi2^{+} HSPCs and cycling HSPCs, bore
665 resemblances to previously described counterparts[17]. Moreover, six subsets exhibited
666 the characteristics of progenitor cells, demonstrating both marker gene expression and
667 the capacity to differentiate into diverse blood cell lineages encompassing NK cells,
668 myeloid cells, lymphoid cells, erythrocytes, and thrombocytes. Yet, the properties of
669 certain HSPC subsets, like H2, H3, and H4, remain undefined. Such subsets exhibit
670 distinct gene expression profiles, which could potentially serve as candidate
671 signatures for future subset classification. Correspondingly, numerous committed or
672 terminal cell lineages, intricately associated with these HSPCs, were detected in the
673 kidney. These lineages encompass a range of innate and adaptive immune-related
674 cells at various developmental stages, prominently featuring neutrophils, macrophages,
675 dendritic cells, NK cells, and various T and B cell subsets. Moreover, early
676 developmental cells such as double negative (DN) T cells, double positive (DP) T
677 cells, pro/pre B cells, and immature/mature B cells were found in the kidney. These
678 cells are major committed immature or partially mature T and B lymphocytes at early
679 stage of hematopoiesis, among them, the DN and DP T cells will enter the thymus,
680 where they complete their maturation and maturing selection[17], while pro/pre B and
681 im/mat B cells may continue to mature or partially mature in the kidney. These
682 insights underscore the presence of diverse HSPCs fostering various blood cell
683 lineages and reinforce the concept that the fish kidney functions as a primary
684 lymphoid organ, mirroring the role of mammalian bone marrow[54,55].
685 Comparatively, human hematopoietic stem cells (HSCs) are characterized by
686 surface markers (such as CD34 and c-kit), coupled with the absence of
687 lineage-specific markers typical of mature cells[56,57]. HSCs yield common
688 myeloid-lymphoid progenitors (CMLPs) and common
689 myeloid-megakaryocyte-erythroid progenitors (CMMEPs). While CMLPs give rise to
690 committed T and B cell precursors, ILCs, and certain myeloid cells, CMMEPs
691 produce precursors for erythroid, megakaryocytic, monocytic, and granulocytic
692 lineages. These precursors subsequently develop into mature erythrocytes, platelets,
693 monocytes, and granulocytes, as well as dendritic cells and mast cells[58,59]. Notably,
694 zebrafish exhibited detectable elementary progenitors responsible for generating
695 principal blood cell lineages, suggesting the presence of conserved cellular
696 components and developmental pathways underlying adult hematopoiesis across
697 species. However, unresolved matters and fish-specific events within adult fish
698 hematopoiesis persist, such as distinguishing HSCs from multiple HSPCs.
699 Additionally, the existence of pluripotent common progenitors akin to CMLPs and

700 CMMEPs, as well as committed precursors for lymphocytic, erythroid,
701 megakaryocytic, monocytic, and granulocytic lineages, warrant clarification.
702 Although pseudotime trajectory and RNA velocity analyses have shed preliminary
703 light on relationships among partial HSPCs, the precise phenotypic features,
704 developmental trajectories, and correlations of these HSPCs necessitate thorough
705 elucidation. Unique HSPCs with unknown properties, like H0, H2, H3, and H4,
706 accentuate the high heterogeneity within HSPCs in adult fish. Given the considerable
707 number of fish-specific lineages, probing the relationship between these
708 uncharacterized HSPCs and fish-specific lineages remains a promising avenue of
709 exploration.

710 The extensive presence of immune cells associated with the kidney signifies the
711 central role of this organ in fish immunity, extending beyond its hematopoietic
712 function. Indeed, the kidney exhibited robust responsiveness to SVCV infection,
713 evidenced by significant changes in the abundance of diverse immune cells, including
714 both upregulated and downregulated subsets. Prominent upregulated populations
715 consisted of neutrophils (N0, N2, N3), NK (T6, T7, T13, T21), NKT (T5, T17), Th17
716 (T12), Th2-like (T22), common $IgM^{+}IgD^{+}$ B (B1), pro/pre B (B2), germinal center
717 B-like (B5) cells, and macrophages (M1, M2, M4, M5), indicating their engagement
718 in host defense against SVCV. Conversely, downregulated populations encompassed
719 subsets of neutrophils (N1, N4), $CD8^{+}$ T (T8, T9, T15), Th1 (T3), Treg (T16), im/mat.
720 B (B0), and M1-/M2-macrophages (M0, M3, M7, M8), implying their impairment
721 during SVCV infection. For example, the impairment of im/mat. B (B0) cells may be
722 caused by undergoing severe cell death under infection in this case, as determined by
723 their highly expression of death-associated genes related to apoptosis, ferroptosis, and
724 necroptosis. The reduction in this antibody-producing subset will attenuate the
725 humoral adaptive immune protection of fish from SVCV infection. Notably, we found
726 that the abundance of three HSPC subsets (H1, H3, and H4) were markedly
727 upregulated by 24.09-, 255.22-, 258.44-folds, respectively. By contrast, six other
728 HSPC subsets (H0, H2, H6, H7, H8 and H9) were downregulated, potentially
729 hampering the differentiation of downstream lineage cells and attenuating antiviral
730 immunity. Encouragingly, two HSPC subsets demonstrated the induction of trained
731 immunity upon stimulation with SVCV vaccine, subsequently challenged by virulent
732 SVCV. These findings not only underscore the role of HSPCs in viral responses but
733 also signify a novel dimension of HSPC involvement in viral infections. Previous
734 studies have highlighted the profound impact of infections on host immune
735 homeostasis in various viral disease models[60-62]. The consequences range from
736 excessive inflammation due to hyperactive immune responses to immune deficiency
737 resulting from ineffective responses, the latter of which potentially favoring immune
738 escape by viruses[61]. In the current study, multiple HSPCs and immune cell subset

739 disturbances were observed under SVCV infection, suggesting a potential role in
740 disease pathogenesis[63]. However, the exact mechanisms of the disturbance of HSPCs
741 and immune cells under infection remains to be studied, which will help clarify the
742 pathogenesis of viremia during SVCV infection from the perspective of
743 immunopathology.

744 The broader overview of kidney immune cell shifts in response to SVCV
745 challenge reveals extensive innate and adaptive immune responses within the kidney
746 during viral infections. This robust immune responsiveness aligns with the concept of
747 the fish kidney as a potent immune organ[64]. Particularly noteworthy, our investigation
748 revealed a diverse range of adaptive immune-associated cells inhabiting the zebrafish
749 kidney. These cells encompass various APCs, along with naïve T and B cells,
750 plasmablasts, and plasma cells—key cell types crucial for initiating, activating, and
751 executing adaptive immune responses. The profiles of adaptive immune cells within
752 the kidney, alongside their responses, closely resemble those observed in the
753 spleen—an evolutionarily conserved secondary lymphoid organ spanning vertebrates
754 from fish to mammals. Consequently, our findings strongly imply that the zebrafish
755 kidney might function as a secondary lymphoid organ, fostering the generation of
756 adaptive immunity through interactions among APCs and antigen-specific T and B
757 cells. To empirically substantiate this hypothesis, we examined the occurrence of
758 antigen-stimulated adaptive immune responses in the kidney. As anticipated, the $CD4^+$
759 T, $CD8^+$ T, and IgM^+ B cells exhibited pronounced activation in the zebrafish kidney
760 under SVCV challenge. This activation was underscored by significant proliferation
761 in $CD4^+$ T, $CD8^+$ T, and IgM^+ B cell populations, followed by upregulated
762 transcriptional expression of CD154 and CD40 genes on these cells. Furthermore, we
763 also observed the occurrence of antigen-induced expression of AID and SHM in the
764 kidney IgM^+ B cells, two hallmark events for the affinity maturation of antibodies in
765 adaptive humoral immunity. These results collectively establish the zebrafish kidney
766 as a distinct entity encompassing attributes of both primary and secondary lymphoid
767 organs, thus offering fresh insights into the dual functional roles of the fish kidney,
768 spanning hematopoiesis and adaptive immunity. While peripheral lymph nodes are
769 absent, the spleen has historically stood as the predominant secondary lymphoid organ
770 in fish. However, our current study introduces a novel member to the array of
771 secondary lymphoid organs. The intricate interplay between the roles of the kidney
772 and spleen in hematopoiesis and immune responses within fish warrants further
773 elucidation. Moreover, unraveling the structural foundations accommodating diverse
774 HSPCs and immune cell types and precisely orchestrating hematopoiesis and immune
775 responses within the kidney and spleen emerges as a compelling area of inquiry.
776 Addressing these queries necessitates the utilization of advanced techniques, such as
777 single-cell spatiotemporal transcriptomic analysis at the level of cross-organ

single-cell transcriptome profiling.

In summary, our study presents a comprehensive panorama of HSPCs and immune cell types within the zebrafish kidney under steady-state conditions, viral emergencies, and vaccine training. Our identification of a multitude of HSPCs, along with developmentally-linked progenitors and immune cell types, and their modifications under emergency and training scenarios, underscores the pivotal role of the kidney in fish defense against viral infections. Moreover, the revelation of trained immunity establishment within HSPCs holds significant implications for comprehending the novel pathways and mechanisms governing trained immunity formation. The paradigm shift—where the kidney, traditionally viewed as a primary lymphoid organ facilitating hematopoiesis—emerges as a secondary lymphoid organ, marks a pivotal transformation in understanding fish biology. Our study offers insights into the intricate and heterogeneous nature of the fish immune system, shedding light on the multifunctionality of the fish kidney, encompassing hematopoiesis, immune defense, waste excretion, and osmoregulation—mainstays of kidney function across diverse vertebrates.

Materials and methods

Experimental fish

Wild-type AB zebrafish (*Danio rerio*), with body weights ranging from 0.5 to 1.0 g and lengths of 3–4 cm, were reared under standard laboratory conditions. The fish were raised in recirculating water at a temperature of 28°C and exposed to a 12-hour light/12-hour dark cycle, as previously described[65,66]. Prior to their use in experiments, all fish were acclimated for a minimum of 2 weeks to ensure their overall health. Only zebrafish exhibiting robust general appearance and activity were selected for experimentation. All animal experiments were conducted in accordance with the guiding principles for the care and use of laboratory animals and were approved by a local ethics committee.

Cell line and virus

Epithelioma papulosum cyprini (EPC) cells were cultured in Medium 199 (M199, Gibco), supplemented with 10% (v/v) fetal bovine serum (FBS), and maintained at 28°C in a 5% CO_2. The spring viremia of carp virus (SVCV), provided as a gift by Prof. Yibing Zhang from the Institute of Hydrobiology, Chinese Academy of Sciences, was propagated in EPC cells at 28°C. The virus was subsequently titrated in 96-well plates until full cytopathic effect (CPE) was observed. Purification of SVCV from EPC cell culture was accomplished through sucrose gradient centrifugation at 100,000 g for 2 hours, as previously described[67]. The purified virus was suspended in sterile PBS and stored at -80°C until utilization. The viral titer was quantified as 1.58×10^7

817 $TCID_{50}$/ml, employing the 50% tissue culture infective dose (TCID50) assay on EPC
818 cells via the Reed-Müench method[68]. For the purpose of vaccination, SVCV was
819 inactivated with a final concentration of 0.4% (v/v) formaldehyde, followed by the
820 protocol as described[69].
821
822 **SVCV challenge**
823 Adult zebrafish were randomly divided into three groups, i.e. PBS-administered group
824 (control), SVCV-infected group (infected), and inactivated SVCV-vaccinated plus
825 virulent SVCV-infected group (vaccinated+infected). Each zebrafish in these groups
826 received an intraperitoneal injection of 10 μl of phosphate-buffered saline (PBS,
827 pH=7.0), 10 μl of virulent SVCV (10^3 $TCID_{50}$/fish), or 10 μl of inactivated SVCV
828 followed by 10 μl of virulent SVCV (10^3 $TCID_{50}$/fish). In the context of vaccination,
829 zebrafish were immunized with 10 μl of inactivated SVCV vaccine (10^5 $TCID_{50}$/fish)
830 for two weeks, succeeded by infection with virulent SVCV (10^3 $TCID_{50}$/fish) for an
831 additional week. Subsequently, kidney samples were collected at 7 days post-infection
832 (dpi) for the control and SVCV-infected groups and at 21 dpi for the
833 vaccinated+infected group. Equivalent quantities of tissue were pooled from each
834 group, and these samples underwent subsequent leukocyte isolation.
835
836 **Isolation of leukocytes**
837 Leukocytes were obtained from kidney samples utilizing Ficoll-Hypaque
838 density-gradient centrifugation, as previously described[28,65,70]. After 7 days of SVCV
839 challenge, zebrafish were euthanized with MS222. Kidney tissues were meticulously
840 excised and passed through a 40 μm stainless nylon mesh (Greiner Bio-One GmbH,
841 Germany). The resulting cell suspension was suspended in Leibovitz's L-15 Medium
842 (L-15, Gibco), supplemented with penicillin (100 U/ml, Sigma-Aldrich), streptomycin
843 (100 μg/ml, Sigma-Aldrich), and heparin sodium (10 U/ml, Sigma-Aldrich). This
844 suspension was then introduced into a Ficoll-Hypaque (1.080 g/mL) density-gradient
845 centrifugation, and subsequently centrifuged at 1,200 g for 25 minutes. The cellular
846 interface layer was cautiously aspirated, followed by a wash with ice-cold PBS at 400
847 g for 10 minutes. The viability and quantity of cells were assessed using 0.4% trypan
848 blue (Sigma, St. Louis, MO, USA), confirming the viability of over 95% of the cells.
849 Enumeration of cells for each group was executed using a cell counting plate.
850
851 **Single-cell RNA sequencing**
852 The library synthesis and RNA-sequencing were completed by the LC-Bio
853 Technology Co., Ltd (Hangzhou, China). In brief, the isolated leucocytes from
854 zebrafish kidney were applied to Red Blood Cell Lysis Buffer and the magnetic bead
855 separation method was used to remove red blood cells and dead cells. After cell

856 counting, an appropriate volume for capturing 10,000 cells was calculated. These cells
857 were mixed into a sample and adjusted to 700~1,200 cell/μl. Libraries were
858 constructed using the Chromium™ Controller and Chromium™ Single Cell 3'
859 Library & Gel Bead Kit v2 (10× Genomics) as per the manufacturer's protocol.
860 Cellular suspension was added to the master mix containing nuclease-free water, RT
861 Reagent Mix, RT Primer, Additive A and RT Enzyme Mix. Master mix with cells was
862 transferred to the wells in the row labelled 1 on the Chromium™ Single Cell A Chip
863 (10× Genomics). Single Cell 3' Gel Beads and Partitioning Oil were placed in specific
864 rows. The chip was loaded onto the Chromium™ Controller to create single-cell
865 GEMs. GEM-RT was conducted in a C1000 Touch Thermal cycler (Bio-Rad),
866 followed by cleanup with DynaBeads MyOne Silane Beads (Thermo Fisher
867 Scientific). Subsequent cDNA amplification and library construction adhered to
868 standard protocols. The library was multiplexed and sequenced on an Illumina
869 NextSeq-500 lane using a high-output (400 m) kit[71]. Quality control of 10× Genomics
870 single-cell RNA-seq was executed (**Figure 1—figure supplement 1**). For mapping,
871 sequences from the 10× Genomics single-cell RNA-seq platform were demultiplexed
872 and mapped to the mm10 transcriptome through the Cell Ranger package (10×
873 Genomics). The DoubletFinder R package identified and filtered doublets
874 (multiplets)[72]. The raw digital gene expression matrix (UMI counts per gene per cell)
875 from Cell Ranger analyses was filtered and normalized using the R package Seurat
876 (Version 3.1.1)[73]. Cells with fewer than 500 unique genes, over 50,000 UMI counts,
877 or more than 10% mitochondrial reads were removed. Undetected genes in any cell
878 were excluded. Post-filtration, cell counts were 9,004 in the PBS-administered group
879 (control), 9,890 in the SVCV-infected group (infected), and 8,487 in the
880 SVCV-vaccinated plus SVCV-infected group (vaccinated+infected).
881
882 **Downstream analysis of 10× Genomics data**
883 After log normalizing the data, a principal component analysis (PCA) was performed
884 to reduce dimension. The identification of significant clusters was performed using
885 the Find Clusters algorithm in the Seurat package, which uses a shared
886 nearest-neighbour modularity optimization-based clustering algorithm. Marker genes
887 for each significant cluster were found using the Seurat function FindAllMarkers. Cell
888 types were determined using a combination of marker genes identified from the
889 literature and gene ontology for cell types. Expression of selected genes was plotted
890 with the Seurat function FeaturePlot and VlnPlot. Hierarchical clustering and heat
891 map generation were performed for single cells based on log-normalized (with scale
892 factor 10,000 and pseudocount 1) expression values of marker genes obtained from
893 the literature or identified as highly differentially expressed. Heat maps were
894 generated using the heatmap.2 function from the gplots v3.5.2 R package using the

895 default complete-linkage clustering algorithm[74].
896
897 **Pseudotime trajectory analysis**
898 Pseudotime trajectory was plotted by using the R package monocle Version 2.22.0
899 with the default settings given there. Pseudotime ordering was performed using the
900 function “reduce dimension” with max_components set at 2 and reduction_method set
901 as DDRTree. Next, the significantly affected genes were obtained from the top 50
902 markers among the clusters by using the function differentialGeneTest
903 (fullModelFormulaStr = ~Pseudotime) and were plotted with the function
904 plot_pseudotime_heatmap. The num_cluster was set at 3 to obtain three modules of
905 significantly changed genes that had similar trends according to their pseudotemporal
906 expression patterns.
907
908 **RNA velocity analysis**
909 Cell RNA velocity analysis was performed using the velocyto (V0.17.17) program[75].
910 This approach uses the relative proportions of unspliced and spliced mRNA
911 abundance to provide insights into the anticipated future state of cells. Initial
912 annotation of spliced and unspliced reads was performed through the utilization of the
913 "velocyto.py" commandline tools. Subsequently, downstream analysis was performed
914 using the same "velocyto.py" framework. The resulting RNA velocity data represents
915 a vector that predicts the transition dynamics of individual cells, with the direction
916 and speed of each transition inferred from the amplitude and direction of the
917 individual cell velocity arrows plotted on a t-Distributed Stochastic Neighbor
918 Embedding (t-SNE) plot. By examining the directional flow within the RNA velocity
919 vector field, the hierarchical relationship between two cell populations can be
920 inferred.
921
922 **Pathway enrichment analysis**
923 Functional enrichment analyses, including Gene Ontology (GO) and Kyoto
924 Encyclopedia of Genes and Genomes (KEGG), were conducted to determine which
925 differentially expressed genes (DEGs) significantly enriched GO terms or metabolic
926 pathways. Given that GO is an international standard classification system for gene
927 function, DEGs are mapped to the GO terms (biological functions) in the database.
928 The number of genes in each term was calculated, and a hypergeometric test was
929 performed to identify significantly enriched GO terms in the gene list out of the
930 background of the reference gene list. GO terms and KEGG pathways with false
931 discovery rates $p < 0.05$ were considered as significantly different.
932
933 **Magnetic-activated cell sorting (MACS) and quantitative real-time PCR**

934 MACS was employed to isolate T and B cells from kidney leukocytes in both
935 SVCV-infected and PBS-administered (control) zebrafish. In this procedure,
936 leukocytes were initially blocked with 5% normal goat serum for 15 minutes at 10°C,
937 then incubated with rabbit anti-TCRα/β (1:200) or mouse anti-IgM Ab (1:200) for an
938 additional 15 minutes at 10°C. Subsequent washing with MACS buffer (PBS
939 containing 2 mM EDTA and 0.5% BSA) was followed by a 15-minute incubation at
940 10°C with anti-IgG magnetic beads (Miltenyi Biotec). The cell suspension was
941 introduced to a LS separation column following the manufacturer's instructions. Total
942 RNA was extracted from positive cells, kidney, and spleen tissues using an RNAiso
943 Plus kit (Takara Bio), and subsequently reverse transcribed into cDNAs. Quantitative
944 real-time PCR (RT-qPCR) was employed to analyze the transcript abundance of target
945 genes on a CFX Connect Real-Time PCR Detection System (Bio-Rad). The PCR
946 protocol encompassed a total volume of 10 μl with iTaq Universal SYBR Green
947 Supermix (Bio-Rad). Reaction mixtures underwent an initial incubation at 95°C for 2
948 minutes, succeeded by 40 cycles of 15 seconds at 95°C, 15 seconds at 60°C, and 20
949 seconds at 72°C. Relative expression levels were calculated using the $2^{-\Delta\Delta CT}$ method,
950 with β-actin as the reference gene. Each PCR trial comprised triplicate parallel
951 reactions, and each experiment was independently repeated at least three times. The
952 RT-qPCR primer sequences are detailed in **Supplementary file 7**.
953
954 **ScRNA-Seq differential expression analysis and SVCV reads enrichment**
955 Seurat package FindMarkers function with default parameters was used to perform
956 differential gene expression analysis between the control and treatment groups of the
957 same cell type. Within the FindAllMarkers function, the Wilcoxon rank-sum test was
958 applied to assess single-cell differential gene expression for identified cell subsets.
959 Marker genes for each cluster were determined by contrasting them with all other
960 cells in the experiment. Differential gene expression, reflecting diverse levels of
961 upregulation and downregulation in different comparisons, was depicted through
962 volcano plots. Enrichment of reads across SVCV genes was analyzed using the
963 Integrative Genome Viewer to identify read pileups[76,77]. Cells containing any counts
964 to viral genes were categorized as positive for viral RNA.
965
966 **Flow cytometry (FCM) analysis**
967 For FCM analysis, cells underwent blocking with 5% normal goat serum at 4°C for 1
968 hour, followed by incubation with corresponding primary antibodies: rabbit
969 anti-CD4-1 (1:200), rabbit anti-CD8α (1:200), and mouse anti-CD154 (1:200), at 4°C
970 for 2 hours. As a control, non-specific mouse or rabbit IgG served as an isotype
971 control. Subsequently, cells were washed and further incubated with secondary
972 antibodies: PE-conjugated goat anti-mouse IgG and FITC-conjugated goat anti-rabbit

973 IgG, for 1 hour at 4°C. Fluorescence signals were detected using a FACScan flow
974 cytometer (FACSCalibur, BD Biosciences) at 488 nm. FCM analysis was based on
975 forward/side scatter (FSC/SSC) characteristics and PE/FITC-conjugated fluorescence
976 with CellQuest program as previously described[65,78,79]. A minimum of 10,000 events
977 were collected from the lymphocyte gate. Data processing was executed using FlowJo
978 7.6 software (BD Biosciences). To examine $CD4^+$ and $CD8^+$ T cell proliferation,
979 zebrafish under PBS/inactivated SVCV treatment received intraperitoneal injections
980 of 5-ethynyl-2'-deoxyuridine, Alexa Fluor 488 (EdU, Beyotime, 8 μg/fish) twice
981 within a 24-hour interval two days before euthanization. Seven days after SVCV
982 stimulation, leukocytes from the kidney were collected and incubated with rabbit
983 anti-CD4/CD8 (1:500), followed by APC-conjugated rabbit anti-IgG secondary
984 antibody (1:1,000; Thermo Fisher). Subsequently, cells were fixed with 4%
985 paraformaldehyde, permeabilized with 0.3% Triton X-100 in PBS, and underwent
986 click reaction according to the manufacturer's instructions (BeyoClick EdU Cell
987 Proliferation Kit with Alexa Fluor 488, Beyotime). The proliferation of $CD4^+$ and
988 $CD8^+$ T cells was subsequently analyzed using FCM (FACSCalibur, BD
989 Biosciences)[80].
990
991 **Immunofluorescence staining**
992 For kidney staining, cryosections were prepared and fixed for 10 minutes in 95%
993 ethyl alcohol, followed by incubation with primary antibodies. Background
994 autofluorescence was eradicated by treating cryosections with 0.1 M glycine (pH 2.3)
995 for 10 minutes. After washing, kidney tissues were incubated with primary antibodies:
996 rabbit anti-CD4-1 (1:200), rabbit anti-CD8α (1:200), and mouse anti-IgM (1:200), at
997 4°C for 2 hours. A control was established using non-specific mouse or rabbit IgG as
998 an isotype control. Subsequently, cryosections were washed and further incubated
999 with secondary antibodies: APC-conjugated goat anti-rabbit/mouse IgG for 1 hour at
1000 4°C. The cryosections were then permeabilized using 0.3% Triton X-100 in PBS, and
1001 underwent click reaction according to the manufacturer's instructions (BeyoClick
1002 EdU Cell Proliferation Kit with Alexa Fluor 488, Beyotime). Prior to
1003 photomicrography, additional staining with 4',6-diamidino-2-phenylindole (DAPI,
1004 100 ng/ml; Sigma-Aldrich) was performed. Samples were captured utilizing a Laser
1005 Scanning Confocal Microscope (Olympus FV3000) with a 60 × oil-immersion
1006 objective lens[65,80].
1007
1008 **High-throughput IgM antibody repertoire analysis**
1009 cDNA samples extracted from the kidneys of three representative fish were subjected
1010 to individual amplification. This was achieved by utilizing specific forward primers
1011 corresponding to distinct subgroups of IGHV genes, combined with reverse primers

that are specific to the IGHM gene (Cμ)[81]. After the PCR reaction, the PCR product was mixed with 2 μl of loading buffer and loaded into a 1.0% agarose gel stained for visualization. Concurrently, 3 μl aliquots of all PCR products obtained from the same tissue were pooled together for subsequent RNaseq analysis. DNA concentrations were measured using the QuBit DNA quantification system (Invitrogen) and the quality checked using an Agilent 2100 Bioanalyzer (Agilent Technologies). A library was constructed per individual tissues with the TruSeq DNA PCR-Free Library Prep Kit (Illumina) according to the manufacturer's instructions. Libraries were pooled together and paired-end sequencing was performed on an Illumina MiSeq with a MiSeq Reagent Kit v3 (2 × 300 cycles) cartridge (Illumina). The primers are listed in **Supplementary file 7**.

Statistical analysis

Statistical analysis and graphical presentation were performed with GraphPad Prism and Origin Pro. All data were presented as the mean ± standard deviation (SD) of each group. Statistical evaluation of differences was assessed using one-way ANOVA, followed by an unpaired two-tailed t-test. Statistical significance was defined as $^{*}p < 0.05$, $^{**}p < 0.01$, $^{***}p < 0.001$. All experiments were replicated at least three times.

Acknowledgements

This work was supported by grants from the National Natural Science Foundation of China, and the National Key Research and Development Program of China.

Additional information

Funding

Funder	Grant reference number	Author
National Natural Science Foundation of China	32173003	Lixin Xiang
National Natural Science Foundation of China	31630083	Jianzhong Shao
National Key Research and Development Program of China	2018YFD0900503	Jianzhong Shao
National Key Research and Development Program of China	2018YFD0900505	Lixin Xiang

The funders had no role in study design, data collection and interpretation, or the decision to submit the work for publication.

Author contributions

Chongbin Hu, Formal analysis, Investigation, Methodology, Software, Supervision, Validation, Visualization, Writing – original draft, Writing – review and editing; Nan Zhang, Formal analysis, Investigation, Methodology, Visualization, Writing – review and editing; Yun Hong, Formal analysis, Investigation, Methodology, Writing – review and editing; Ruxiu Tie, Provided consultation, reviewed and revised the manuscript; Dongdong Fan, Provided material support; Aifu Lin, Provided consultation, reviewed and revised the manuscript; Ye Chen, Methodology, Supervision, Provided consultation, reviewed and revised the manuscript; Lixin Xiang, Funding acquisition, Supervision, Writing – review and editing; Jianzhong Shao, Conceptualization, Data curation, Formal analysis, Funding acquisition, Investigation, Methodology, Project administration, Supervision, Visualization, Writing – original draft, Writing – review and editing

Author ORCIDs

Ye Chen: https://orcid.org/0000-0003-3671-2504
Lixin Xiang: https://orcid.org/0000-0002-7136-7729
Jianzhong Shao: https://orcid.org/0000-0003-3483-1817

Ethics

All animal care and experimental procedures were approved by the Committee on Animal Care and Use and the Committee on the Ethics of Animal Experiments of Zhejiang University (ZU_0325/2021; Hangzhou, China).

Conflict of interest

The authors declare that no competing interests exist.

Supplementary files

Supplementary file 1. Markergene list and gene expression tables of 13 immune-cell and renal cell categories.
Supplementary file 2. Markergene list and gene expression tables of HSPC subsets.
Supplementary file 3. Markergene list and gene expression tables of T/NK cell subsets.
Supplementary file 4. Markergene list and gene expression tables of B cell subsets.
Supplementary file 5. Markergene list and gene expression tables of macrophages/myeloid cell subsets.
Supplementary file 6. Markergene list and gene expression tables of neutrophil subsets.
Supplementary file 7. Primers used in this study for Real-time quantitative PCR and

IgM antibody repertoire analysis.

Data availability

The data that support the findings of this study are openly available in GEO at https://www.ncbi.nlm.nih.gov/geo/, GEO accession number GSE242133.

The following dataset was generated:

Author(s)	Year	Dataset title	Dataset URL	Database and Identifier
Chongbin Hu	2023	Single-cell RNA sequencing unveils the hidden powers of zebrafish kidney for generating both hematopoiesis and adaptive antiviral immunity	https://www.ncbi.nlm.nih.gov/geo/query/acc.cgi?acc=GSE242133	NCBI Gene Expression Omnibus, GSE242133

References

1 Sunyer, J. O. Fishing for mammalian paradigms in the teleost immune system. *Nature immunology*. 2013;14: 320-326.

2 Zhu, L.-y., Nie, L., Zhu, G., Xiang, L.-x. & Shao, J.-z. Advances in research of fish immune-relevant genes: a comparative overview of innate and adaptive immunity in teleosts. *Developmental & Comparative Immunology*. 2013;39: 39-62.

3 Volff, J. Genome evolution and biodiversity in teleost fish. *Heredity*. 2005;94: 280-294.

4 Fan, G., Song, Y., Yang, L. *et al.* Initial data release and announcement of the 10,000 Fish Genomes Project (Fish10K). *GigaScience*. 2020;9: giaa080.

5 Rauta, P. R., Nayak, B. & Das, S. Immune system and immune responses in fish and their role in comparative immunity study: a model for higher organisms. *Immunology letters*. 2012;148: 23-33.

6 Secombes, C. & Wang, T. in *Infectious disease in aquaculture* 3-68 (Elsevier, 2012).

7 Mokhtar, D. M., Zaccone, G., Alesci, A. *et al.* Main components of fish immunity: An overview of the fish immune system. *Fishes*. 2023;8: 93.

8 Smith, N. C., Rise, M. L. & Christian, S. L. A comparison of the innate and adaptive immune systems in cartilaginous fish, ray-finned fish, and lobe-finned fish. *Frontiers in immunology*. 2019;10: 2292.

9 Cooper, M. D. & Alder, M. N. The evolution of adaptive immune systems. *Cell*. 2006;124: 815-822.

10 Wan, F., Hu, C.-b., Ma, J.-x. *et al.* Characterization of γδ T cells from zebrafish provides insights into their important role in adaptive humoral immunity. *Frontiers in immunology*. 2017;7: 675.

11 Neely, H. R. & Flajnik, M. F. Emergence and evolution of secondary lymphoid organs. *Annual review of cell and developmental biology*. 2016;32: 693-711.

12 Matz, H., Taylor, R. S., Redmond, A. K. *et al.* Organized B cell sites in cartilaginous fishes reveal the evolutionary foundation of germinal centers. *Cell Reports*. 2023;42.

1114 13 Barreto, V. M., Pan-Hammarstrom, Q., Zhao, Y. *et al.* AID from bony fish catalyzes
1115 class switch recombination. *The Journal of experimental medicine*. 2005;202:
1116 733-738.
1117 14 Wakae, K., Magor, B. G., Saunders, H. *et al.* Evolution of class switch recombination
1118 function in fish activation-induced cytidine deaminase, AID. *International*
1119 *immunology*. 2006;18: 41-47.
1120 15 Hu, C. B., Wang, J., Hong, Y. *et al.* Single-cell transcriptome profiling reveals diverse
1121 immune cell populations and their responses to viral infection in the spleen of
1122 zebrafish. *The FASEB Journal*. 2023;37: e22951.
1123 16 Ferrero, G., Gomez, E., Lyer, S. *et al.* The macrophage-expressed gene (mpeg) 1
1124 identifies a subpopulation of B cells in the adult zebrafish. *Journal of leukocyte*
1125 *biology*. 2020;107: 431-443.
1126 17 Rubin, S. A., Baron, C. S., Pessoa Rodrigues, C. *et al.* Single-cell analyses reveal
1127 early thymic progenitors and pre-B cells in zebrafish. *Journal of Experimental*
1128 *Medicine*. 2022;219: e20220038.
1129 18 Philipson, B. I., O'Connor, R. S., May, M. J. *et al.* 4-1BB costimulation promotes
1130 CAR T cell survival through noncanonical NF-κB signaling. *Science signaling*.
1131 2020;13.
1132 19 van Asten, S. D., de Groot, R., van Loenen, M. M. *et al.* T cells expanded from renal
1133 cell carcinoma display tumor-specific CD137 expression but lack significant IFN-γ,
1134 TNF-α or IL-2 production. *OncoImmunology*. 2021;10: 1860482.
1135 20 Ribeil, J.-A., Zermati, Y., Vandekerckhove, J. *et al.* Hsp70 regulates erythropoiesis by
1136 preventing caspase-3-mediated cleavage of GATA-1. *Nature*. 2007;445: 102-105.
1137 21 Tang, Q., Iyer, S., Lobbardi, R. *et al.* Dissecting hematopoietic and renal cell
1138 heterogeneity in adult zebrafish at single-cell resolution using RNA sequencing.
1139 *Journal of Experimental Medicine*. 2017;214: 2875-2887.
1140 22 Asahara, T., Murohara, T., Sullivan, A. *et al.* Isolation of putative progenitor
1141 endothelial cells for angiogenesis. *Science*. 1997;275: 964-966.
1142 23 Shi, Q., Rafii, S., Wu, M. H.-D. *et al.* Evidence for circulating bone marrow-derived
1143 endothelial cells. *Blood, The Journal of the American Society of Hematology*. 1998;92:
1144 362-367.
1145 24 Fu, B., Wang, F., Sun, R. *et al.* CD11b and CD27 reflect distinct population and
1146 functional specialization in human natural killer cells. *Immunology*. 2011;133:
1147 350-359.
1148 25 Ahmed, R., Omidian, Z., Giwa, A. *et al.* A public BCR present in a unique
1149 dual-receptor-expressing lymphocyte from type 1 diabetes patients encodes a potent T
1150 cell autoantigen. *Cell*. 2019;177: 1583-1599. e1516.
1151 26 Zwollo, P., Cole, S., Bromage, E. & Kaattari, S. B cell heterogeneity in the teleost
1152 kidney: evidence for a maturation gradient from anterior to posterior kidney. *The*
1153 *Journal of Immunology*. 2005;174: 6608-6616.
1154 27 Bromage, E. S., Kaattari, I. M., Zwollo, P. & Kaattari, S. L. Plasmablast and plasma
1155 cell production and distribution in trout immune tissues. *The Journal of Immunology*.
1156 2004;173: 7317-7323.
1157 28 Zhu, L.-y., Lin, A.-f., Shao, T. *et al.* B cells in teleost fish act as pivotal initiating

1158 APCs in priming adaptive immunity: an evolutionary perspective on the origin of the
1159 B-1 cell subset and B7 molecules. *The Journal of Immunology*. 2014;192: 2699-2714.
1160 29 Wu, L., Gao, A., Li, L. *et al.* A single-cell transcriptome profiling of anterior kidney
1161 leukocytes from Nile tilapia (Oreochromis niloticus). *Frontiers in Immunology*. 2021:
1162 5399.
1163 30 Zhou, Q., Zhao, C., Yang, Z. *et al.* Cross-organ single-cell transcriptome profiling
1164 reveals macrophage and dendritic cell heterogeneity in zebrafish. *Cell Reports*.
1165 2023;42.
1166 31 Huang, H., Hao, S., Li, F. *et al.* CD4+ Th1 cells promote CD8+ Tc1 cell survival,
1167 memory response, tumor localization and therapy by targeted delivery of interleukin 2
1168 via acquired pMHC I complexes. *Immunology*. 2007;120: 148-159.
1169 32 Ahrends, T., Spanjaard, A., Pilzecker, B. *et al.* CD4+ T cell help confers a cytotoxic T
1170 cell effector program including coinhibitory receptor downregulation and increased
1171 tissue invasiveness. *Immunity*. 2017;47: 848-861. e845.
1172 33 Aggad, D., Mazel, M., Boudinot, P. *et al.* The two groups of zebrafish virus-induced
1173 interferons signal via distinct receptors with specific and shared chains. *The Journal*
1174 *of Immunology*. 2009;183: 3924-3931.
1175 34 Sullivan, C., Soos, B.-L., Millard, P. J., Kim, C. H. & King, B. L. Modeling
1176 Virus-Induced Inflammation in Zebrafish: A Balance Between Infection Control and
1177 Excessive Inflammation. *Frontiers in Immunology*. 2021;12: 1635.
1178 35 Langevin, C., Aleksejeva, E., Passoni, G. *et al.* The antiviral innate immune response
1179 in fish: evolution and conservation of the IFN system. *Journal of molecular biology*.
1180 2013;425: 4904-4920.
1181 36 Gan, Z., Chen, S. N., Huang, B., Zou, J. & Nie, P. Fish type I and type II interferons:
1182 composition, receptor usage, production and function. *Reviews in Aquaculture*.
1183 2020;12: 773-804.
1184 37 Perng, Y.-C. & Lenschow, D. J. ISG15 in antiviral immunity and beyond. *Nature*
1185 *Reviews Microbiology*. 2018;16: 423-439.
1186 38 Langevin, C., Van Der Aa, L., Houel, A. *et al.* Zebrafish ISG15 exerts a strong
1187 antiviral activity against RNA and DNA viruses and regulates the interferon response.
1188 *Journal of virology*. 2013;87: 10025-10036.
1189 39 Mitroulis, I., Ruppova, K., Wang, B. *et al.* Modulation of myelopoiesis progenitors is
1190 an integral component of trained immunity. *Cell*. 2018;172: 147-161. e112.
1191 40 Netea, M., Joosten, L., Latz, E. *et al.* (2016).
1192 41 Yao, Y., Jeyanathan, M., Haddadi, S. *et al.* Induction of autonomous memory alveolar
1193 macrophages requires T cell help and is critical to trained immunity. *Cell*. 2018;175:
1194 1634-1650. e1617.
1195 42 de Laval, B., Maurizio, J., Kandalla, P. K. *et al.* C/EBPβ-dependent epigenetic
1196 memory induces trained immunity in hematopoietic stem cells. *Cell stem cell*.
1197 2020;26: 657-674. e658.
1198 43 Kaufmann, E., Sanz, J., Dunn, J. L. *et al.* BCG educates hematopoietic stem cells to
1199 generate protective innate immunity against tuberculosis. *Cell*. 2018;172: 176-190.
1200 e119.
1201 44 Riedel, C., Hennrich, A. A. & Conzelmann, K.-K. Components and architecture of the

1202 rhabdovirus ribonucleoprotein complex. *Viruses*. 2020;12: 959.
1203 45 Kiuchi, A. & Roy, P. Comparison of the primary sequence of spring viremia of carp
1204 virus M protein with that of vesicular stomatitis virus. *Virology*. 1984;134: 238-243.
1205 46 Roy, P. Phosphoproteins of spring viremia of carp virus. *Virology*. 1981;112: 274-281.
1206 47 Boehm, T. & Bleul, C. C. The evolutionary history of lymphoid organs. *Nature*
1207 *immunology*. 2007;8: 131-135.
1208 48 Chinn, I. K., Blackburn, C. C., Manley, N. R. & Sempowski, G. D. in *Seminars in*
1209 *immunology.* 309-320 (Elsevier).
1210 49 Malhotra, D., Fletcher, A. L. & Turley, S. J. Stromal and hematopoietic cells in
1211 secondary lymphoid organs: partners in immunity. *Immunological reviews*. 2013;251:
1212 160-176.
1213 50 Randall, T. D., Carragher, D. M. & Rangel-Moreno, J. Development of secondary
1214 lymphoid organs. *Annu. Rev. Immunol.* 2008;26: 627-650.
1215 51 Stachura, D. L., Reyes, J. R., Bartunek, P. *et al.* Zebrafish kidney stromal cell lines
1216 support multilineage hematopoiesis. *Blood, The Journal of the American Society of*
1217 *Hematology*. 2009;114: 279-289.
1218 52 Diep, C. Q., Ma, D., Deo, R. C. *et al.* Identification of adult nephron progenitors
1219 capable of kidney regeneration in zebrafish. *Nature*. 2011;470: 95-100.
1220 53 Page, D. M., Wittamer, V., Bertrand, J. Y. *et al.* An evolutionarily conserved program
1221 of B-cell development and activation in zebrafish. *Blood, The Journal of the*
1222 *American Society of Hematology*. 2013;122: e1-e11.
1223 54 Catton, W. Blood cell formation in certain teleost fishes. *Blood*. 1951;6: 39-60.
1224 55 Zapata, A. Ultrastructural study of the teleost fish kidney. *Developmental &*
1225 *Comparative Immunology*. 1979;3: 55-65.
1226 56 Yang, L., Bryder, D., Adolfsson, J. r. *et al.* Identification of Lin–Sca1+ kit+ CD34+
1227 Flt3–short-term hematopoietic stem cells capable of rapidly reconstituting and
1228 rescuing myeloablated transplant recipients. *Blood*. 2005;105: 2717-2723.
1229 57 Shin, J. Y., Hu, W., Naramura, M. & Park, C. Y. High c-Kit expression identifies
1230 hematopoietic stem cells with impaired self-renewal and megakaryocytic bias.
1231 *Journal of Experimental Medicine*. 2014;211: 217-231.
1232 58 Woolthuis, C. M. & Park, C. Y. Hematopoietic stem/progenitor cell commitment to
1233 the megakaryocyte lineage. *Blood, The Journal of the American Society of*
1234 *Hematology*. 2016;127: 1242-1248.
1235 59 Kondo, M. Lymphoid and myeloid lineage commitment in multipotent hematopoietic
1236 progenitors. *Immunological reviews*. 2010;238: 37-46.
1237 60 Sumbria, D., Berber, E., Mathayan, M. & Rouse, B. T. Virus infections and host
1238 metabolism—can we manage the interactions? *Frontiers in Immunology*. 2021;11:
1239 594963.
1240 61 Rouse, B. T. & Sehrawat, S. Immunity and immunopathology to viruses: what
1241 decides the outcome? *Nature Reviews Immunology*. 2010;10: 514-526.
1242 62 Perelson, A. S. & Ribeiro, R. M. Introduction to modeling viral infections and
1243 immunity. *Immunological reviews*. 2018;285: 5.
1244 63 Spellberg, B. & Edwards Jr, J. E. Type 1/Type 2 immunity in infectious diseases.
1245 *Clinical Infectious Diseases*. 2001;32: 76-102.

1246 64 García-Valtanen, P., Martínez-López, A., López-Muñoz, A. *et al.* Zebra fish lacking
1247 adaptive immunity acquire an antiviral alert state characterized by upregulated gene
1248 expression of apoptosis, multigene families, and interferon-related genes. *Frontiers in*
1249 *immunology*. 2017;8: 121.
1250 65 Feng, W., Chong-Bin, H., Jun-Xia, M. *et al.* Characterization of γδ T Cells from
1251 Zebrafish Provides Insights into Their Important Role in Adaptive Humoral Immunity.
1252 *Frontiers in Immunology*. 2016;7.
1253 66 Li, J. Y., Wang, Y. Y., Shao, T., Fan, D. D. & Shao, J. Z. The zebrafish NLRP3
1254 inflammasome has functional roles in ASC-dependent interleukin-1β maturation and
1255 gasdermin E–mediated pyroptosis. *Journal of Biological Chemistry*. 2019;295:
1256 jbc.RA119.011751.
1257 67 Chen, Z. Y., Liu, H., Li, Z. Q. & Zhang, Q. Y. Development and characterization of
1258 monoclonal antibodies to spring viraemia of carp virus. *Vet Immunol Immunopathol*.
1259 2008;123: 266-276.
1260 68 Reed, L. J. & Muench, H. A simple method of estimating fifty per cent endpoints.
1261 *American journal of epidemiology*. 1938;27: 493-497.
1262 69 Dong, C., Xiong, X., Luo, Y. *et al.* Efficacy of a formalin-killed cell vaccine against
1263 infectious spleen and kidney necrosis virus (ISKNV) and immunoproteomic analysis
1264 of its major immunogenic proteins. *Vet Microbiol*. 2013;162: 419-428.
1265 70 Tong, S., Wei, S., Jia-Yu, Z. *et al.* Costimulatory Function of Cd58/Cd2 Interaction in
1266 Adaptive Humoral Immunity in a Zebrafish Model. *Frontiers in Immunology*. 2018;9:
1267 1204-.
1268 71 Hernandez, P. P., Strzelecka, P. M., Athanasiadis, E. I. *et al.* Single-cell transcriptional
1269 analysis reveals ILC-like cells in zebrafish. *Sci Immunol*. 2018;3.
1270 72 McGinnis, C. S., Murrow, L. M. & Gartner, Z. J. DoubletFinder: doublet detection in
1271 single-cell RNA sequencing data using artificial nearest neighbors. *Cell systems*.
1272 2019;8: 329-337. e324.
1273 73 Butler, A., Hoffman, P., Smibert, P., Papalexi, E. & Satija, R. Integrating single-cell
1274 transcriptomic data across different conditions, technologies, and species. *Nat*
1275 *Biotechnol*. 2018;36: 411-420.
1276 74 Xu, Z., You, W., Chen, W. *et al.* Single-cell RNA sequencing and lipidomics reveal
1277 cell and lipid dynamics of fat infiltration in skeletal muscle. *J Cachexia Sarcopenia*
1278 *Muscle*. 2021;12: 109-129.
1279 75 La Manno, G., Soldatov, R., Zeisel, A. *et al.* RNA velocity of single cells. *Nature*.
1280 2018;560: 494-498.
1281 76 Robinson, J. T., Thorvaldsdóttir, H., Winckler, W. *et al.* Integrative genomics viewer.
1282 *Nature biotechnology*. 2011;29: 24-26.
1283 77 Speranza, E., Williamson, B. N., Feldmann, F. *et al.* Single-cell RNA sequencing
1284 reveals SARS-CoV-2 infection dynamics in lungs of African green monkeys. *Science*
1285 *Translational Medicine*. 2021;13.
1286 78 Shi, W., Shao, T., Li, J. Y. *et al.* BTLA-HVEM Checkpoint Axis Regulates Hepatic
1287 Homeostasis and Inflammation in a ConA-Induced Hepatitis Model in Zebrafish.
1288 *Journal of immunology*. 2019;203: 2425-2442.
1289 79 Shao, T., Shi, W., Zheng, J. Y. *et al.* Costimulatory Function of Cd58/Cd2 Interaction

in Adaptive Humoral Immunity in a Zebrafish Model. *Front Immunol*. 2018;9: 1204.

80 Hong, Y., Hu, C.-b., Bai, J. *et al.* Essential role of an ERV-derived Env38 protein in adaptive humoral immunity against an exogenous SVCV infection in a zebrafish model. *PLoS Pathogens*. 2023;19: e1011222.

81 Weinstein, J. A., Jiang, N., White III, R. A., Fisher, D. S. & Quake, S. R. High-throughput sequencing of the zebrafish antibody repertoire. *Science*. 2009;324: 807-810.

1329 **Figure legends**

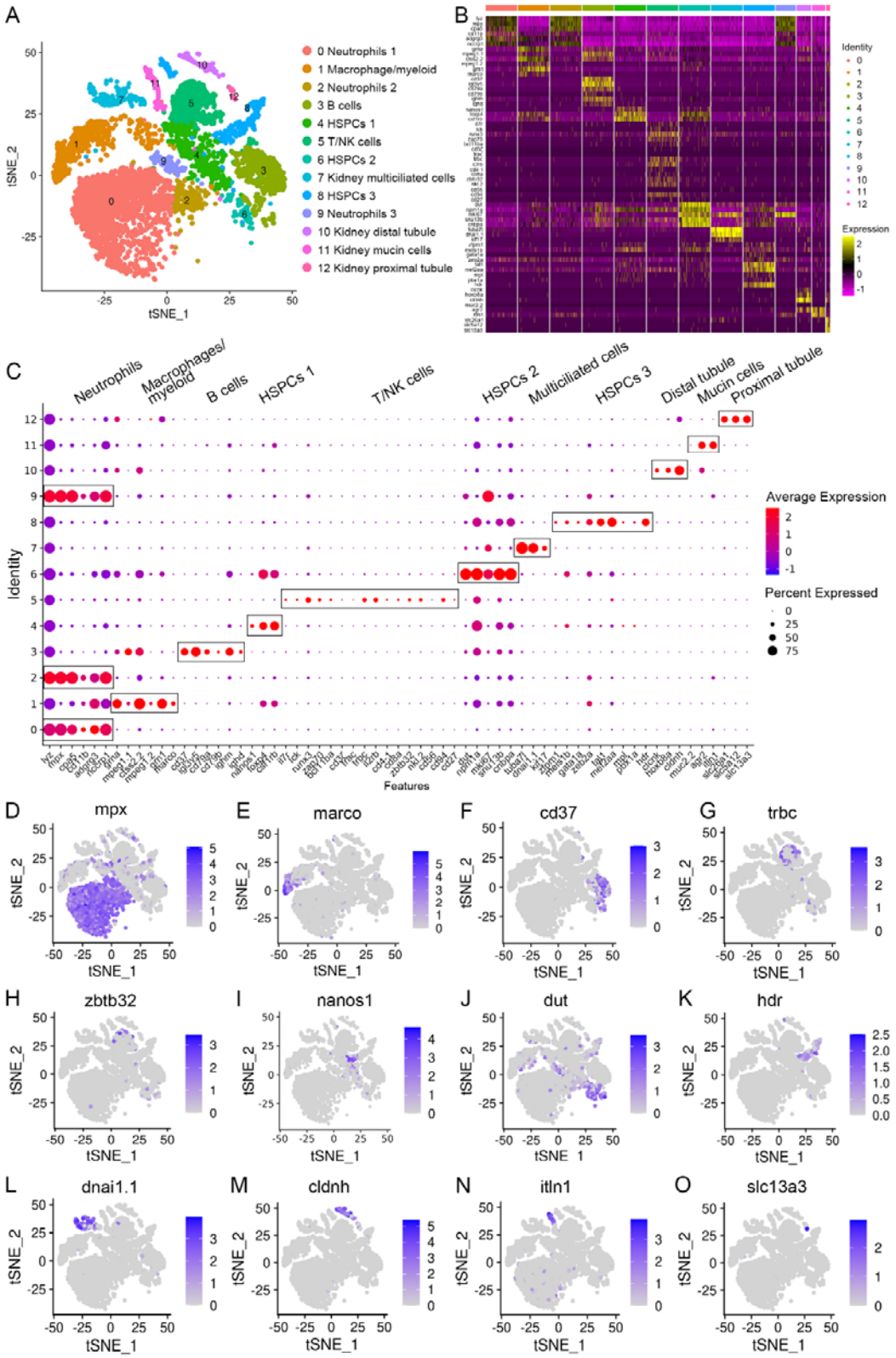

1330

1331 **Figure 1.** Categorization of the HSPCs and immune cell types in zebrafish kidney. (**A**)

1332 Nonlinear t-SNE clustering visually categorized populations of zebrafish kidney

leukocytes. PCA was performed following expression data normalization, with subsequent PCA dimension reduction to streamline variables. The cell clustering algorithm based on graph theory was then employed. (**B**) Heatmap displaying marker genes specific to each cluster. Columns depict distinct cell subtypes, while rows correspond to genes. Expression levels are color-coded, with intense yellow indicating high expression and deep purple representing low expression. (**C**) Dot plots illustrating marker gene expression levels and the respective percentages of cluster-expressing cells. (**D–O**) t-SNE results depicting molecular marker distribution for immune and kidney cell types. Each dot signifies a cell, with dark dots indicating elevated expression of the marker gene in a given cell. Notably, Neutrophil marker gene in (**D**), Macrophage/myeloid cells marker gene in (**E**), B-cells marker gene in (**F**), T-cells marker gene in (**G**), NK-cells marker gene in (**H**), HSPCs 1 marker gene in (**I**), HSPCs 2 marker gene in (**J**), HSPCs 3 marker gene in (**K**), kidney multiciliated cells marker gene in (**L**), kidney distal tubule cells marker gene in (**M**), kidney mucin cells marker gene in (**N**), and kidney proximal tubule cells marker genes in (**O**).

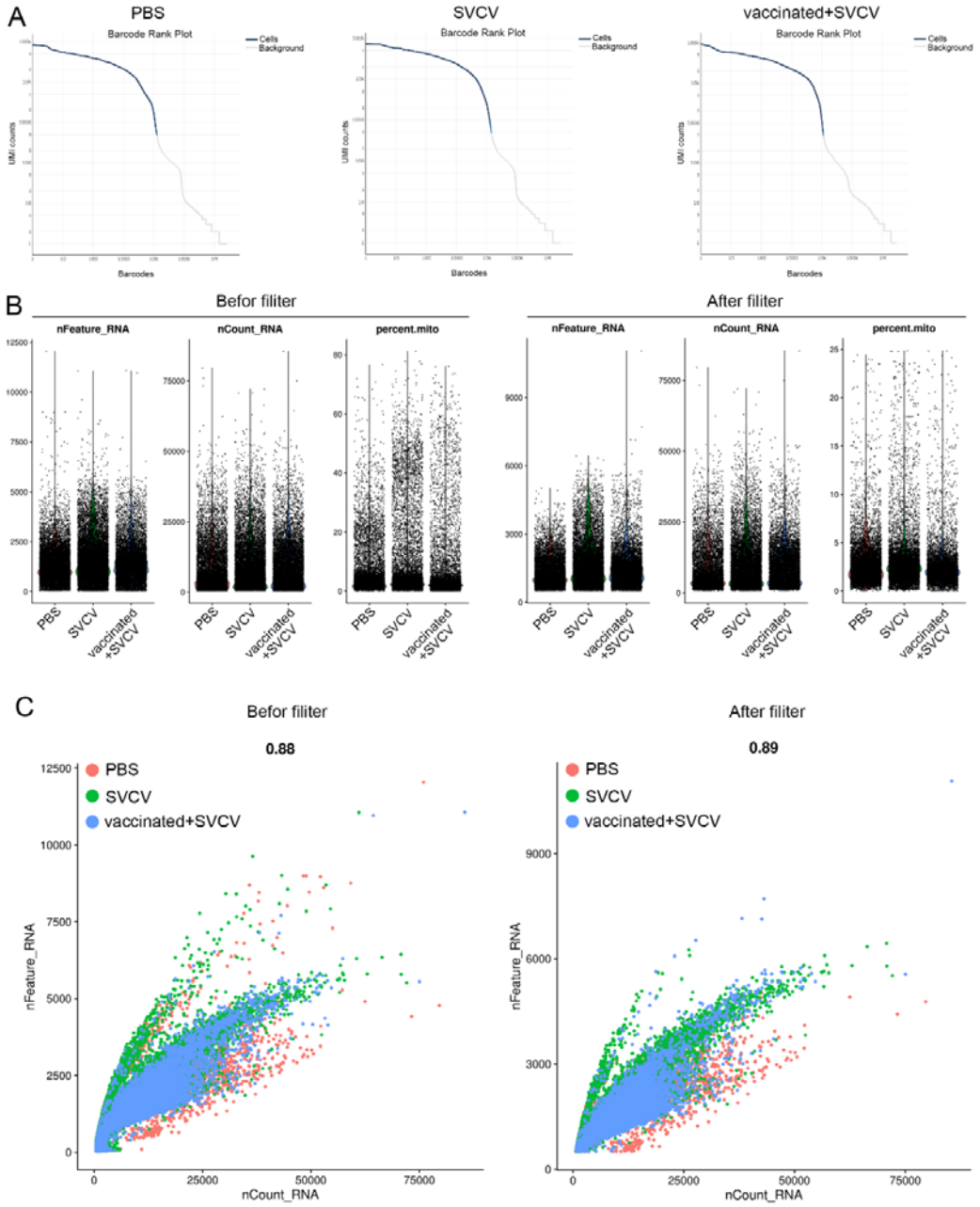

Figure 1-figure supplement 1. Single-cell sequencing quality control. (**A**) Identification of the effective cell number of the sample. The X_axis is the number of barcodes, and the Y_axis is the UMI counts. Blue line is the effective cells corresponding to barcodes, and the gray line is the background noise. (**B**) The basic information of sample cell before and after filtering, including the total number of genes (nFeature_RNA), the total number of UMIs (nCount_RNA) and the percentage of reads mapping mitochondrial genes (Percent.mito). (**C**) The scatter plot of sample cell basic information before and after filtering, showing the relationship between nCount_RNA and nFeature_RNA. The numbers above the graph are Pearson correlation coefficients.

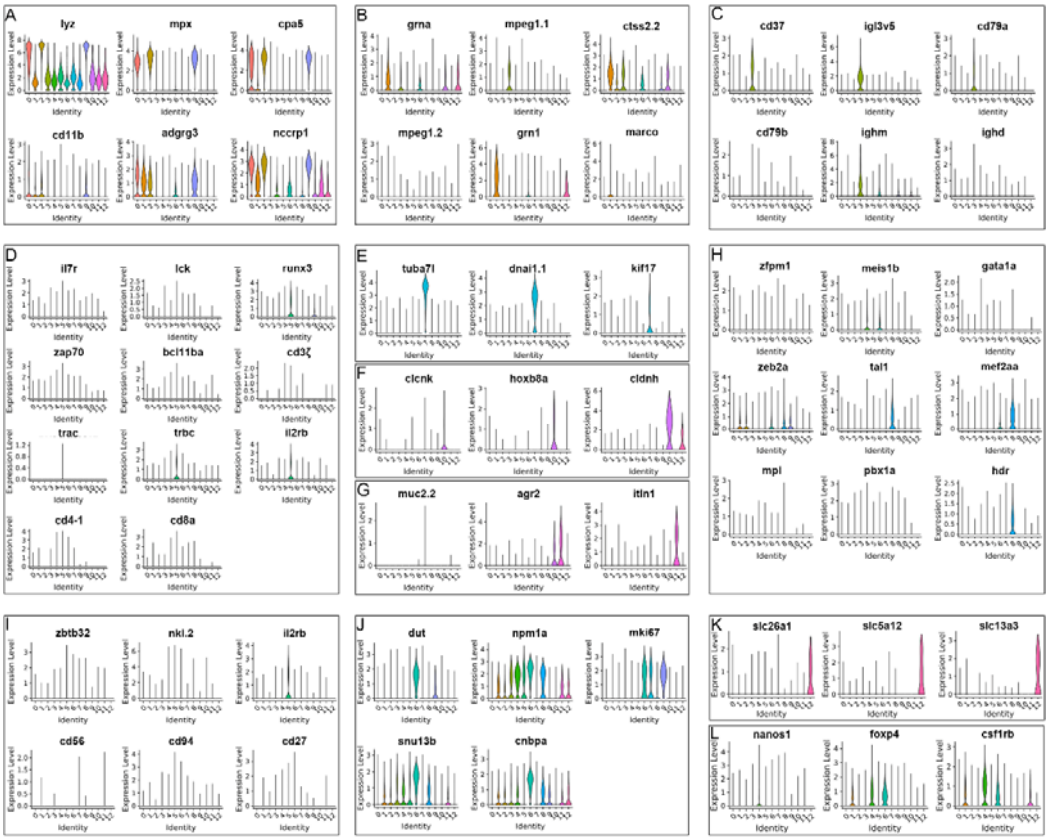

Figure 1-figure supplement 2. Violin plots showing the expression of marker genes for per immune cell and renal cell categories at the single cell level. (**A**) neutrophil; (**B**) macrophage/myeloid cells; (**C**) B cells; (**D**) T cells; (**E**) Kidney multiciliated cells; (**F**) Kidney distal tubule cells; (**G**) Kidney mucin cells; (**H**) HSPCs 3; (**I**) NK cells; (**J**) HSPCs 2; (**K**) Kidney proximal tubule cells; (**L**) HSPCs 1.

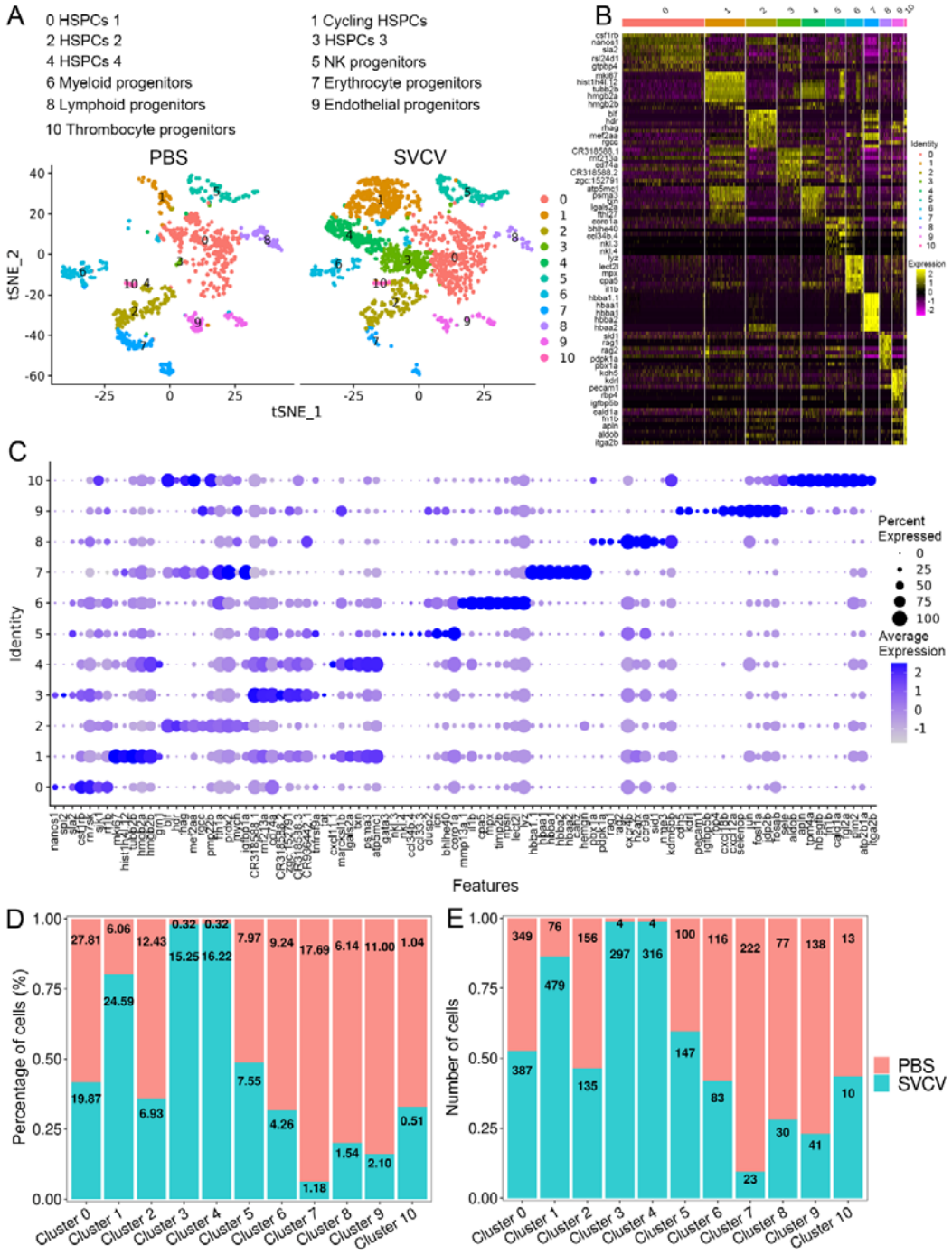

Figure 2. HSPCs subtype analysis based on single-cell gene expression. (**A**) Graph-based clustering revealed 11 subclusters of HSPCs within both the control group (PBS) and SVCV-infected group. (**B**) Heatmap presenting marker gene expression for each HSPC subcluster. (**C**) Dot plots of differentially expressed selected markers across HSPCs subtypes. Dot size indicates the percentage of cells within a population expressing a specific marker, while dot color indicates average expression. (**D**) Histogram demonstrating differences in HSPC subset ratios between

the control group (PBS) and SVCV-infected group. (**E**) Histogram illustrating discrepancies in HSPC numbers across clusters between the control group and the SVCV-infected group.

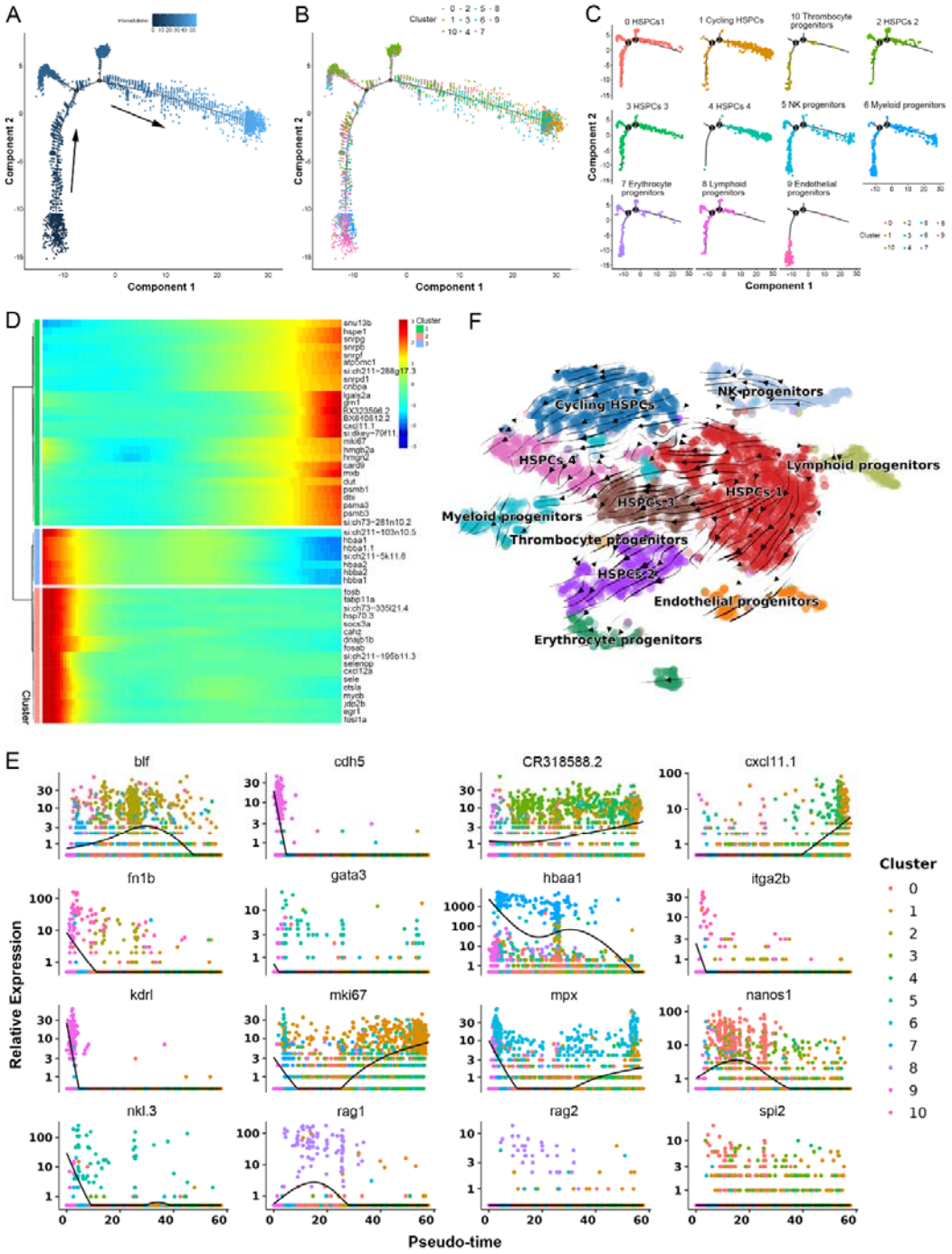

Figure 3. Pseudotemporal and RNA velocity analyses of zebrafish kidney HSPCs development. (**A**) Pseudotime single-cell trajectory of HSPCs reconstructed using Monocle2. Pseudotime is represented in a gradient from dark to light blue, with its starting point indicated. (**B-C**) Distribution of the 11 HSPC subsets within the trajectory. (**D**) Pseudotemporal heatmap demonstrating gene expression dynamics of significant marker genes. Genes (rows) were grouped into three modules, while cells (columns) were ordered according to pseudotime. (**E**) Gene expression dynamics over

1392 pseudotime computed in Monocle2, color-coded by cluster assignment for 16 genes
1393 linked to HSPCs development. (**F**) Single cell velocities of the HSPCs subclusters
1394 visualized as streamlines in a t-SNE plot. Black arrows indicate direction and
1395 thickness indicates speed along the HSPCs development trajectory.
1396

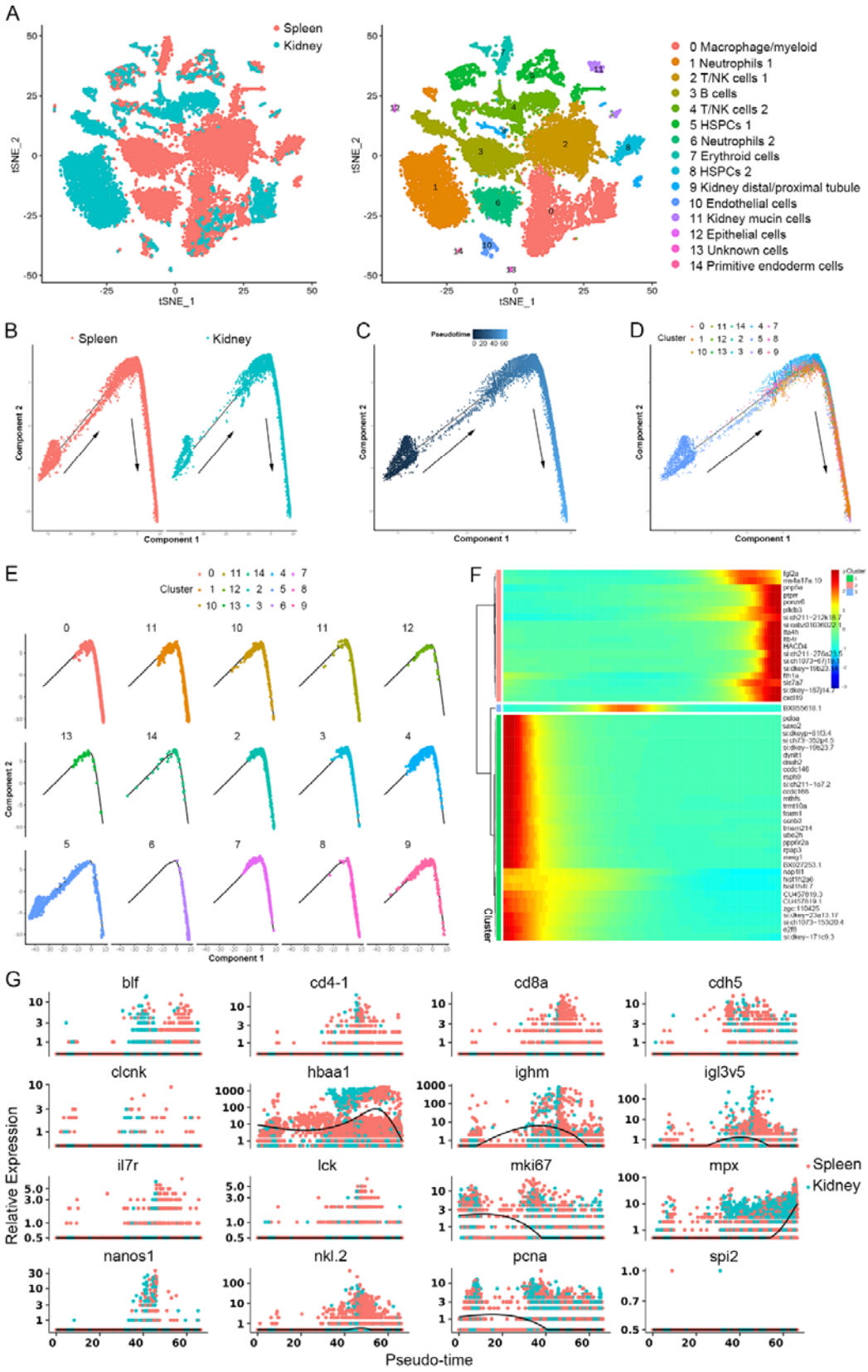

Figure 4. Integrated clustering and pseudotemporal analysis of zebrafish kidney and

spleen HSPCs and immune cells development. (**A**) Nonlinear t-SNE clustering illustrated the divergence in classification outcomes of zebrafish leukocyte populations between kidney and spleen. (**B**) Pseudotime single-cell trajectory of zebrafish kidney marrow and spleen immune cells reconstructed using Monocle2. (**C**) Pseudotime single-cell trajectories of HSPCs and immune cells, with pseudotime depicted in a gradient from dark to light blue, marking its inception. (**D-E**) Distribution of subsets within the trajectory. (**F**) Pseudotemporal heatmap revealing gene expression dynamics of significant marker genes. Genes (rows) were organized into three modules, while cells (columns) followed pseudotime order. (**G**) Gene expression dynamics over pseudotime computed in Monocle2, colored by cluster assignment for 16 genes associated with immune cell development.

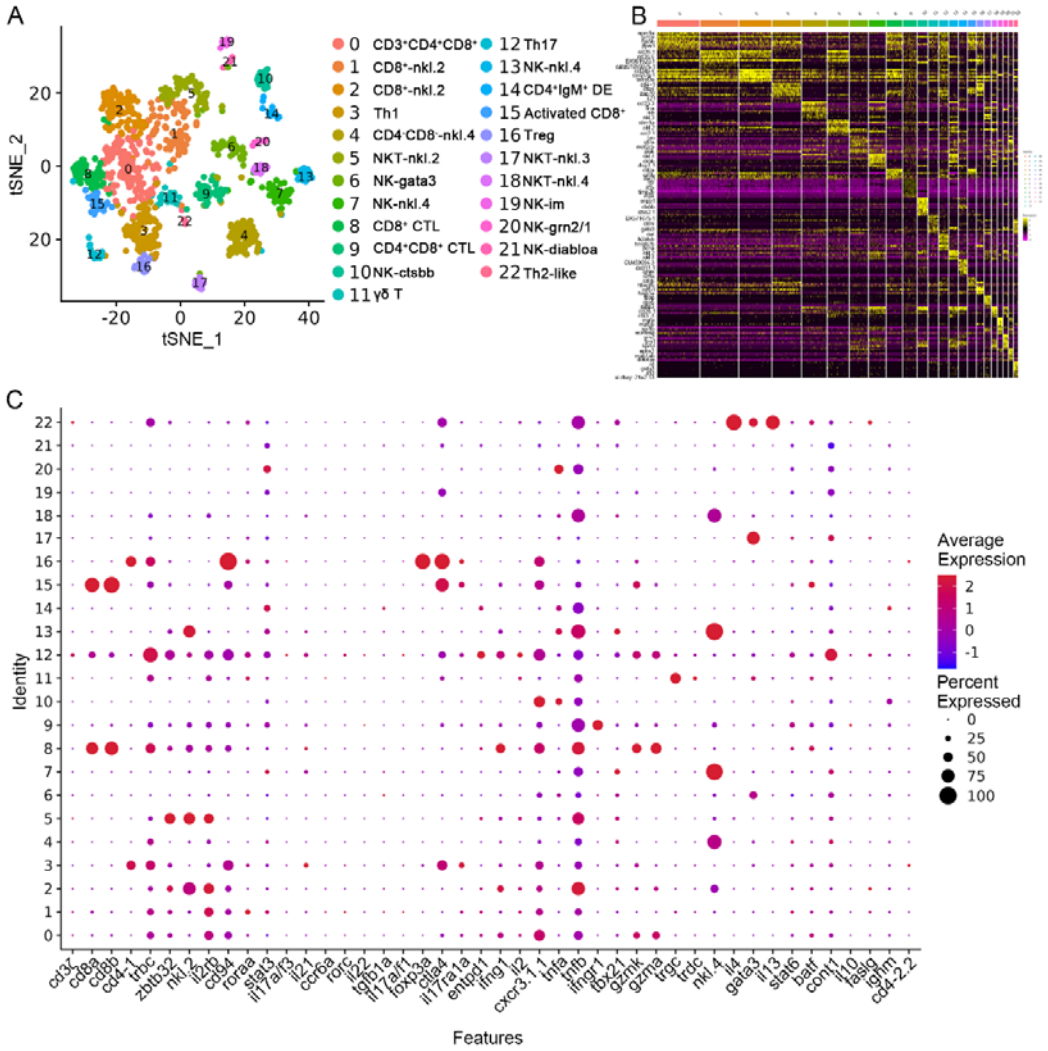

Figure 5. T/NK cell subtype analysis based on single-cell gene expression. (**A**) Graph-based clustering unveiled 23 T/NK cell subclusters within the control group. Nonlinear t-SNE clustering highlighted the differing classification outcomes of T/NK cell populations in zebrafish kidney. (**B**) Heatmap showcasing marker gene expression for each cluster. Columns represent cell subtypes, while rows depict genes, color-coded according to expression levels. (**C**) Dot plots demonstrating marker gene expression levels and the respective percentages of cells per cluster expressing the gene of interest.

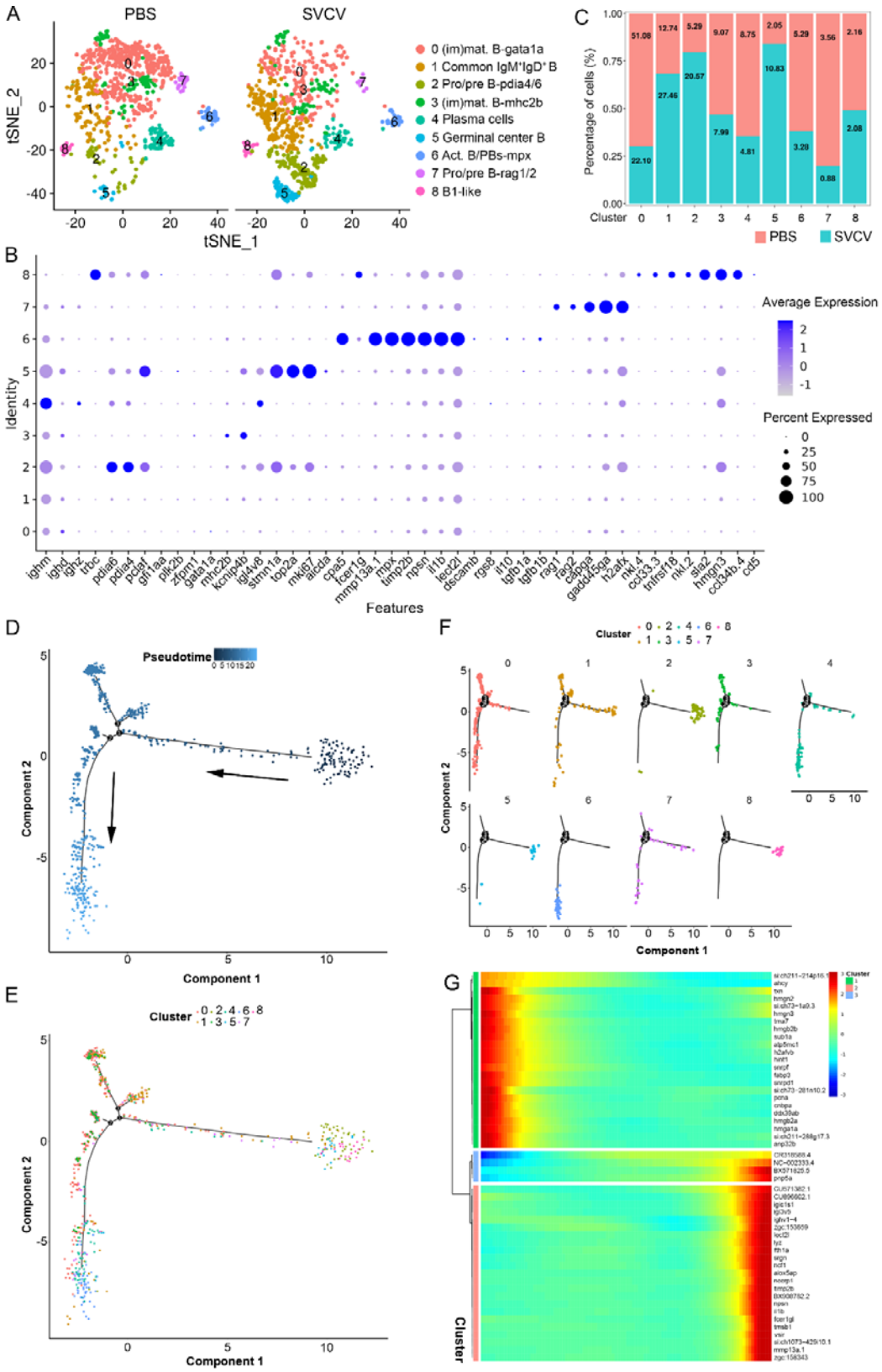

Figure 6. B-cell subtype and pseudotemporal analysis based on single-cell gene expression. (**A**) Graph-based clustering disclosed nine B cell subclusters in both the

control group (PBS) and SVCV-infected group. (**B**) Dot plots of differentially expressed selected markers across B cell subtypes. Dot size indicates the percentage of cells within a population expressing a specific marker, while dot color indicates average expression. (**C**) Histogram highlighting differences in cell ratios between the control group and the SVCV-infected group. (**D**) Pseudotime single-cell trajectory of B cells reconstructed using Monocle2, pseudotime shown in a gradient from dark to light blue, marking its starting point. (**E-F**) Distribution of the nine B cell subsets within the trajectory. (**G**) Pseudotemporal heatmap revealing gene expression dynamics of significant marker genes. Genes (rows) were grouped into three modules, while cells (columns) were ordered based on pseudotime.

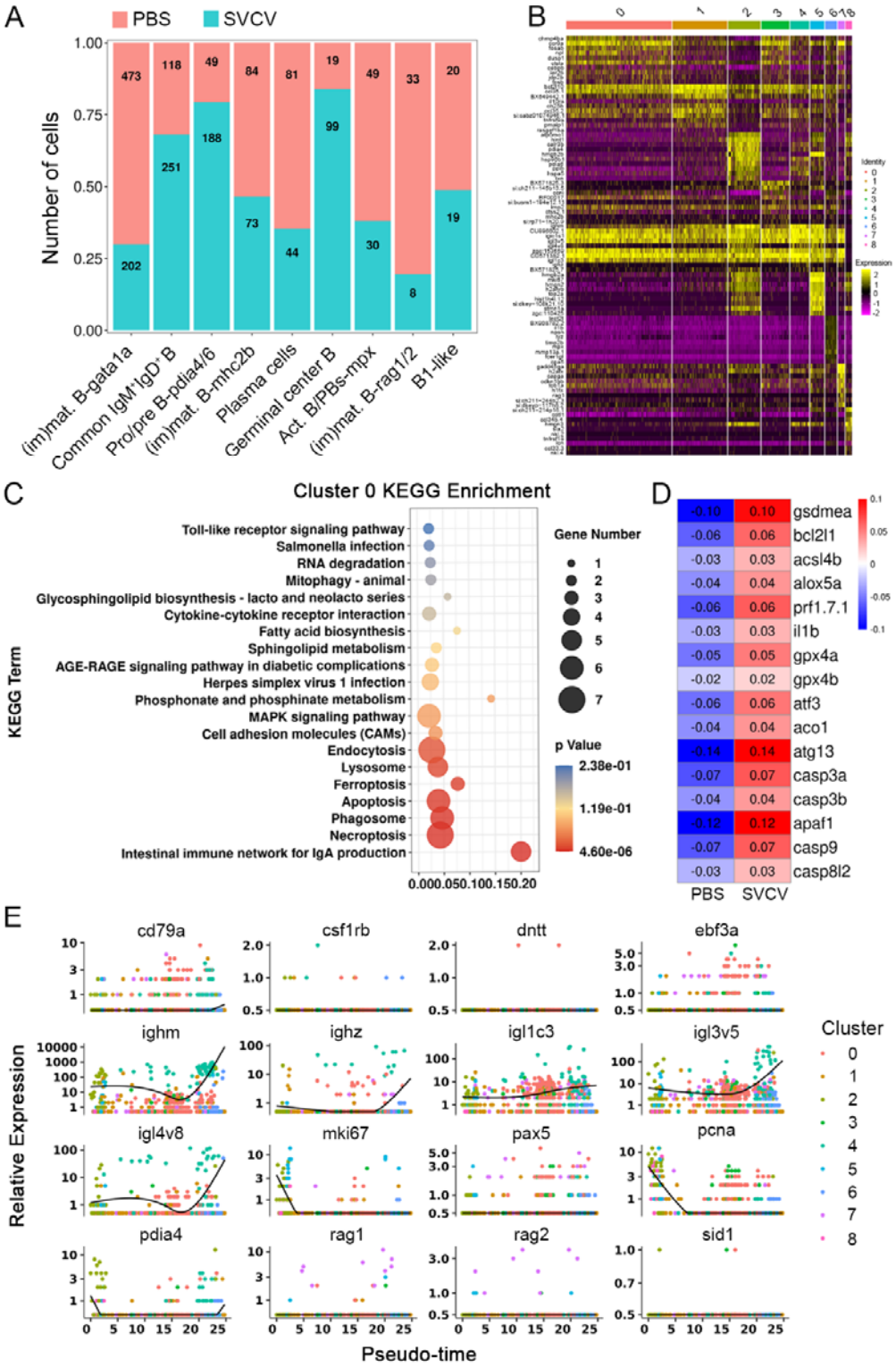

Figure 6-figure supplement 1. Identification of B cell subtype clusters and the expression patterns of marker genes. (**A**) Histogram presenting differences in cell numbers within each cluster between the control group and the SVCV-infected group. (**B**) The top 10 differently expressed genes (DEGs) for each cluster were shown in heatmap. (**C**) Top 20 most significant KEGG pathways for the cluster 0 B-cell subset.

1446 (**D**) Heatmap of the differentially expressed genes for apoptosis, ferroptosis,
1447 necroptosis, and autophagy in the cluster 0 B-cell subset between the control group
1448 and the SVCV-infected group. (**E**) Gene expression dynamics over pseudotime
1449 computed in Monocle2, color-coded by cluster assignment for 16 genes linked to B
1450 cells development.
1451
1452
1453
1454
1455
1456
1457
1458
1459
1460
1461
1462
1463
1464

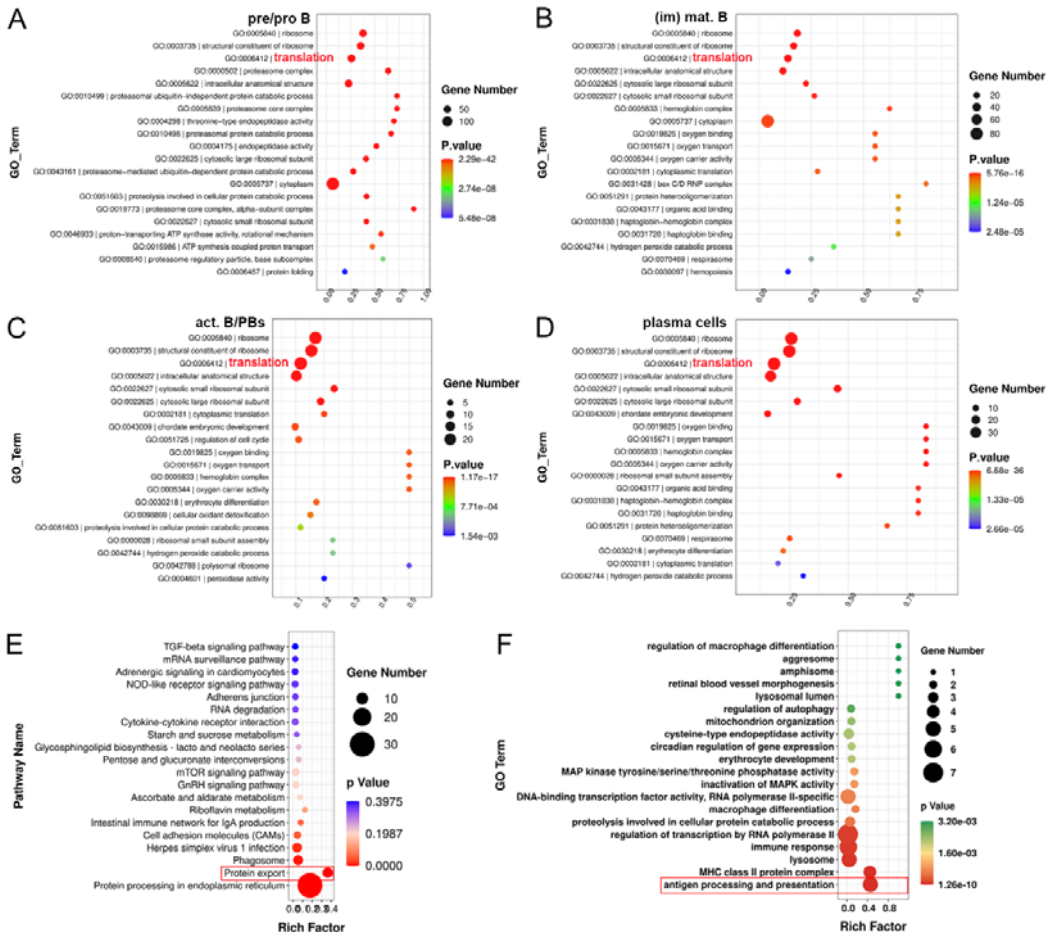

Figure 6-figure supplement 2. GO and KEGG analysis of each cluster of B subset cells. (**A-D**) The top 20 most significant Gene Ontology (GO) terms within the biological process (BP) category for pre/pro B, immature/mature B cells (im/mat. B), activated B cell and plasmablasts (act. B/PBs), and plasma cells (PCs). (**E**) Top 20 most significant KEGG pathways of plasma cells (Cluster 4). (**F**) Top 20 most significant GO terms of (im)mat. B cells (Cluster 3).

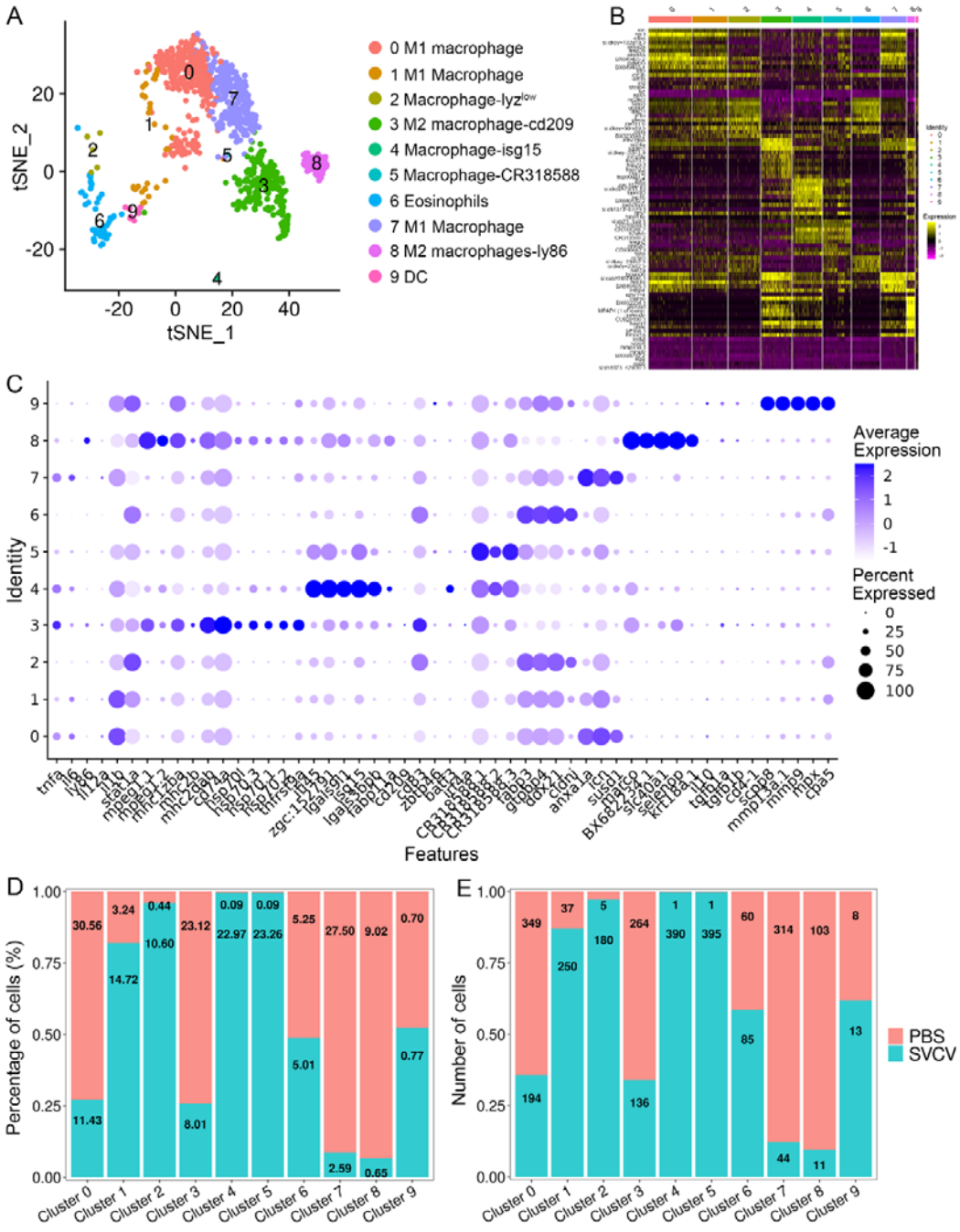

Figure 7. Identification of macrophage/myeloid cell subtypes. (**A**) Graph-based clustering identified 10 macrophage/myeloid cell subclusters within the control group. (**B**) Heatmap displaying marker genes for each cluster. (**C**) Dot plots illustrating marker gene expression levels and the percentages of macrophages/myeloid cells per cluster expressing specific genes. (**D**) Histogram presenting variations in cell ratios between the control group and the SVCV-infected group. (**E**) Histogram illustrating differences in cell numbers within each cluster between the control group and the SVCV-infected group.

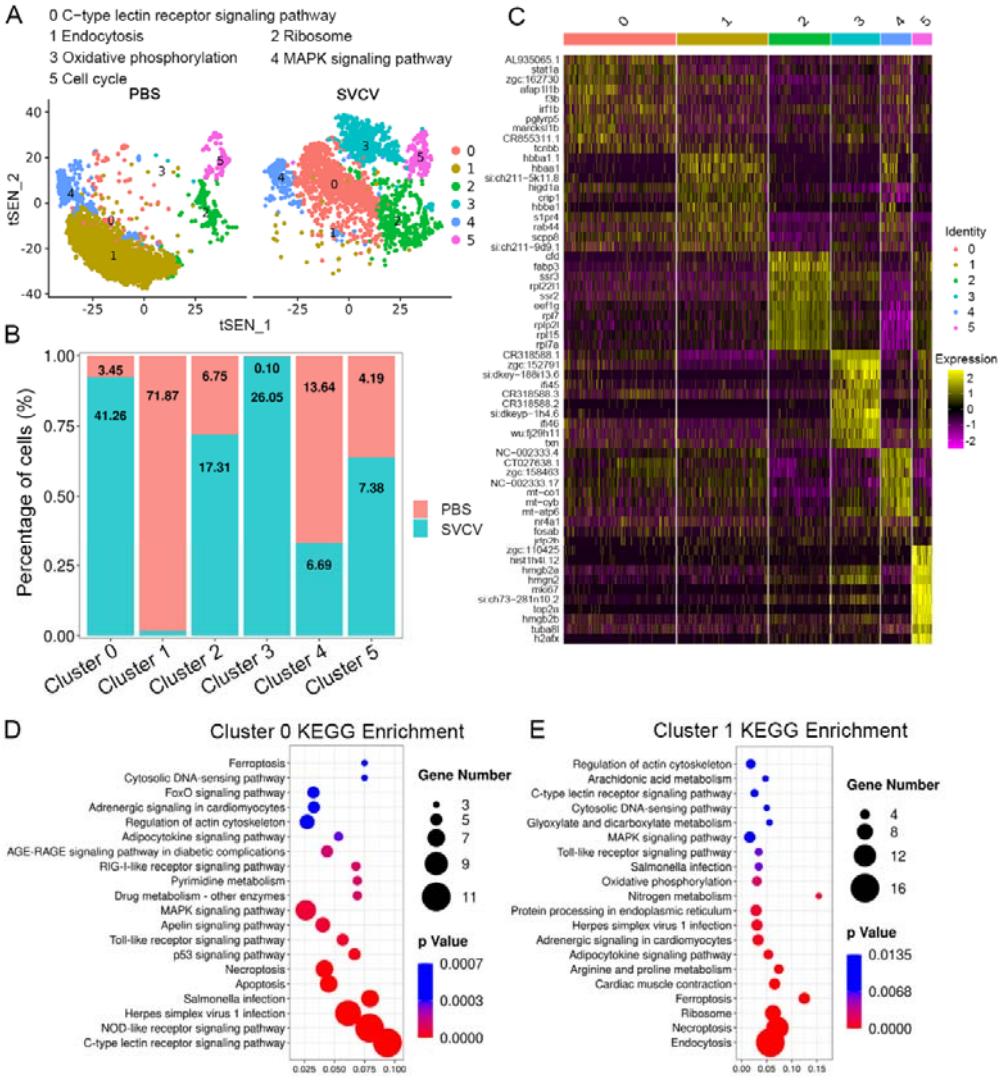

Figure 8. Neutrophil subtype analysis based on single-cell gene expression. (**A**) Graph-based clustering of neutrophils revealed six subclusters within both the control group (PBS) and the SVCV-infected group. Increased and decreased neutrophil subtypes were significant in the SVCV-infected group, with numeric labels indicating cluster percentages. (**B**) Histogram depicting the differing neutrophil ratios between the control group and the SVCV-infected group. (**C**) Heatmap presenting marker gene expression for each cluster. (**D**) KEGG analysis outcomes for cluster 0. RichFactor signifies the ratio of differentially expressed transcripts within the pathway entry to total transcripts located in the entry, indicating enrichment. Q value represents *p* value post multiple hypothesis test correction, with a lower value indicating significant enrichment. The graph sorts top 20 pathways based on ascending Q values. (**E**) KEGG analysis outcomes for cluster 1.

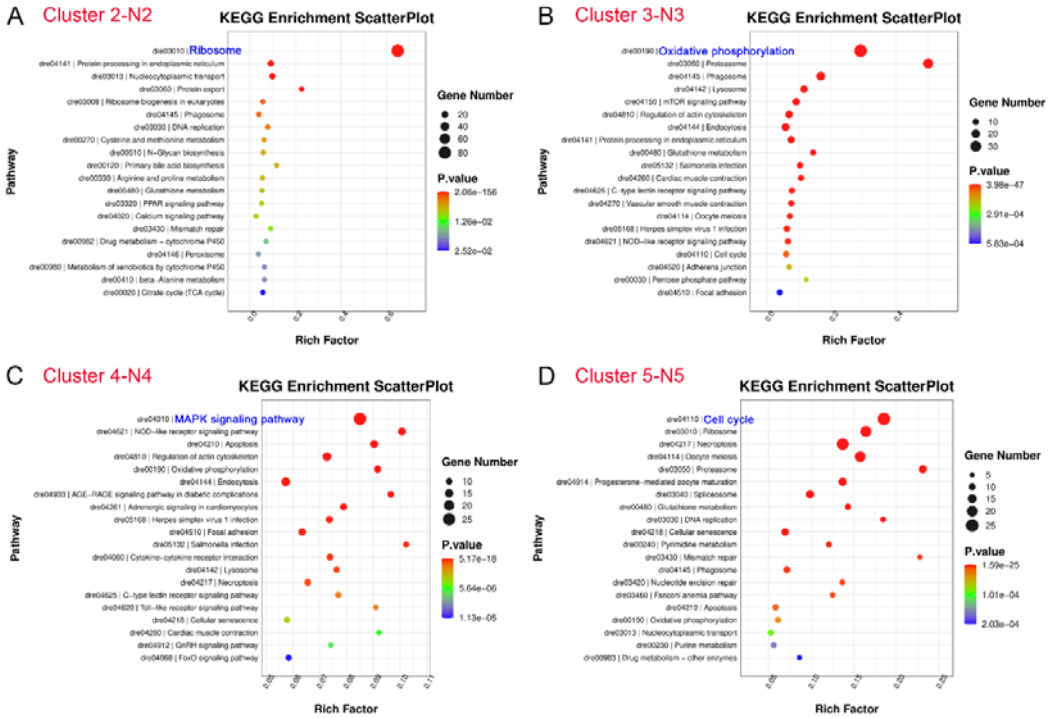

Figure 8-figure supplement 1. KEGG analysis of neutrophil subsets (N2-N5). (**A-D**) Top 20 most significant KEGG pathways of neutrophil subclusters (Cluster 2, 3, 4, 5).

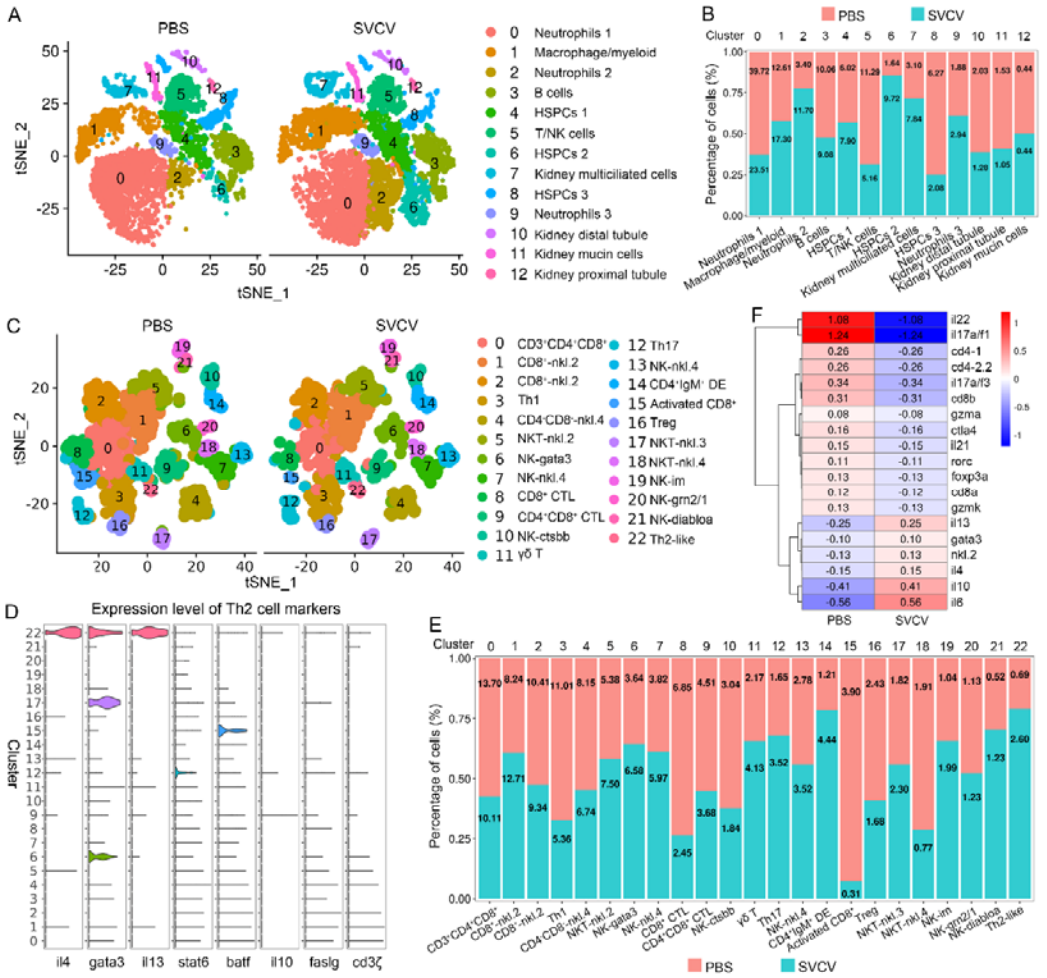

Figure 9. Zebrafish kidney immune-cell and T/NK cell subtype changes upon SVCV infection. (**A**) Nonlinear t-SNE clustering depicted variations in zebrafish kidney leukocyte classification between control (PBS) and SVCV-infected groups. (**B**) Histogram showcasing differences in cell ratios between the control group and the SVCV-infected group. (**C**) Graph-based clustering of T/NK cells demonstrated 23 subclusters within both the control group (PBS) and the SVCV-infected group. Nonlinear t-SNE clustering displayed differences in zebrafish kidney leukocyte classification between control and SVCV-infected groups. (**D**) Violin plots of Th2 cell marker genes across all clusters, displaying normalized gene expression. (**E**) Histogram showing differences in T/NK cell ratios between the control group and the SVCV-infected group. (**F**) Heatmap of significantly differentially expressed marker genes in T/NK cells between the control group and the SVCV-infected group. Gene names are indicated on the right.

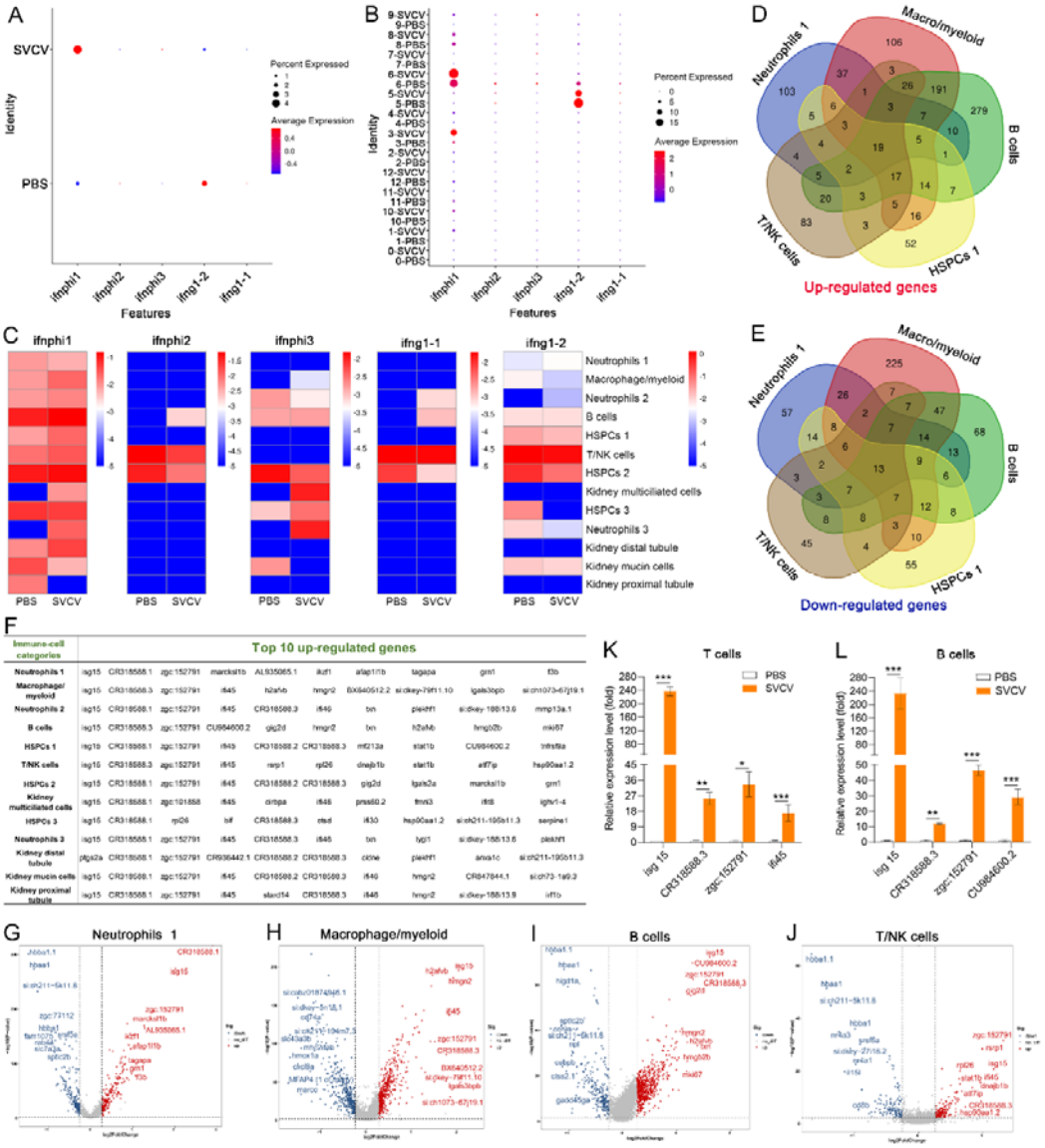

Figure 10. Analysis of IFN-producing cell types and key virus-responsive genes upon SVCV infection. (**A**) Dot plots illustrating five significantly up-/down-regulated IFNs during viral infection in zebrafish kidney immune cells. (**B**) Dot plots showing five differentially expressed IFN genes in each immune cell cluster between control and SVCV-infected zebrafish. (**C**) Heatmap of five differentially expressed IFN genes in each immune cell cluster between control and SVCV-infected zebrafish. (**D-E**) Venn diagram depicting overlapping up-regulated (**D**) and down-regulated (**E**) genes among five major kidney immune-cell categories. (**F**) Top 10 up-regulated genes in each cluster of immune cells and kidney cells. (**G-J**) Volcano plot of DEGs in neutrophils 1 (cluster 0), macrophage/myeloid cells (cluster 1), B cells (cluster 3), and T/NK cells (cluster 5) between the control and SVCV-infected groups. (**K**) RT-qPCR examination of four key virus-responsive genes (*isg15*, *CR318588.3*, *zgc:152791*, and *ifi45*) in T

1530 cells upon SVCV stimulation. (**L**) RT-qPCR examination of four key virus-responsive
1531 genes (*isg15*, *CR318588.3*, *zgc:152791*, and *CU984600.2*) in B cells upon SVCV
1532 stimulation. Error bars represent SD. Data collected from a minimum of three
1533 independent experiments. *$p < 0.05$, **$p < 0.01$, ***$p < 0.001$.
1534
1535
1536

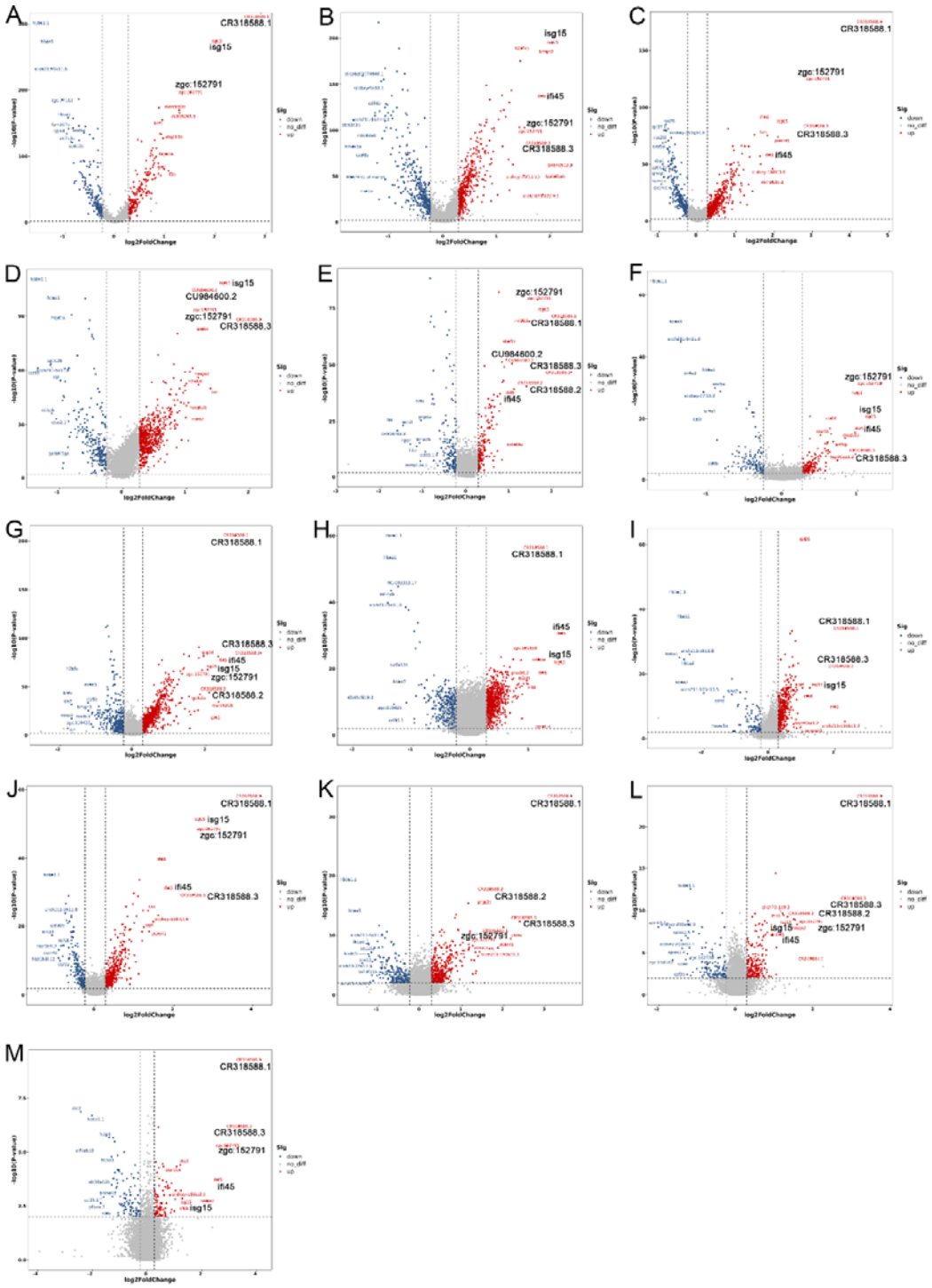

Figure 10-figure supplement 1. Volcano plots showing the DEGs in zebrafish kidney immune-cell and renal cell categories between control (PBS) and SVCV-infected groups (up-regulated: red; down-regulated: blue). (**A**) Neutrophils 1; (**B**) Macrophage/myeloid cells; (**C**) Neutrophils 2; (**D**) B cells; (**E**) HSPCs 1; (**F**) T/NK cells; (**G**) HSPCs 2; (**H**) Kidney multiciliated cells; (**I**) HSPCs 3; (**J**) Neutrophils 3; (**K**) Kidney distal tubule cells; (**L**) Kidney mucin cells; (**M**) Kidney

1544 proximal tubule cells. Some key up-regulated genes are displayed in bold, including
1545 *isg15*, *ifi45*, *zgc:152791*, *CR318588.1*, *CR318588.2* and *CU984600.2.*
1546
1547
1548
1549
1550
1551
1552

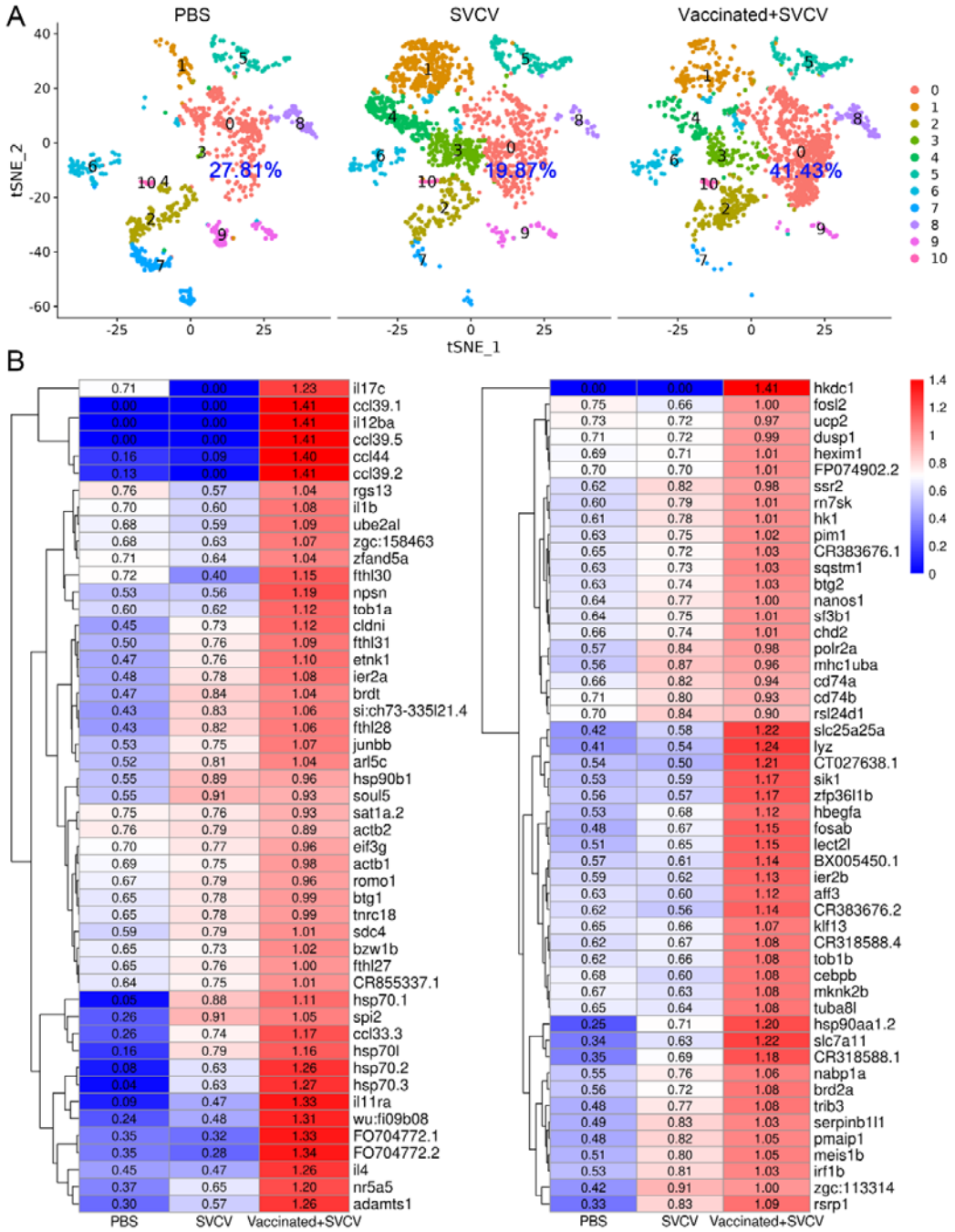

Figure 11. Induction of trained immunity in HSPCs through zebrafish vaccination with inactivated SVCV. (**A**) Nonlinear t-SNE clustering displayed the proportions of HSPCs 1 (H0) in the PBS-administered (control), SVCV-infected (infected), and SVCV-vaccinated plus SVCV-infected (vaccinated+SVCV) groups. (**B**) Heatmap showcasing significant immune gene expression differences in HSPCs 1 (H0) among the PBS-administered, SVCV-infected, and vaccinated+SVCV groups.

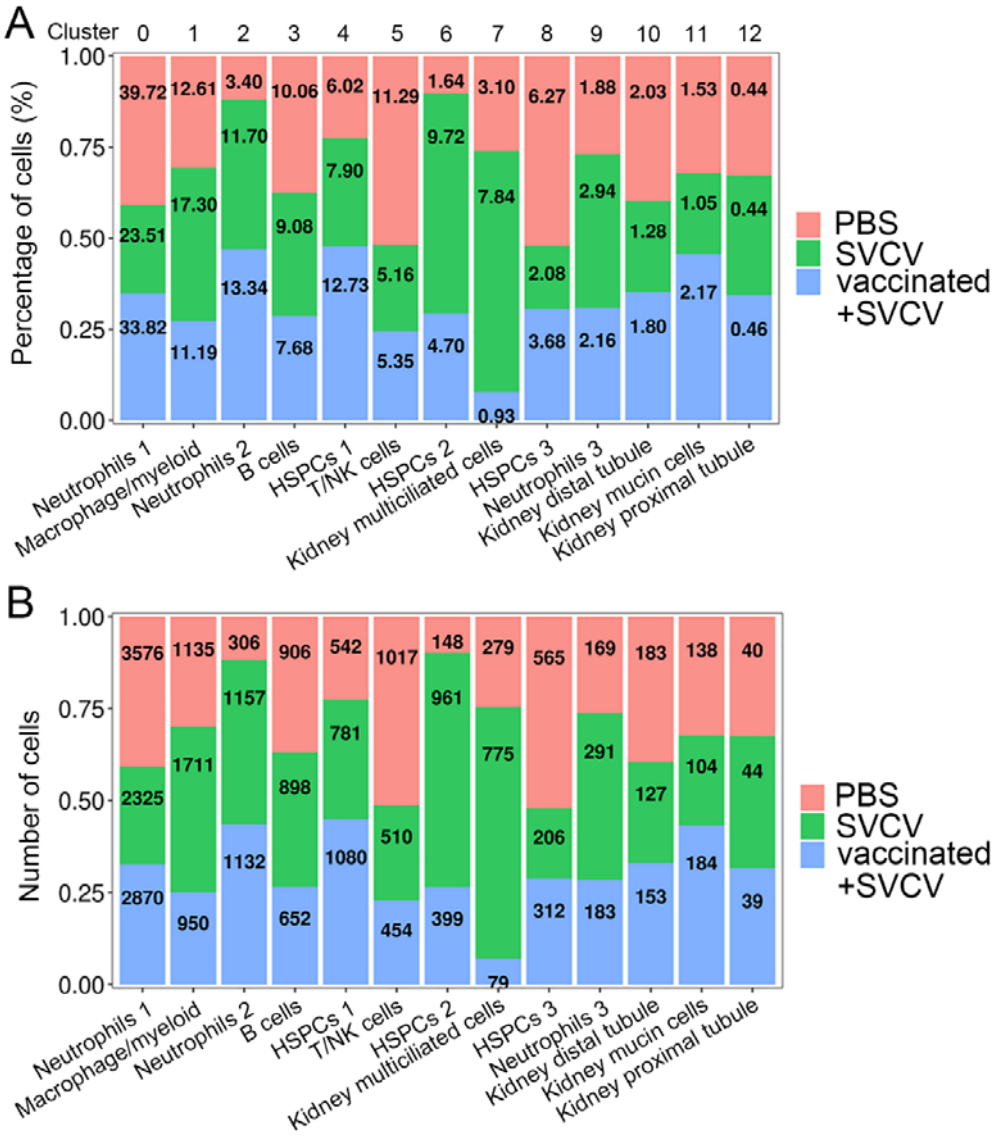

Figure 11-figure supplement 1. Percentage and number changes in zebrafish kidney HSPCs and immune-cell categories in response to SVCV infection. (**A**) Histogram showing the differences in cell ratios between the control group, the SVCV-infected group and the SVCV-vaccinated plus SVCV-infected group. (**B**) Histogram presenting the differences in the cell numbers of each cluster between the control group, the SVCV-infected group and the SVCV-vaccinated plus SVCV-infected group.

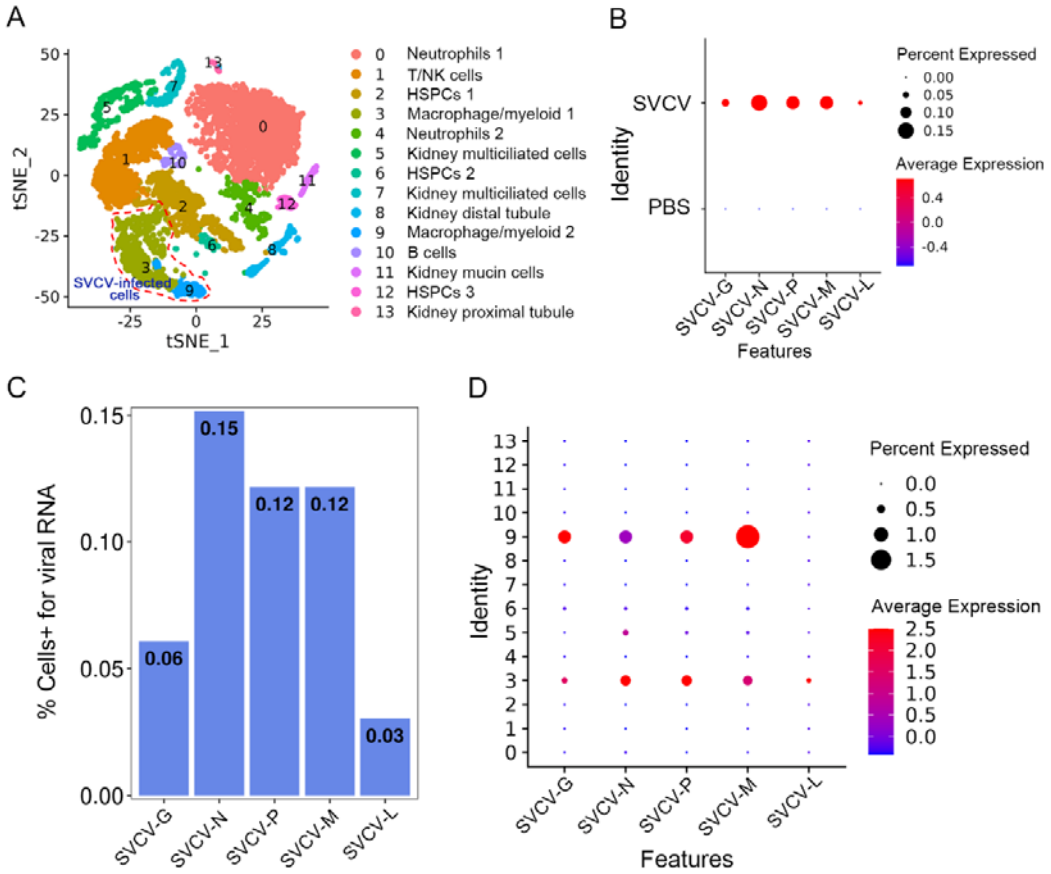

Figure 12. Single-cell sequencing reveals SVCV-infected cells in kidney tissue. (**A**) Nonlinear t-SNE clustering depicted the zebrafish kidney leukocyte classification results after integrating SVCV genes into the zebrafish genome. PCA analysis followed data normalization, and dimension reduction was achieved via principal component analysis and graph theory-based clustering. The infected cell populations are displayed in red dashed circles. (**B**) Dot plots illustrating expression levels of five SVCV genes and percentage of cells per cluster expressing these genes. (**C**) Percentage of scRNA-seq-identified cells positive for reads aligning to the viral genome in SVCV-infected cases. (**D**) Dot plots showing differential expression of five SVCV genes per immune cell cluster in SVCV-infected zebrafish.

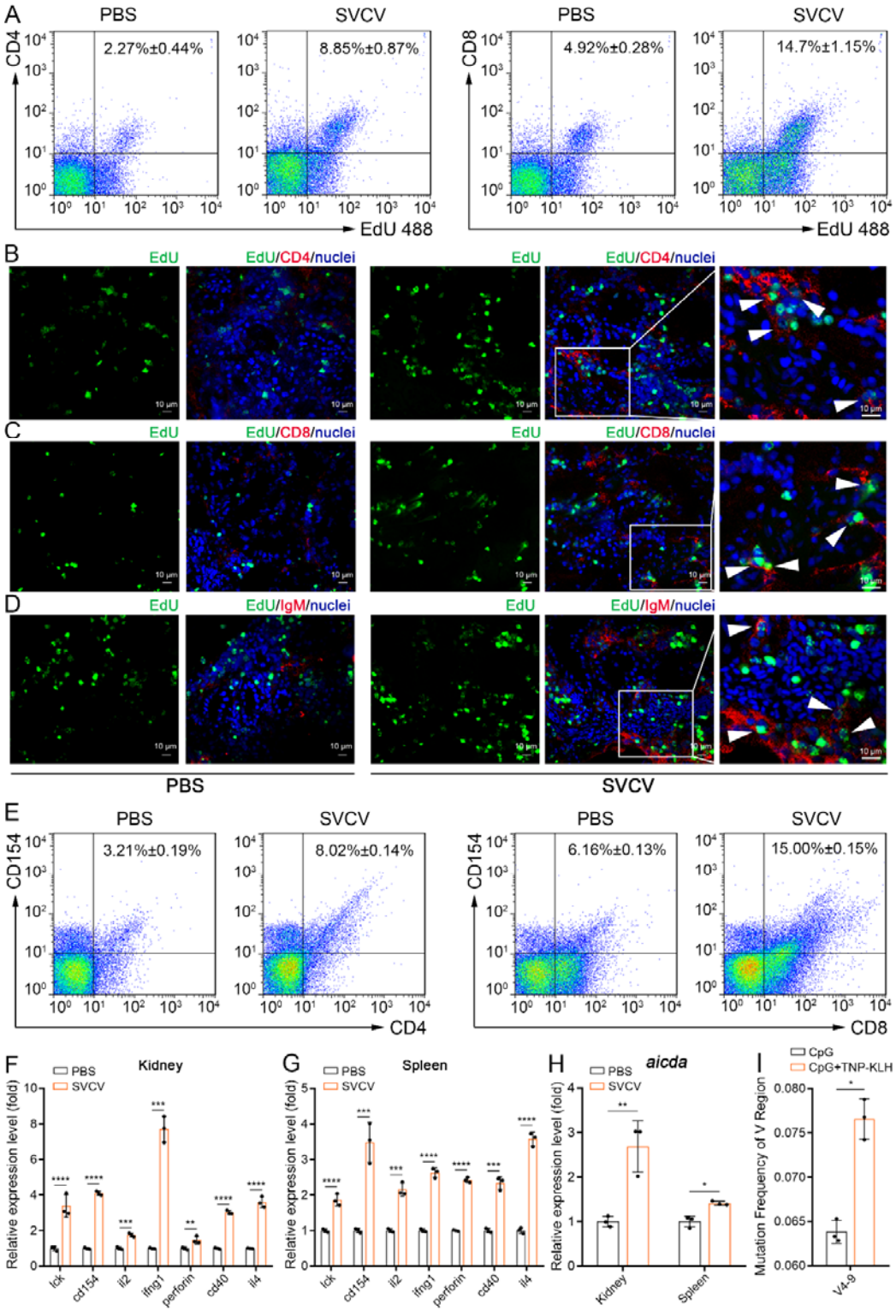

Figure 13. Examination of zebrafish kidney acting as a secondary immune organ involved in the antiviral immune response. (**A**) In vivo proliferation assessment of $CD4^+$ and $CD8^+$ T cells in kidney of zebrafish stimulated with inactivated SVCV (10^6 $TCID_{50}$), determined by $CD4^+EdU^+$ and $CD8^+EdU^+$ T cell percentages via FCM

1588 analysis. (**B-D**) Analysis of proliferative $CD4^+$ T, $CD8^+$ T and IgM^+ B cells by
1589 immunofluorescence staining. Kidney cryosections were stained for EdU (green),
1590 CD4 (red, B), CD8 (red, C) and IgM (red, D), and nuclei (blue) detection.
1591 Fluorescence images were captured using Laser scanning confocal microscope
1592 (FV3000, 60 × oil). White arrowheads point to cells double stained for EdU with CD4,
1593 CD8 or IgM. Scale bars, 10 μm. (**E**) In vivo activation examination of $CD4^+$ and
1594 $CD8^+$ T cells after SVCV stimulation, determined by $CD4^+CD154^+$ and $CD8^+CD154^+$
1595 T cell percentages via FCM analysis. (**F-G**) RT-qPCR analysis of transcriptional
1596 expression of T/B cell activation-related genes in kidney and spleen under SVCV
1597 stimulation. (**H**) RT-qPCR analysis of B cell SHM-related gene AID (*aicda*)
1598 transcriptional expression in kidney and spleen under SVCV stimulation. (**I**) SHM
1599 analysis in IgM antibody V genes through multiple PCR-based high-throughput
1600 sequencing. Experiments were independently repeated at least three times (*$p < 0.05$,
1601 **$p < 0.01$, ***$p < 0.001$, ****$p < 0.0001$).

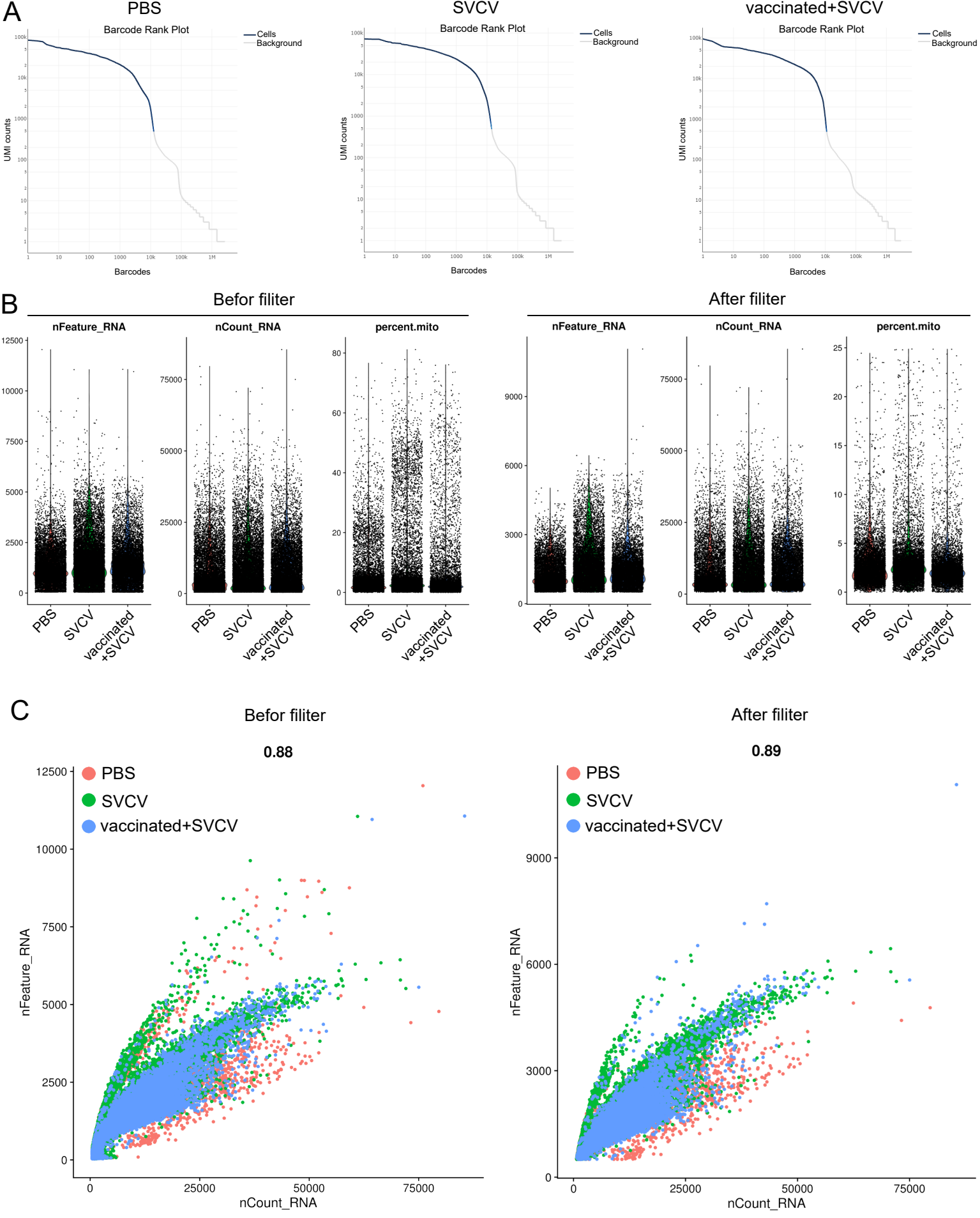
A
PBS
SVCV
vaccinated+SVCV
Barcode Rank Plot
Cells
Background
UMI counts
Barcodes
B
Befor filiter
After filiter
nFeature_RNA
nCount_RNA
percent.mito
PBS
SVCV
vaccinated +SVCV
C
Befor filiter
After filiter
0.88
0.89
PBS
SVCV
vaccinated+SVCV
nFeature_RNA
nCount_RNA

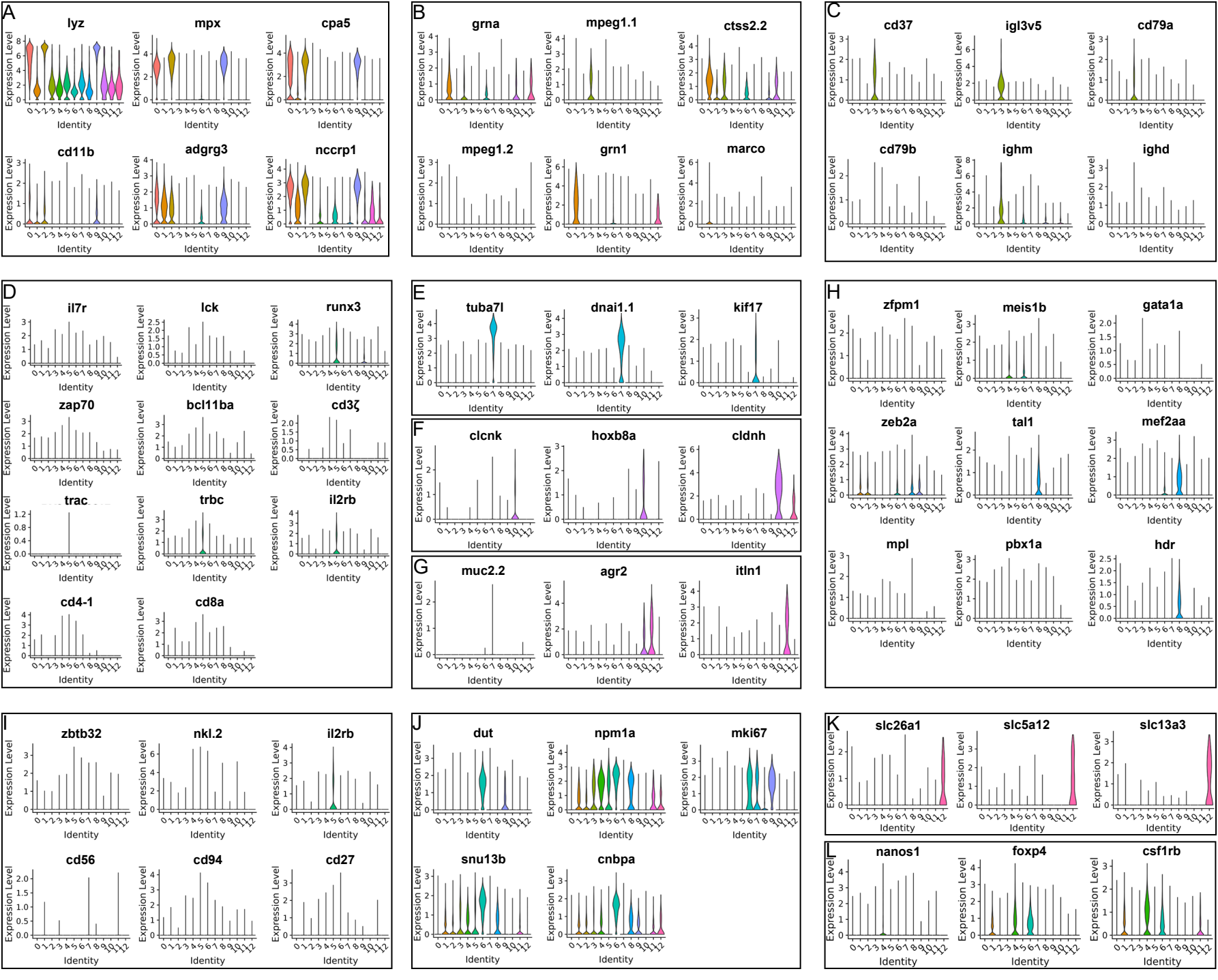
A
lyz
mpx
cpa5
cd11b
adgrg3
nccrp1
B
grna
mpeg1.1
ctss2.2
mpeg1.2
grn1
marco
C
cd37
igl3v5
cd79a
cd79b
ighm
ighd
D
il7r
lck
runx3
zap70
bcl11ba
cd3ζ
trac
trbc
il2rb
cd4-1
cd8a
E
tuba7l
dnai1.1
kif17
F
clcnk
hoxb8a
cldnh
G
muc2.2
agr2
itln1
H
zfpm1
meis1b
gata1a
zeb2a
tal1
mef2aa
mpl
pbx1a
hdr
I
zbtb32
nkl.2
il2rb
cd56
cd94
cd27
J
dut
npm1a
mki67
snu13b
cnbpa
K
slc26a1
slc5a12
slc13a3
L
nanos1
foxp4
csf1rb
Expression Level
Identity

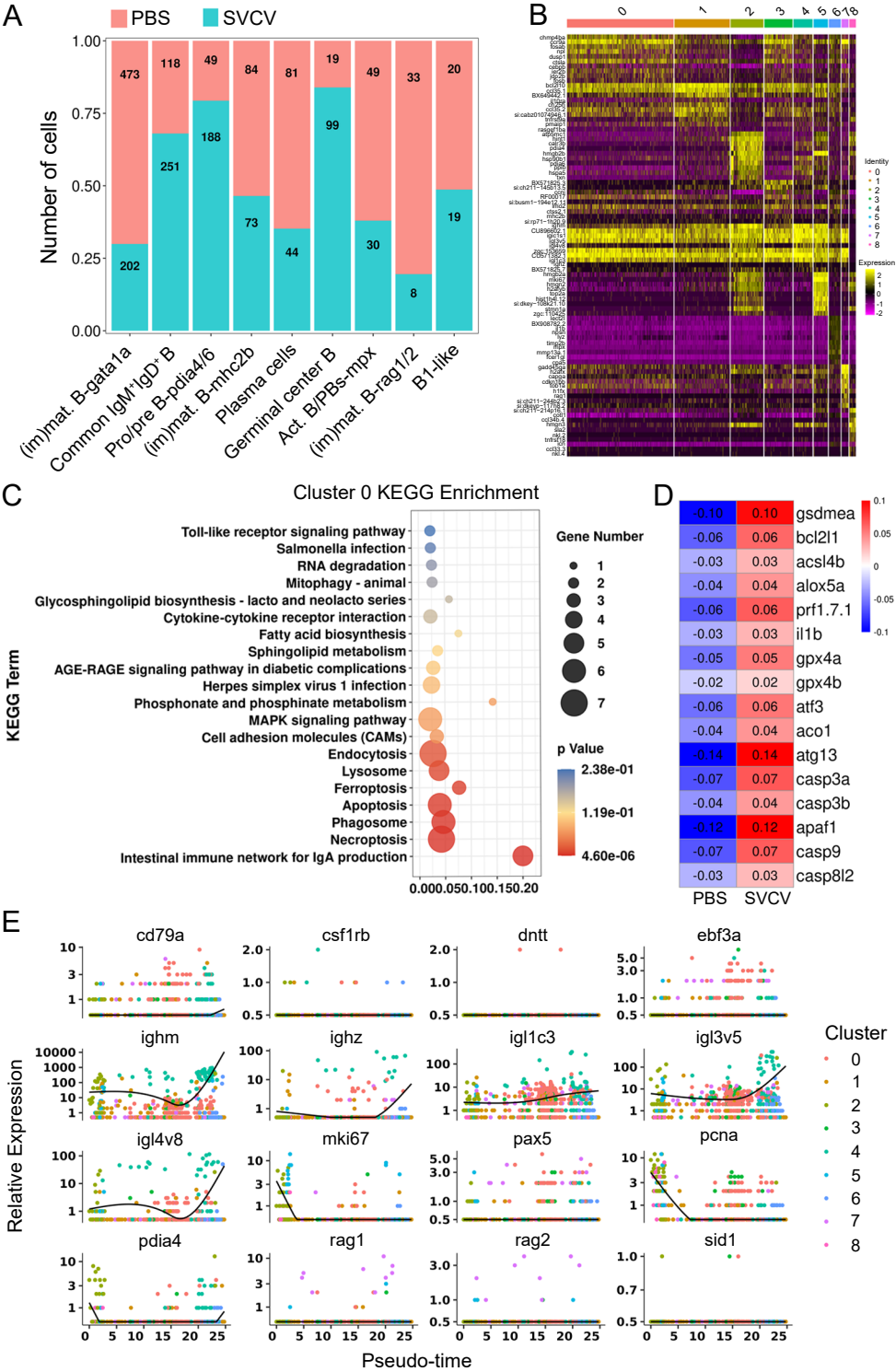
A
PBS
SVCV
Number of cells
1.00
0.75
0.50
0.25
0.00
473
202
118
251
49
188
84
73
81
44
19
99
49
30
33
8
20
19
(im)mat. B-gata1a
Common IgM+IgD+ B
Pro/pre B-pdia4/6
(im)mat. B-mhc2b
Plasma cells
Germinal center B
Act. B/PBs-mpx
(im)mat. B-rag1/2
B1-like
B
0
1
2
3
4
5
6
7
8
Identity
Expression
C
Cluster 0 KEGG Enrichment
KEGG Term
Toll-like receptor signaling pathway
Salmonella infection
RNA degradation
Mitophagy - animal
Glycosphingolipid biosynthesis - lacto and neolacto series
Cytokine-cytokine receptor interaction
Fatty acid biosynthesis
Sphingolipid metabolism
AGE-RAGE signaling pathway in diabetic complications
Herpes simplex virus 1 infection
Phosphonate and phosphinate metabolism
MAPK signaling pathway
Cell adhesion molecules (CAMs)
Endocytosis
Lysosome
Ferroptosis
Apoptosis
Phagosome
Necroptosis
Intestinal immune network for IgA production
0.00
0.05
0.10
0.15
0.20
Gene Number
1
2
3
4
5
6
7
p Value
2.38e-01
1.19e-01
4.60e-06
D
gsdmea -0.10 0.10
bcl2l1 -0.06 0.06
acsl4b -0.03 0.03
alox5a -0.04 0.04
prf1.7.1 -0.06 0.06
il1b -0.03 0.03
gpx4a -0.05 0.05
gpx4b -0.02 0.02
atf3 -0.06 0.06
aco1 -0.04 0.04
atg13 -0.14 0.14
casp3a -0.07 0.07
casp3b -0.04 0.04
apaf1 -0.12 0.12
casp9 -0.07 0.07
casp8l2 -0.03 0.03
PBS
SVCV
0.1
0.05
0
-0.05
-0.1
E
cd79a
csf1rb
dntt
ebf3a
ighm
ighz
igl1c3
igl3v5
igl4v8
mki67
pax5
pcna
pdia4
rag1
rag2
sid1
Relative Expression
Pseudo-time
Cluster
0
1
2
3
4
5
6
7
8

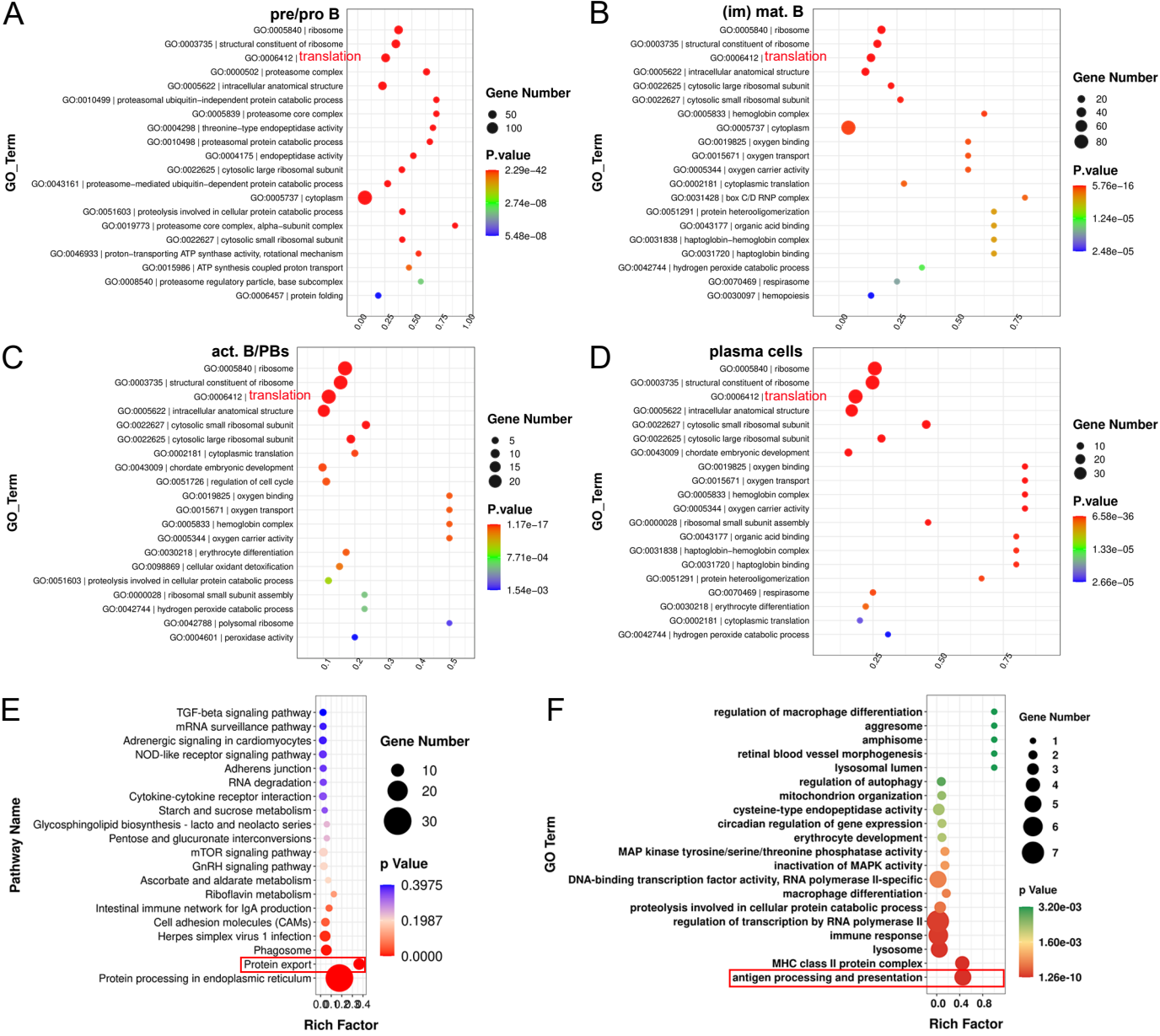
A
pre/pro B
GO_Term
GO:0005840 | ribosome
GO:0003735 | structural constituent of ribosome
GO:0006412 | translation
GO:0000502 | proteasome complex
GO:0005622 | intracellular anatomical structure
GO:0010499 | proteasomal ubiquitin–independent protein catabolic process
GO:0005839 | proteasome core complex
GO:0004298 | threonine–type endopeptidase activity
GO:0010498 | proteasomal protein catabolic process
GO:0004175 | endopeptidase activity
GO:0022625 | cytosolic large ribosomal subunit
GO:0043161 | proteasome–mediated ubiquitin–dependent protein catabolic process
GO:0005737 | cytoplasm
GO:0051603 | proteolysis involved in cellular protein catabolic process
GO:0019773 | proteasome core complex, alpha–subunit complex
GO:0022627 | cytosolic small ribosomal subunit
GO:0046933 | proton–transporting ATP synthase activity, rotational mechanism
GO:0015986 | ATP synthesis coupled proton transport
GO:0008540 | proteasome regulatory particle, base subcomplex
GO:0006457 | protein folding
0.00 0.25 0.50 0.75 1.00
Gene Number
50
100
P.value
2.29e−42
2.74e−08
5.48e−08
B
(im) mat. B
GO_Term
GO:0005840 | ribosome
GO:0003735 | structural constituent of ribosome
GO:0006412 | translation
GO:0005622 | intracellular anatomical structure
GO:0022625 | cytosolic large ribosomal subunit
GO:0022627 | cytosolic small ribosomal subunit
GO:0005833 | hemoglobin complex
GO:0005737 | cytoplasm
GO:0019825 | oxygen binding
GO:0015671 | oxygen transport
GO:0005344 | oxygen carrier activity
GO:0002181 | cytoplasmic translation
GO:0031428 | box C/D RNP complex
GO:0051291 | protein heterooligomerization
GO:0043177 | organic acid binding
GO:0031838 | haptoglobin–hemoglobin complex
GO:0031720 | haptoglobin binding
GO:0042744 | hydrogen peroxide catabolic process
GO:0070469 | respirasome
GO:0030097 | hemopoiesis
0.00 0.25 0.50 0.75
Gene Number
20
40
60
80
P.value
5.76e−16
1.24e−05
2.48e−05
C
act. B/PBs
GO_Term
GO:0005840 | ribosome
GO:0003735 | structural constituent of ribosome
GO:0006412 | translation
GO:0005622 | intracellular anatomical structure
GO:0022627 | cytosolic small ribosomal subunit
GO:0022625 | cytosolic large ribosomal subunit
GO:0002181 | cytoplasmic translation
GO:0043009 | chordate embryonic development
GO:0051726 | regulation of cell cycle
GO:0019825 | oxygen binding
GO:0015671 | oxygen transport
GO:0005833 | hemoglobin complex
GO:0005344 | oxygen carrier activity
GO:0030218 | erythrocyte differentiation
GO:0098869 | cellular oxidant detoxification
GO:0051603 | proteolysis involved in cellular protein catabolic process
GO:0000028 | ribosomal small subunit assembly
GO:0042744 | hydrogen peroxide catabolic process
GO:0042788 | polysomal ribosome
GO:0004601 | peroxidase activity
0.1 0.2 0.3 0.4 0.5
Gene Number
5
10
15
20
P.value
1.17e−17
7.71e−04
1.54e−03
D
plasma cells
GO_Term
GO:0005840 | ribosome
GO:0003735 | structural constituent of ribosome
GO:0006412 | translation
GO:0005622 | intracellular anatomical structure
GO:0022627 | cytosolic small ribosomal subunit
GO:0022625 | cytosolic large ribosomal subunit
GO:0043009 | chordate embryonic development
GO:0019825 | oxygen binding
GO:0015671 | oxygen transport
GO:0005833 | hemoglobin complex
GO:0005344 | oxygen carrier activity
GO:0000028 | ribosomal small subunit assembly
GO:0043177 | organic acid binding
GO:0031838 | haptoglobin–hemoglobin complex
GO:0031720 | haptoglobin binding
GO:0051291 | protein heterooligomerization
GO:0070469 | respirasome
GO:0030218 | erythrocyte differentiation
GO:0002181 | cytoplasmic translation
GO:0042744 | hydrogen peroxide catabolic process
0.25 0.50 0.75
Gene Number
10
20
30
P.value
6.58e−36
1.33e−05
2.66e−05
E
Pathway Name
TGF-beta signaling pathway
mRNA surveillance pathway
Adrenergic signaling in cardiomyocytes
NOD-like receptor signaling pathway
Adherens junction
RNA degradation
Cytokine-cytokine receptor interaction
Starch and sucrose metabolism
Glycosphingolipid biosynthesis - lacto and neolacto series
Pentose and glucuronate interconversions
mTOR signaling pathway
GnRH signaling pathway
Ascorbate and aldarate metabolism
Riboflavin metabolism
Intestinal immune network for IgA production
Cell adhesion molecules (CAMs)
Herpes simplex virus 1 infection
Phagosome
Protein export
Protein processing in endoplasmic reticulum
Rich Factor
Gene Number
10
20
30
p Value
0.3975
0.1987
0.0000
F
GO Term
regulation of macrophage differentiation
aggresome
amphisome
retinal blood vessel morphogenesis
lysosomal lumen
regulation of autophagy
mitochondrion organization
cysteine-type endopeptidase activity
circadian regulation of gene expression
erythrocyte development
MAP kinase tyrosine/serine/threonine phosphatase activity
inactivation of MAPK activity
DNA-binding transcription factor activity, RNA polymerase II-specific
macrophage differentiation
proteolysis involved in cellular protein catabolic process
regulation of transcription by RNA polymerase II
immune response
lysosome
MHC class II protein complex
antigen processing and presentation
0.0 0.4 0.8
Rich Factor
Gene Number
1
2
3
4
5
6
7
p Value
3.20e-03
1.60e-03
1.26e-10

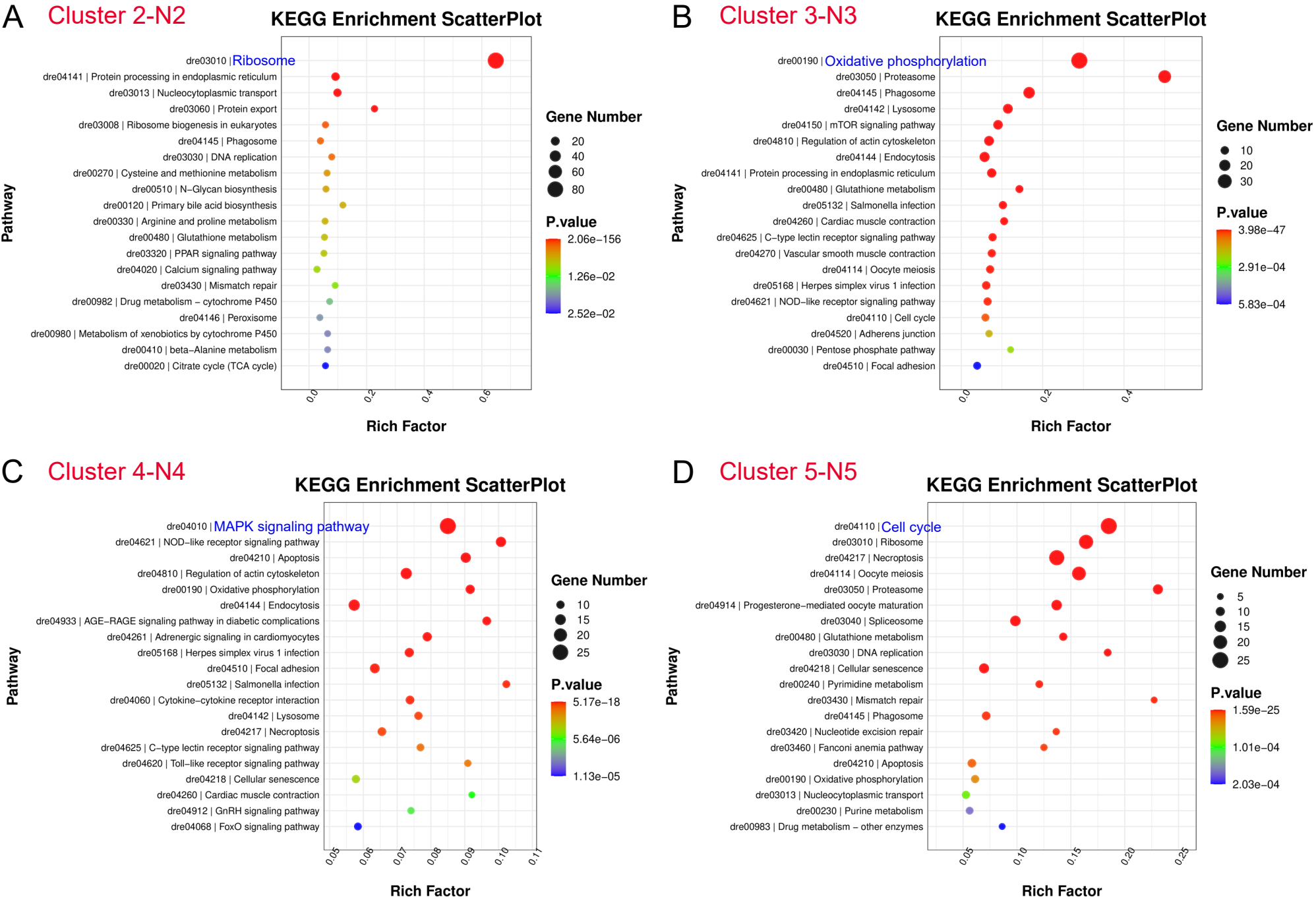
A
Cluster 2-N2
KEGG Enrichment ScatterPlot
dre03010 | Ribosome
dre04141 | Protein processing in endoplasmic reticulum
dre03013 | Nucleocytoplasmic transport
dre03060 | Protein export
dre03008 | Ribosome biogenesis in eukaryotes
dre04145 | Phagosome
dre03030 | DNA replication
dre00270 | Cysteine and methionine metabolism
dre00510 | N−Glycan biosynthesis
dre00120 | Primary bile acid biosynthesis
dre00330 | Arginine and proline metabolism
dre00480 | Glutathione metabolism
dre03320 | PPAR signaling pathway
dre04020 | Calcium signaling pathway
dre03430 | Mismatch repair
dre00982 | Drug metabolism − cytochrome P450
dre04146 | Peroxisome
dre00980 | Metabolism of xenobiotics by cytochrome P450
dre00410 | beta−Alanine metabolism
dre00020 | Citrate cycle (TCA cycle)
Pathway
0.0
0.2
0.4
0.6
Rich Factor
Gene Number
20
40
60
80
P.value
2.06e−156
1.26e−02
2.52e−02
B
Cluster 3-N3
KEGG Enrichment ScatterPlot
dre00190 | Oxidative phosphorylation
dre03050 | Proteasome
dre04145 | Phagosome
dre04142 | Lysosome
dre04150 | mTOR signaling pathway
dre04810 | Regulation of actin cytoskeleton
dre04144 | Endocytosis
dre04141 | Protein processing in endoplasmic reticulum
dre00480 | Glutathione metabolism
dre05132 | Salmonella infection
dre04260 | Cardiac muscle contraction
dre04625 | C−type lectin receptor signaling pathway
dre04270 | Vascular smooth muscle contraction
dre04114 | Oocyte meiosis
dre05168 | Herpes simplex virus 1 infection
dre04621 | NOD−like receptor signaling pathway
dre04110 | Cell cycle
dre04520 | Adherens junction
dre00030 | Pentose phosphate pathway
dre04510 | Focal adhesion
Pathway
0.0
0.2
0.4
Rich Factor
Gene Number
10
20
30
P.value
3.98e−47
2.91e−04
5.83e−04
C
Cluster 4-N4
KEGG Enrichment ScatterPlot
dre04010 | MAPK signaling pathway
dre04621 | NOD−like receptor signaling pathway
dre04210 | Apoptosis
dre04810 | Regulation of actin cytoskeleton
dre00190 | Oxidative phosphorylation
dre04144 | Endocytosis
dre04933 | AGE−RAGE signaling pathway in diabetic complications
dre04261 | Adrenergic signaling in cardiomyocytes
dre05168 | Herpes simplex virus 1 infection
dre04510 | Focal adhesion
dre05132 | Salmonella infection
dre04060 | Cytokine−cytokine receptor interaction
dre04142 | Lysosome
dre04217 | Necroptosis
dre04625 | C−type lectin receptor signaling pathway
dre04620 | Toll−like receptor signaling pathway
dre04218 | Cellular senescence
dre04260 | Cardiac muscle contraction
dre04912 | GnRH signaling pathway
dre04068 | FoxO signaling pathway
Pathway
0.05
0.06
0.07
0.08
0.09
0.10
0.11
Rich Factor
Gene Number
10
15
20
25
P.value
5.17e−18
5.64e−06
1.13e−05
D
Cluster 5-N5
KEGG Enrichment ScatterPlot
dre04110 | Cell cycle
dre03010 | Ribosome
dre04217 | Necroptosis
dre04114 | Oocyte meiosis
dre03050 | Proteasome
dre04914 | Progesterone−mediated oocyte maturation
dre03040 | Spliceosome
dre00480 | Glutathione metabolism
dre03030 | DNA replication
dre04218 | Cellular senescence
dre00240 | Pyrimidine metabolism
dre03430 | Mismatch repair
dre04145 | Phagosome
dre03420 | Nucleotide excision repair
dre03460 | Fanconi anemia pathway
dre04210 | Apoptosis
dre00190 | Oxidative phosphorylation
dre03013 | Nucleocytoplasmic transport
dre00230 | Purine metabolism
dre00983 | Drug metabolism − other enzymes
Pathway
0.05
0.10
0.15
0.20
0.25
Rich Factor
Gene Number
5
10
15
20
25
P.value
1.59e−25
1.01e−04
2.03e−04

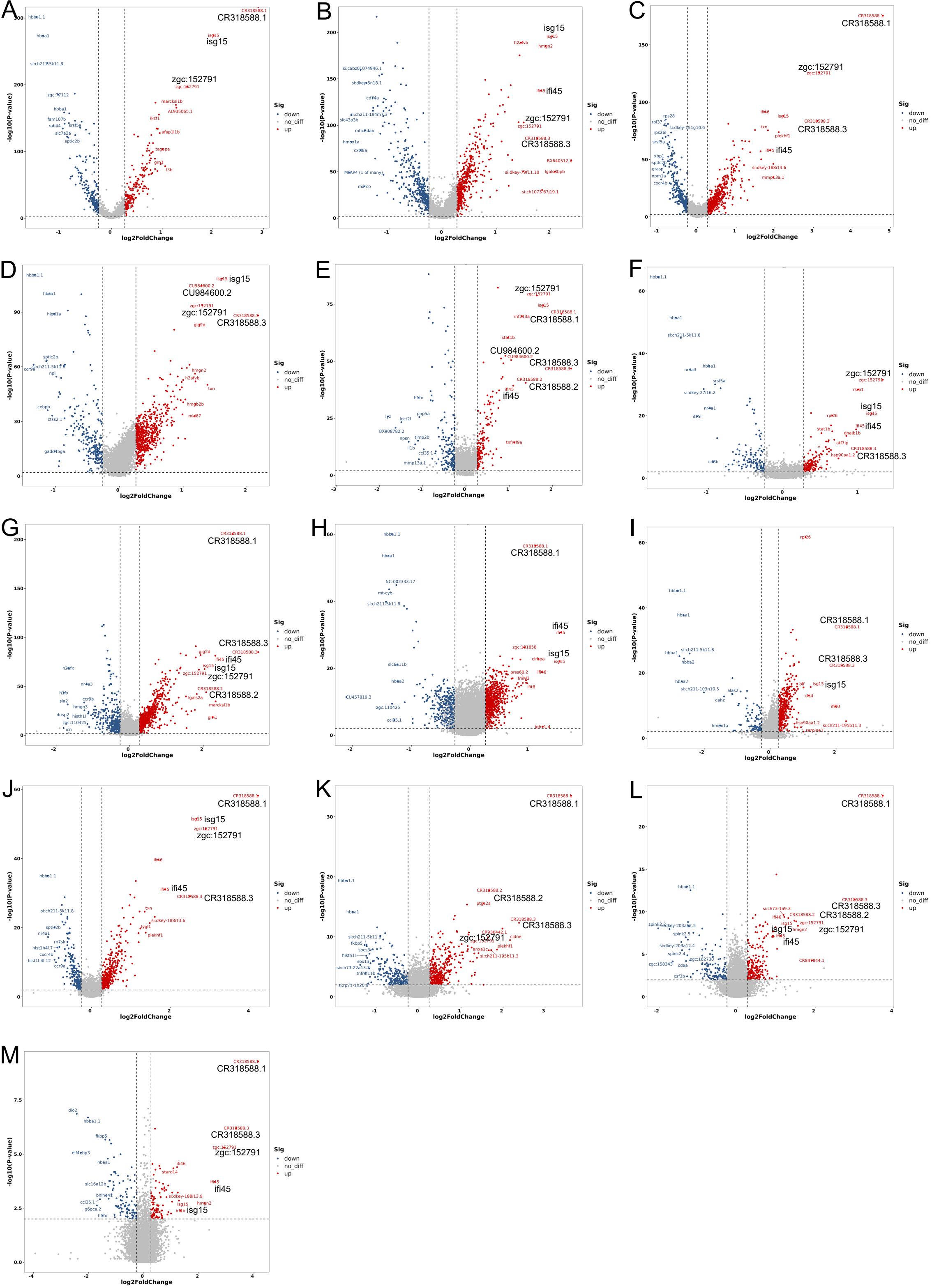
A
CR318588.1
isg15
zgc:152791
B
isg15
ifi45
zgc:152791
CR318588.3
C
CR318588.1
zgc:152791
CR318588.3
ifi45
D
isg15
CU984600.2
zgc:152791
CR318588.3
E
zgc:152791
CR318588.1
CU984600.2
CR318588.3
CR318588.2
ifi45
F
zgc:152791
isg15
ifi45
CR318588.3
G
CR318588.1
CR318588.3
ifi45
isg15
zgc:152791
CR318588.2
H
CR318588.1
ifi45
isg15
I
CR318588.1
CR318588.3
isg15
J
CR318588.1
isg15
zgc:152791
ifi45
CR318588.3
K
CR318588.1
CR318588.2
CR318588.3
zgc:152791
L
CR318588.1
CR318588.3
CR318588.2
isg15
zgc:152791
ifi45
M
CR318588.1
CR318588.3
zgc:152791
ifi45
isg15
-log10(P-value)
log2FoldChange
Sig
down
no_diff
up

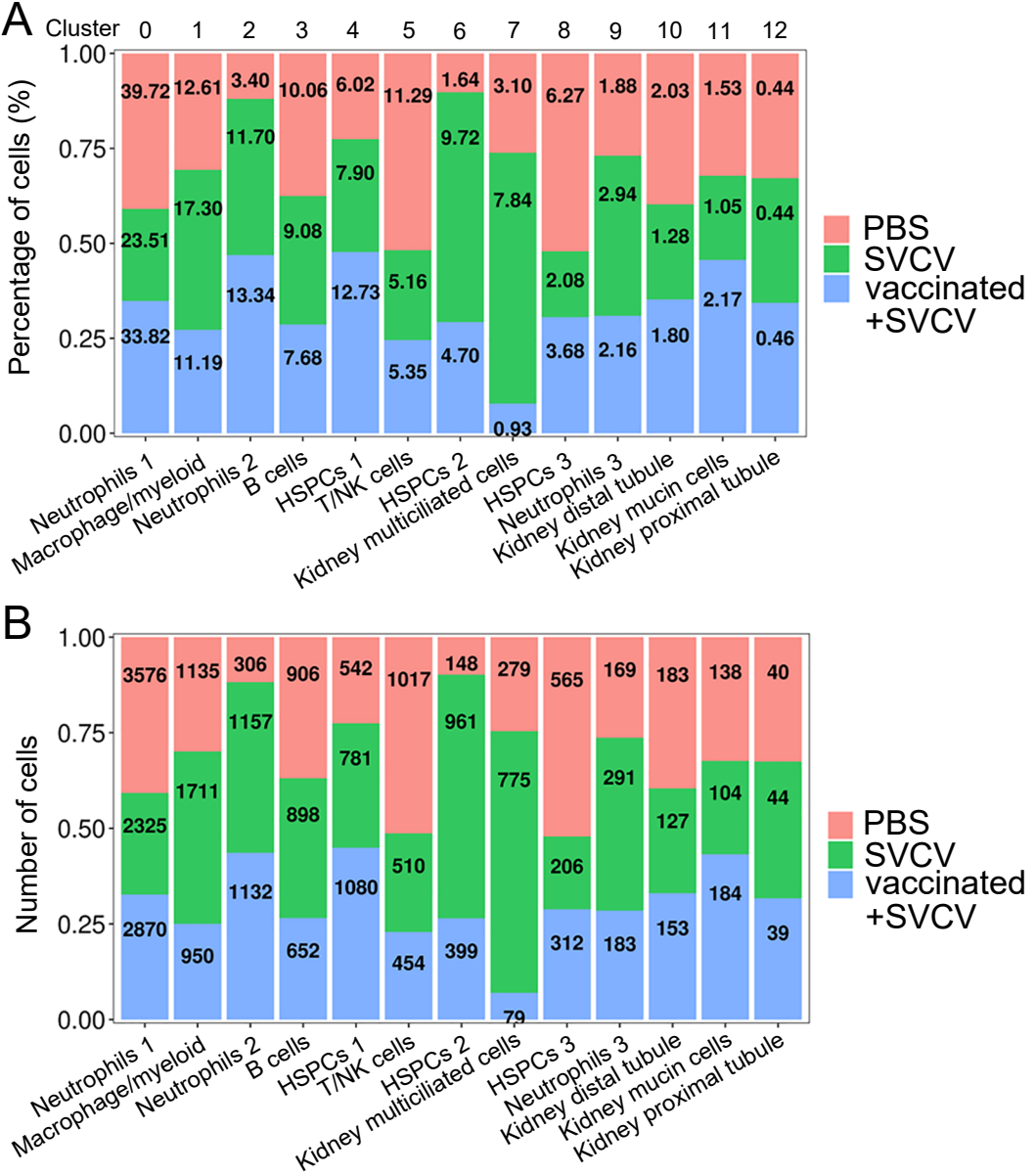
A
Cluster 0 1 2 3 4 5 6 7 8 9 10 11 12
Percentage of cells (%)
1.00
0.75
0.50
0.25
0.00
39.72 12.61 3.40 10.06 6.02 11.29 1.64 3.10 6.27 1.88 2.03 1.53 0.44
23.51 17.30 11.70 9.08 7.90 5.16 9.72 7.84 2.08 2.94 1.28 1.05 0.44
33.82 11.19 13.34 7.68 12.73 5.35 4.70 0.93 3.68 2.16 1.80 2.17 0.46
PBS
SVCV
vaccinated +SVCV
Neutrophils 1
Macrophage/myeloid
Neutrophils 2
B cells
HSPCs 1
T/NK cells
HSPCs 2
Kidney multiciliated cells
HSPCs 3
Neutrophils 3
Kidney distal tubule
Kidney mucin cells
Kidney proximal tubule
B
Number of cells
1.00
0.75
0.50
0.25
0.00
3576 1135 306 906 542 1017 148 279 565 169 183 138 40
2325 1711 1157 898 781 510 961 775 206 291 127 104 44
2870 950 1132 652 1080 454 399 79 312 183 153 184 39
PBS
SVCV
vaccinated +SVCV
Neutrophils 1
Macrophage/myeloid
Neutrophils 2
B cells
HSPCs 1
T/NK cells
HSPCs 2
Kidney multiciliated cells
HSPCs 3
Neutrophils 3
Kidney distal tubule
Kidney mucin cells
Kidney proximal tubule